

INFORMATION TO USERS

This manuscript has been reproduced from the microfilm master. UMI films the text directly from the original or copy submitted. Thus, some thesis and dissertation copies are in typewriter face, while others may be from any type of computer printer.

The quality of this reproduction is dependent upon the quality of the copy submitted. Broken or indistinct print, colored or poor quality illustrations and photographs, print bleedthrough, substandard margins, and improper alignment can adversely affect reproduction.

In the unlikely event that the author did not send UMI a complete manuscript and there are missing pages, these will be noted. Also, if unauthorized copyright material had to be removed, a note will indicate the deletion.

Oversize materials (e.g., maps, drawings, charts) are reproduced by sectioning the original, beginning at the upper left-hand corner and continuing from left to right in equal sections with small overlaps. Each original is also photographed in one exposure and is included in reduced form at the back of the book.

Photographs included in the original manuscript have been reproduced xerographically in this copy. Higher quality 6" x 9" black and white photographic prints are available for any photographs or illustrations appearing in this copy for an additional charge. Contact UMI directly to order.

UMI

**A Bell & Howell Information Company
300 North Zeeb Road, Ann Arbor MI 48106-1346 USA
313/761-4700 800/521-0600**

**ON-LINE TOOL MISALIGNMENT DETECTION USING
AN IMAGING METHOD**

by

Tong Xie

**A Dissertation Submitted to the Faculty of the
COMMITTEE ON OPTICAL SCIENCES (GRADUATE)**

In Partial Fulfillment of the Requirements

For the Degree of

DOCTOR OF PHILOSOPHY

In the Graduate College

THE UNIVERSITY OF ARIZONA

1997

UMI Number: 9806848

UMI Microform 9806848
Copyright 1997, by UMI Company. All rights reserved.

**This microform edition is protected against unauthorized
copying under Title 17, United States Code.**

UMI
300 North Zeeb Road
Ann Arbor, MI 48103

THE UNIVERSITY OF ARIZONA ©
GRADUATE COLLEGE

As members of the Final Examination Committee, we certify that we have read the dissertation prepared by Tong Xie

entitled On-line Tool Misalignment Detection Using an Imaging Method

and recommend that it be accepted as fulfilling the dissertation requirement for the Degree of Doctor of Philosophy

[Signature]
(John E. Greivenkamp) Date 8-6-97

[Signature]
(Jose Sasian) Date 8-6-97

[Signature]
(Michael Descour) Date 8-6-97

Date _____

Date _____

Final approval and acceptance of this dissertation is contingent upon the candidate's submission of the final copy of the dissertation to the Graduate College.

I hereby certify that I have read this dissertation prepared under my direction and recommend that it be accepted as fulfilling the dissertation requirement.

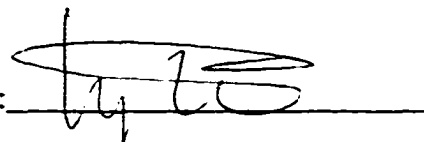
John E. Greivenkamp [Signature] Date 8-11-97
Dissertation Director

STATEMENT BY THE AUTHOR

This dissertation has been submitted in partial fulfillment of requirements for an advanced degree at The University of Arizona and is deposited in the University Library to be made available to borrowers under rules of the Library.

Brief quotations from this dissertation are allowable without special permission provided that accurate acknowledgment of source is made. Requests for permission for extended quotation from or reproduction of this manuscript in whole or in part may be granted by the head of the major department or the Dean of the Graduate College when in his or her judgment the proposed use of the material is in the interests of scholarship. In all other instances, however, permission must be obtained from the author.

SIGNED: _____

A handwritten signature in black ink, appearing to be 'J. L. ...', written over a horizontal line.

ACKNOWLEDGEMENT

This work was made possible through funding support provided by the U.S. Army Material Command, under contract #DAAA21-94-C-0003 and sponsorship by the Center for Optics Manufacturing (COM) at the University of Rochester. I would like to thank the staff of COM for their support, especially Harvey Pollicove, Steve Jacobs, Don Golini and Jeff Ruckman. I thank Mark Atwood and Ed Sess for their helps during my on-site studies at COM.

I would like to express my gratitude to my adviser, Professor John E. Greivenkamp, for his patience and guidance throughout the duration of this project. I also want to extend my appreciation to the committee members, Profs. Michael R. Descour and Jose M. Sasian for taking the time to read and comment on my work.

I would like to thank my colleagues in the Optical Testing and Ophthalmic Research lab, Matthew Chang, Heidi Hall, Jim Schwiegerling, Andrew Lowman and many others, for their support and friendship. I thank Heidi Hall, Yuchun Chang and Matthew Chang for reviewing this manuscript in its various stages and providing valuable suggestions.

I want to thank Prof. Jack Gaskill for his vision, which led to the establishment of the undergraduate program at the Optical Sciences Center. Thanks also go to Mike Nofziger for his effort in this program. I feel proud and fortunate to be the first graduate from the program. I also thank Jack for giving me the opportunity to be the first person who received a complete optical education, both undergraduate and graduate, from the center.

Finally, I want to express my deepest appreciation to my parents, Ying and Wenhua Xie, to my sister and brother-in-law, Hong and Hua Chen, who always encouraged me and supported me. I thank my grandparents for their trust in me. I would also like to contribute my special thanks to Mabel and Bill Sears for their friendship and helps.

To My Mother and Father

TABLE OF CONTENTS

LIST OF FIGURES.....	10
ABSTRACT	14
INTRODUCTION	16
1. OPTICAM OPTICAL SURFACE GENERATOR.....	23
1.1 Opticam Generator	23
1.2 Ring Grinding Geometry	28
2. SURFACE FIGURE ERRORS	
PRODUCED BY MACHINE SETUP ERRORS.....	33
2.1 Static Tool Alignment Errors	34
2.1.1 X-direction tool misalignment.....	35
2.1.2 Y-direction tool misalignment.....	39
2.2 Other Sources of Errors	51
2.2.1 Errors in the tool radius and the tilt angle	51
2.2.2 Machine dwell error.....	53
2.3 Tool Misalignment Detection System	54
3. CONVENTIONAL SURFACE METROLOGY SYSTEMS.....	57
3.1 Optical Interferometric Systems	57
3.2 Fringe and Moiré Projection.....	61
3.3 Mechanical Stylus Profiler	64

TABLE OF CONTENTS - *Continued*

3.4 Moiré Deflectometry	67
3.5 New Metrology Method	71
4. INTERFERENCE FRINGE ANALYSIS METHODS	73
4.1 Spatial Synchronous Method.....	74
4.2 Fourier Transform Method	76
4.3 Phase Unwrapping.....	84
4.4 Fringe Analysis Method Used in the On-line Tool Misalignment Detection System.....	85
5. DESCRIPTION OF THE NEW METROLOGY SYSTEM	87
5.1 Theoretical Background	87
5.1.1 Image distortions	88
5.1.2 Reflected images produced by Opticam generated surfaces with y-errors	91
5.2 Tool Misalignment Detection using an Imaging Method.....	93
5.3 Image Processing Algorithm	96
5.4 Computer Simulations	99
6. PROTOTYPE SYSTEM DESIGN	106
6.1 New Off-axis Geometry	107
6.2 Hardware Design	109

TABLE OF CONTENTS - *Continued*

6.2.1 Imaging system.....	111
6.2.2 Illumination system	113
6.2.3 Bar target and target holder	116
6.2.4 Electronic controls and frame grabber.....	117
6.3 Software Design	118
6.4 Surface Wetting Technique	122
7. EXPERIMENTAL RESULTS	126
7.1 Detection Setup.....	127
7.2 Surface Figure Errors from Cutter Misalignments and Machine Dwell	129
7.3 Detection Sensitivity.....	134
7.4 Cutter Mark Orientation Identification.....	139
7.5 Machine Spark Out Time and Surface Dwell Error	140
7.6 Study of Surface Wetting Agent.....	141
8. DISSCUSSION AND CONCLUSION.....	143
8.1 X-Error Detection	145
8.2 Surface Height Map.....	146
8.3 Radius of Curvature Measurement.....	148
8.4 Other Applications.....	154

TABLE OF CONTENTS - *Continued*

APPENDIX: PROGRAM LISTING	155
REFERENCES	169

LIST OF FIGURES

Figure 1.1: Opticam SX machine	26
Figure 1.2: Schematic drawing of the Opticam ring grinding geometry	27
Figure 1.3: Mathematical model of the ring grinding geometry	29
Figure 2.1: Perspective views of the grinding setup with x-direction tool misalignments.....	36
Figure 2.2: Top views of the grinding setup with x-errors	37
Figure 2.3: Mathematical model of the ring grinding geometry with +x-error	39
Figure 2.4: Perspective views of the grinding setup with y-direction tool misalignments.....	40
Figure 2.5: Top views of the grinding setup with y-errors	41
Figure 2.6: Mathematical model of the ring grinding geometry with -y-error.....	42
Figure 2.7: Surface error map of a part generated with 100 μm y-direction.....	47
Figure 2.8: Surface error produced by y-direction tool misalignment	48
Figure 2.9: Cutter marks on Opticam generated surfaces.....	49
Figure 2.10: Surface PV error vs. y-error for R/2 surfaces	50
Figure 2.11: Surface error map of a part with machine dwell error	54
Figure 3.1: Simple Fizeau interferometer testing a concave mirror	59
Figure 3.2: Fringe projection	62

LIST OF FIGURES - *Continued*

Figure 3.3: System setups for shadow and projection moiré.....	63
Figure 3.4: Stylus profiler.....	65
Figure 3.5: Moiré deflectometry system.....	68
Figure 3.6: Moiré deflectometric setup for testing a concave mirror	70
Figure 4.1: Distorted bar image.....	80
Figure 4.2: Spatial frequency spectrum of the distorted image along a horizontal line ...	80
Figure 4.3: Filtered and shifted spectrum.....	81
Figure 4.4: Calculated raw phase function	82
Figure 4.5: Unwrapped phase function.....	83
Figure 5.1: Law of reflection.....	88
Figure 5.2: A flat surface produces reflected images with no distortion.....	89
Figure 5.3: Distorted image produced by a curved surface	90
Figure 5.4: Reflected image formed by a cone-shaped surface.....	92
Figure 5.5: Tool misalignment detection system layout.....	94
Figure 5.6: Surface slope averaging due to finite aperture size.....	96
Figure 5.7: System setup used in the ray trace analysis	100
Figure 5.8: Computer generated image of a bar target reflected off a surface with 100 μm y-error	102

LIST OF FIGURES - *Continued*

Figure 5.9: Calculated phase function of the image in Figure 5.8.....	102
Figure 5.10: Captured reflected image of a bar target off a surface with 100 μm y-error	103
Figure 5.11: Calculated phase profile of the image in Figure 5.10	103
Figure 5.12: Phase discontinuity vs. y-error	104
Figure 6.1: Off-axis layout of the detection system	107
Figure 6.2: Hardware unit of the prototype tool misalignment detection system	110
Figure 6.3: The imaging lens and the CCD camera on the tilt stage	111
Figure 6.4: Image location shift as a function of the surface base radius.....	112
Figure 6.5: Picture of the illumination unit	115
Figure 6.6: Schematic drawing of the illumination unit.....	115
Figure 6.7: Screen capture of the image analysis program.....	120
Figure 6.8: Flow chart of the image analysis program	121
Figure 6.9: Schematic drawing of the surface wetting process	123
Figure 6.10: Comparison of image contrast for dry and wet surfaces.....	124
Figure 6.11: Calculate phase discontinuities of the reflected images off a test surface before and after surface wetting	125
Figure 7.1: Tool misalignment detection system in the Opticam SX generator.....	128

LIST OF FIGURES - *Continued*

Figure 7.2: Surface error map of a part with machine dwell error	130
Figure 7.3: Surface error map of a part generated with y-error.....	130
Figure 7.4: Surface PV error vs. y-error for surfaces with different radius of curvature.....	131
Figure 7.5: Opticam generated part with machine dwell error.....	133
Figure 7.6: Surface PV error vs. $\pm y$ -error.....	135
Figure 7.7: Measured y-error vs. nominal misalignment	137
Figure 7.8: Residual surface PV error vs. y-error.....	138
Figure 7.9: Surface PV error vs. machine dwell time	141
Figure 8.1: Comparison of non-telecentric and telecentric imaging systems.....	147
Figure 8.2: Depth of field vs. image position tolerance for $ \Delta R/R =0.01$	153
Figure 8.3: Depth of focus vs. image position tolerance for $ \Delta R/R =0.1$	153

ABSTRACT

The Opticam spherical surface generator is developed at the Center for Optics Manufacturing (COM). It combines computer-numerical-control (CNC) technology with bound abrasive ring grinding geometry to create advantages over the conventional loose abrasive grinding systems in flexibility, productivity and accuracy. The Opticam SX utilizes a ring grinding geometry to generate spherical surfaces. By adjusting the tilt angle and the diameter of the ring cutter, the Opticam is capable of generating spherical surfaces with an essentially unlimited range of radius of curvature. This ring grinding geometry, however, requires a precise alignment between the cutter and the generated part. Residual cutter misalignments in the machine setup cause the finished surface to deviate from the design shape.

Current tool misalignment detection techniques seriously limit the productivity of the Opticam system, and a new metrology system is introduced in this dissertation. The new system is geometrical ray trace based, and has some similarities to the moiré deflectometry techniques. It uses a non-contact method to measure surface slope errors from images reflected off Opticam generated surfaces. The detected slope errors are used to determine the corresponding tool misalignments in the Opticam generator. The system setup is simple and not sensitive to vibrations. This system is compatible with the wet

grinding environment. Furthermore, this new metrology system is capable of measuring surfaces with a wide range of radius of curvature from convex to concave.

A prototype system was built based on this technique. It has been evaluated on-line in the Opticam SX. A surface wetting technique is used to allow detection on Opticam generated surfaces independent of the actual surface finish. The experimental results suggested that the on-line detection system is capable of detecting tool misalignment corresponding to a peak-to-valley surface figure error that is 1 μm or greater on ground surfaces. Better than 0.5 μm peak-to-valley surface error detection was achieved on specular surfaces. It was also found that machine dwell produces surface figure errors that are opposite to the errors produced by y-direction tool misalignment. Best surface figures are achieved when machine dwell errors are balance by residual tool misalignments in the Opticam machine.

INTRODUCTION

Traditional optical fabrication techniques based on open-loop processes, loose abrasive grinding, hand lapping and polishing severely limit the flexibility, and productivity of optical elements. The introduction of the computer-numeric-control (CNC) technology in the optical fabrication industry helps to take optical manufacturing into a new era [Pollicove et. al. 1992]. The new CNC-based optical surface generating and polishing systems significantly reduce the manufacture cycle time and improve the production throughput. One of the most successful CNC based optical surface generator systems is the Opticam spherical surface generator [Golini and Czajkowski 1992]. The Opticam system was developed by the Center for Optics Manufacturing (COM) centered at the University of Rochester located in Rochester, NY [Pollicove and Moore 1992].

The Opticam spherical surface generator incorporates CNC technology with the deterministic ring tool micro-grinding geometry to generate spherical optical surfaces with superior figure accuracy. The surface generation process in the Opticam generator is executed by a diamond-impregnated ring shaped cutting tool. During the grinding process, the part and the ring cutter are spun at approximately 200 rpm and 10,000 rpm respectively [Golini 1996]. Spherical surfaces are produced by tilting the ring cutter spindle from the spindle axis of the generated part by a calculated angle. The cutter tilt angle and its diameter determine the radius of curvature of the finished surface.

The advantages of the ring grinding geometry versus the traditional loose abrasive grinding system reside at its superior flexibility in controlling the shape of the finished parts and its high production throughput [Lindquist 1996]. The ring grinding geometry allows the Opticam generator to produce spherical surfaces with an essentially unlimited range of radius of curvature, without special radiused cutting tools. However, this geometry also requires a precise alignment between the cutter and the part. Uncertainties in the machine grinding setup produce errors on the finished parts [Rich and Lindquist 1993]. The sources of error include cutting tool misalignments, errors in the diameter and the tilt angle of the ring cutter, tool wear and machine dwelling.

During the surface generation process, the ring cutter edge must coincide with the vertex of the generated surface. Cutting tool misalignments in the Opticam system result in surface figure errors on the final parts. Two types of tool alignment errors may exist in the Opticam machine setup [Rich and Lindquist 1993]. X-direction misalignment, position error of the cutter in the plane of the tilt, produces radius of curvature errors on the finished surface. Cutter misalignment perpendicular to the x-direction, defined as y-error, causes the final surface shape to deviate from a sphere.

In order for the Opticam machine to generate pre-polished parts with the highest accuracy in surface figure, it is necessary to correct these machine tool misalignments in the Opticam system. Conventional metrology systems, such as interferometric systems,

mechanical stylus profilers, fringe and moiré projection systems and moiré deflectometers are not suitable for this application due to their limitations and special setup requirements. Most of these techniques require an off-line detection procedure, requiring the test part to be removed from the machine, limiting the productivity of the Opticam generator.

Spherometers are often used in practice to determine the tool alignment errors from the measured surface radius error. The measurements may be conducted on-line without removing the generated parts. Nevertheless, because of the lack of simple conversion between the surface radius errors and the tool misalignments, the Opticam operators' experience becomes important in the correct identification of the tool misalignment using this technique. Several iterations may be taken before tool alignment errors can be eliminated, and the productivity of the Opticam system is compromised. A new on-line metrology system for tool misalignment detection must be developed.

The on-line detection system described in this dissertation detects the y-direction tool alignment errors in the Opticam spherical surface generator in real-time without the need for removing the part from the spindle. The detection technique was developed based on optical image formation concepts. It is geometrical ray trace based technique with strong similarities to moiré deflectometry techniques. It uses a non-contact method to measure surface slope errors from the distortion information in the reflected image off the test

surface. Different from moiré deflectometry, this technique does not require a spatially coherent light source, which further simplified the system setup.

Image analysis in the detection system is completed using a Fourier transform method. This method does not require multiple phase-shifted images and phase shifting hardware. Only a single frame is necessary to retrieve a 2D phase map of the test surface in the direction that is perpendicular to the fringe orientation. Images with different carrier frequencies may be analyzed without prior knowledge about the fringe period, which is required for spatial synchronous detection technique.

It will be shown that a y-direction tool misalignment primarily results in a slope discontinuity at the vertex of the generated surface. Slope discontinuities on the test surface are determined from the phase discontinuities in the reflected image of a grating pattern. The calculated phase function of the reflected image is related to the slope function of the test surface. Finally, tool misalignment errors are calculated from the measured surface slope discontinuities using the linear relationship between these two quantities. Knowledge of about the detection setup geometry, i.e., the target frequency, the target to surface distance and base radius of the test surface, are required for this calculation.

The new on-line metrology system allows a real-time feedback to the Opticam machine operator to correct errors in the machine geometry. It has the potential to be set

up in a closed loop operation environment in the Opticam system. It may be used to measure concave and convex surfaces without adjustment. The system setup has a considerably low requirement on the mechanical stability. It also takes advantage of the wet grinding environment to accommodate variations in specularities of the test surfaces. Ground surfaces can be measured as well as specular surfaces.

The dissertation begins by providing a brief review of the existing optical fabrication techniques in Chapter 1. A new generation optical fabrication system based on CNC technology is then introduced. The Opticam system and the ring tool micro-grinding geometry are described. The advantages of the ring grinding setup versus the conventional optical fabrication processes are also discussed. A mathematical model of the ring grinding geometry is given in this chapter. It is used to derive the simple relationship between the Opticam generated surface figure and the machine grinding setup geometry.

Possible sources of error in the Opticam machine are analyzed in Chapter 2. Surface errors result from these machine setup errors are studied. Static tool misalignments and their effects on surface figure errors are specially addressed. X-errors and y-errors are studied independently. Mathematical descriptions of surfaces generated with static tool misalignments are presented. The needs of an on-line tool misalignment detection system for the Opticam machine are discussed.

In Chapter 3, we will review several commonly used metrology techniques. Their principles and typical applications are provided. The advantages and disadvantages of these systems are presented. We will show that limitations in these systems prevent them from being used for the on-line tool misalignment detection. A new metrology technique using an imaging method is introduced.

Different methods used for interferogram analysis are examined in Chapter 4. Spatial analysis methods are discussed in detail, because of their advantages over the temporal techniques for this application. Basic theories behind both the spatial synchronous detection and the Fourier transform technique are provided. Their advantages and disadvantages are studied. An example demonstrating the process of the Fourier transfer method is given. Techniques for correction of phase wrapping errors are also discussed. Both the Fourier transform technique and the linear scanning phase unwrapping method are adopted in the on-line tool misalignment detection system.

A theoretical study of the new metrology technique is described in Chapter 5. The conceptual layout of the detection system is given. A detailed description on the selection of the shape and the bandwidth of the spatial filter used in the Fourier image process is given. Computer simulations and ray trace analysis of the detection setup are completed. For comparison with the simulation results, a real detection image and the analysis result are shown.

Chapter 6 describes the design of the prototype detection system. A new off-axis layout is introduced. Its advantages over the original co-axial setup are discussed. Individual modules in the prototype system are described in detail. An integrated software package designed for hardware control and image analysis is introduced. A surface wetting technique is proposed in this chapter to take advantage of the wet grinding environment in the Opticam machine. This technique allows the detection system to measure surfaces independent of their actual surface finish, from ground to polished.

Experimental implementation of the on-line detection system is presented in Chapter 7. Final on-line tests of the prototype system with an Opticam SX generator are described. The detection sensitivity of the prototype system is examined. A detailed discussion of machine dwell error effects on the overall surface figures for Opticam generated surfaces is given. A study on Opticam coolant used for surface wetting is completed.

At the end, we will discuss the limitations of this on-line metrology system. We will address the possibilities of 2D surface slope metrology, x-error detection and full integration of the system into the Opticam machine. Possible modifications of the existing system for surface height map measurement and radius of curvature measurement are suggested. Extensions for the application of the new detection technique are also discussed.

CHAPTER 1

OPTICAM OPTICAL SURFACE GENERATOR

In this chapter, conventional optical manufacturing techniques are briefly reviewed. A new generation of optical fabrication systems based on computer-numerical-control and the bound abrasive ring tool grinding geometry is introduced. The advantages of the CNC-based ring grinding technique over conventional loose abrasive processes are discussed. One of the most successful CNC-based systems, the Opticam spherical surface generator, is described in detail. The deterministic ring grinding geometry used in the Opticam is studied. A mathematical modeling of the ring grinding setup will show that parts generated by the Opticam have shapes that are precisely determined by the grinding geometry. It will also show that the ring geometry provides the Opticam system the flexibility in generating spherical surface with virtually unlimited radius of curvature.

1.1 OPTICAM GENERATOR

Conventional optical manufacturing technique relies on labor intensive, multi-machine processes. Low material removal rate in the loose abrasive based grinding systems severely limits the productivity of optical instruments. Control of the generated

surface shape is also different in these systems. Modern precision machine based optical manufacturing systems use bound abrasive ring cutting tool, which allows a much higher production throughput compared to the loose abrasive grinding process [Lindquist 1996]. The ring grinding geometry also gives these systems flexibility in controlling the shape of the finished surface. Recent development of the new generation CNC based grinding systems further advanced the optical fabrication technology. The new systems combine the computer numerical control with the bound abrasive ring grinding geometry. The CNC technology provides these systems even higher flexibility in controlling the grinding process and further improves the quality and the productivity of the optical fabrication process [Lindquist 1996].

The Opticam spherical surface generator is one of the new generation CNC-based optical surface generators. It was developed by the Center for Optics Manufacturing (COM) located at the University of Rochester. It is designed to revolutionize the optical fabrication industry, and replace the traditional labor intensive and multi-machine processes. With the helps from the modern CNC technology, the Opticam system is capable of generating spherical surfaces with extraordinarily accurate surface figure with superior surface finish. The Opticam system can generate odd shaped surfaces and mount interface geometry, which is not possible with conventional systems [Pollicove and Moore 1990].

The Opticam systems eliminate the need for multi-machine process. Generation, fine grinding, lens centering can be accomplished in one setup. The machine axis in the Opticam system coincides with both the mechanical and the optical axis, which improves the accuracy of the generated part. The Opticam machine eliminates non-symmetrical figure errors resulting from the misalignment between axes of the conventional multiple-machine process and numerous part-handling operations between machines [Pollicove and Moore 1990].

Programming capability in the Opticam generator enables a fully automatic fabrication procedure. Generated parts can also be edged directly to achieve automatic centration. Computerized routines for process controls in the Opticam generator also enable the potential for computer integrated manufacturing (CIM) linkages to computer aided design (CAD) stations [Taylor et. al. 1996]. Compared to the conventional loose abrasive grinding process, the Opticam system provides a much higher throughput at high precision.

The Opticam SX is a commercial implementation of the optical spherical generator produced by CNC system, Inc. (Ontario, NY) (Figure 1.1). Ring shape metal bond diamond cutting tools are used to generate spherical optical surfaces. Figure 1.2 shows a schematic drawing of the ring tool grinding geometry used in the Opticam SX. Accurate and flexible motions of the ring cutter tilt angles, pivot center and linear motions in the Opticam SX give the machine superior control over the generated surface figures

[Lindquist 1996]. In the Opticam SX, the ring tool spindle has a dynamic range from 6000 to 30,000 rpm, while the maximum part spindle speed is 250 rpm. Linear resolution on both the x and the z axes is $0.1 \mu\text{m}$, and the slowest allowable infeed rate on the z-axis is $0.1 \mu\text{m}/\text{sec}$. Angular accuracy of the cutter spindle axis is $\pm 3.5 \text{ arcsec}$ [Golini 1993].

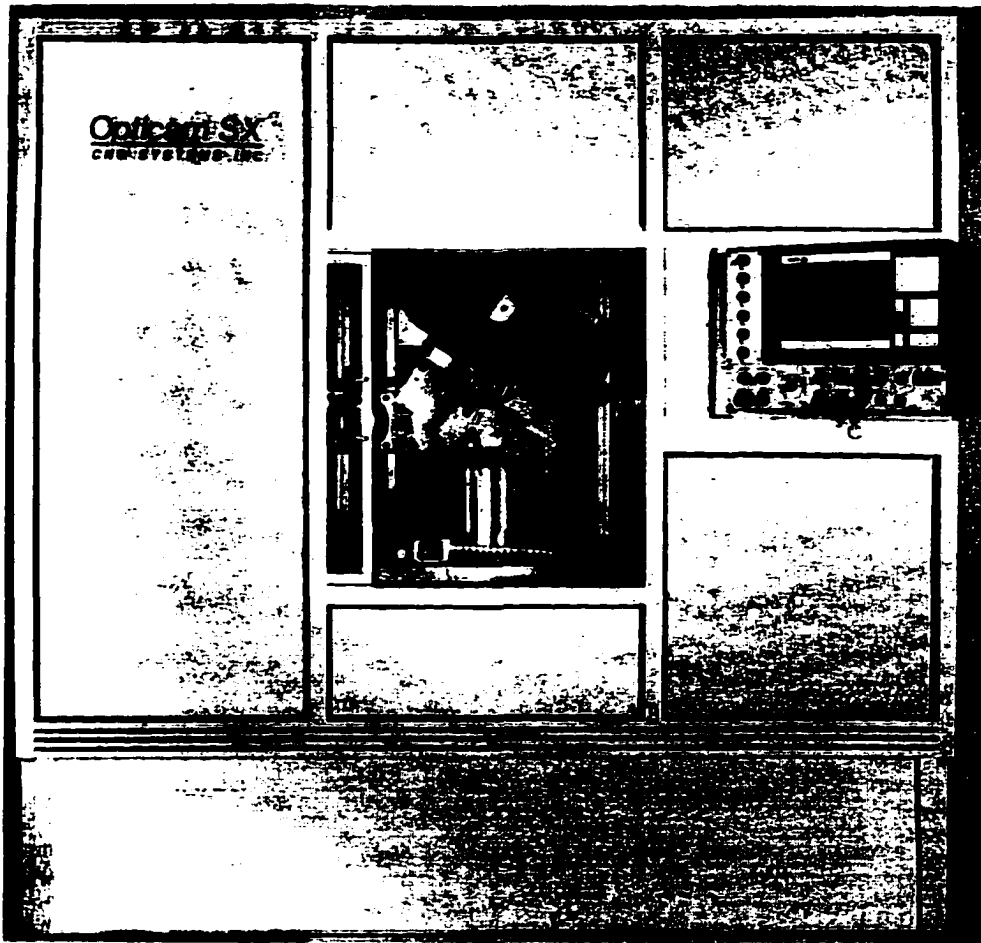


Figure 1.1. Opticam SX machine.

The metal bonded diamond tool used in the Opticam system along with the high spindle speed allows a fast material removal rate, which greatly improves the

productivity of the surface generation process. High rigidity and stiffness of the part and cutter spindles along with the computer controlled infeed rates allow the Opticam system to generate optical surfaces with superior surface finish and figure accuracy. The Opticam SX system is capable of producing near specular microground surfaces with 1 to 2 μm subsurface damage and less than 1λ of peak-to-valley figure error [Golini 1996]. This combination of features allows for a well characterized, repeatable and predictable process that has been termed deterministic micro-grinding.

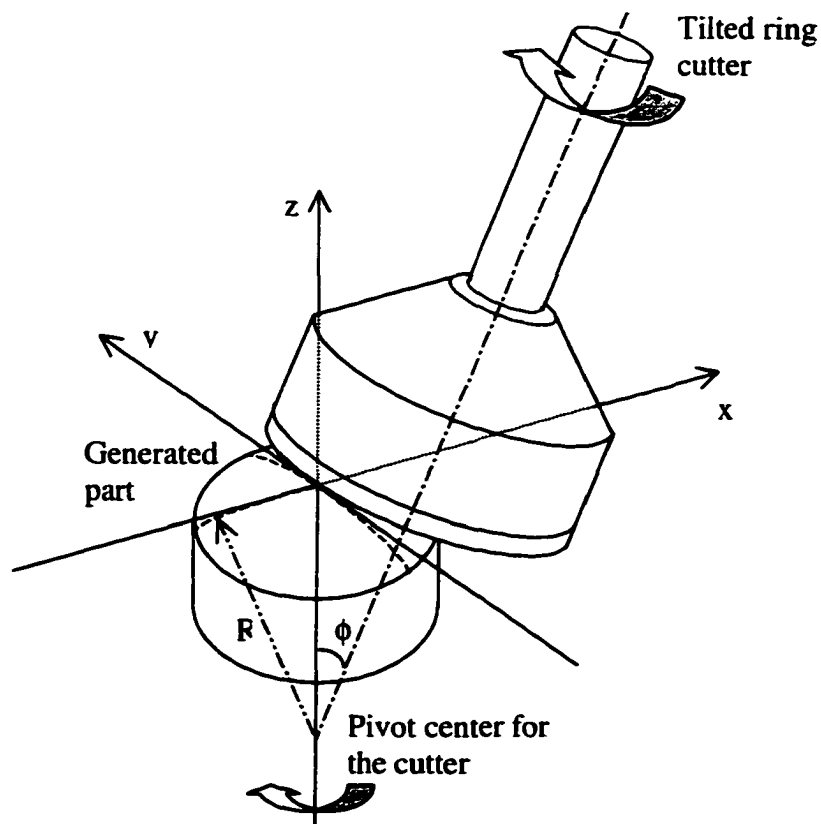


Figure 1.2. Schematic drawing of the Opticam ring grinding geometry.

During the grinding process, the part spindle is spun at approximately 200 rpm, while the tool spindle is spun at a much higher speed, about 10,000 rpm typically. The generation process is executed by the ring shape cutter mounted on the tool head. Spherical surfaces are produced by tilting the cutter head with respect to the part spindle axis during surface generation process.

1.2 RING GRINDING GEOMETRY

A mathematical model describing the ring grinding geometry is developed. Using this model, we will show that the ring grinding geometry is a deterministic process for producing spherical surfaces with defined radii of curvature. Radii of curvature of the Opticam generated surfaces are determined by the ring cutter radius (T) and the tilt angle (ϕ) of the cutter spindle axis with respect to the part spindle. Furthermore, the Opticam generator is capable of generating spherical surfaces with a wide range of radius of curvature without special radiused cutting tools. In this model, grinding dynamics, chemical reaction, area contacts, etc., are not included. The model also assumes that both tool and part are rigid and the shape of the finished surface depends only on the geometry of the cutting tool relative to the generated part.

The modeling process starts by characterizing the ring cutter and the generated part in two separated right-handed Cartesian coordinate systems (see Figure 1.3). The cutter

coordinate system ($x'-y'-z'$) is tilted with respect to the part coordinate system ($x-y-z$) by an angle (ϕ) in the $x-z$ plane from the optical axis defined by the generated part (z -axis). The edge of the ring cutter in this initial model is aligned with the vertex of the part.

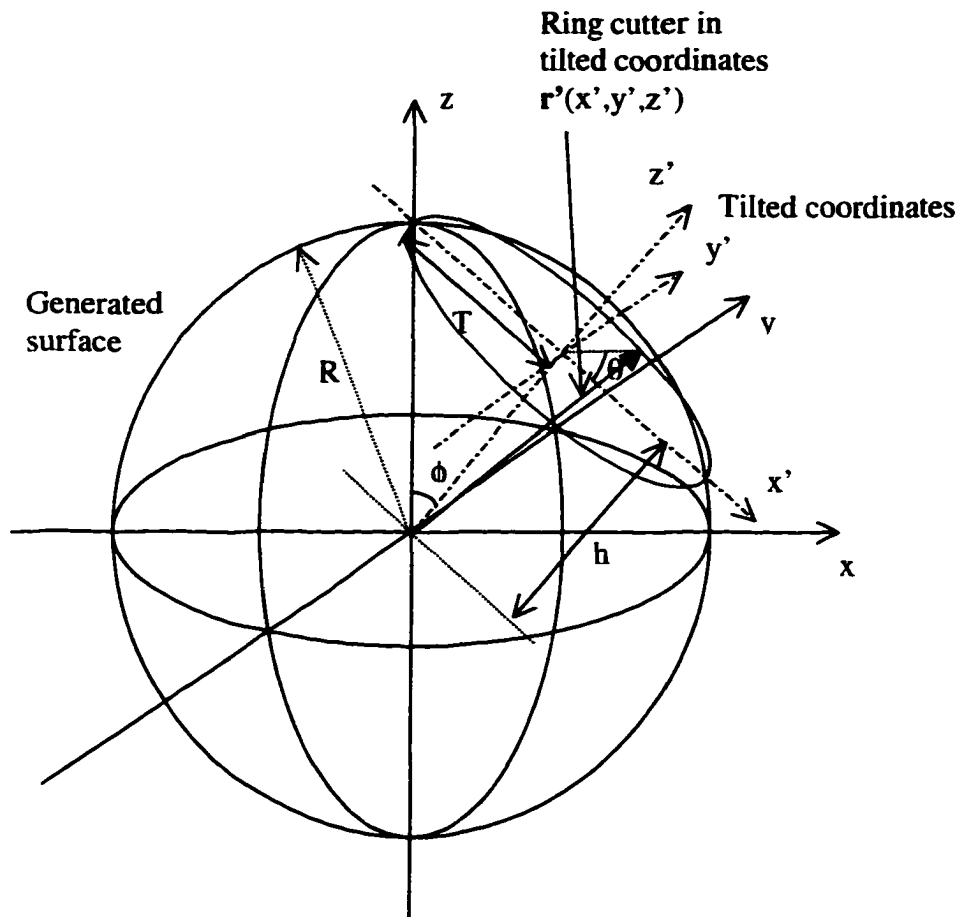


Figure 1.3. Mathematical model of the ring grinding geometry.

A vector $\mathbf{r}'(x', y', z')$ can be used to describe the ring shape cutter in the tilted coordinate system:

$$\begin{aligned}
 x' &= T \cos \theta \\
 y' &= T \sin \theta \\
 z' &= h
 \end{aligned}
 \tag{1.1}$$

where:

T = radius of the ring cutter;

θ = angle in the x' - y' plane from the x' -axis;

h = displacement of the ring cutter from its pivot center along the z -axis.

During the grinding process, the ring cutter edge conforms to the generated surface shape, and the finish surface figure is confined by the ring cutter edge. Hence, a description of the final surface figure may be obtained from the geometrical path of the ring cutter edge in the un-tilted part coordinate system. To do this, a rotation matrix M_{rot} may be applied to the vector $\mathbf{r}'(x', y', z')$, and $\mathbf{r}(x, y, z) = M_{rot} \mathbf{r}'(x', y', z')$.

$$M_{rot} = \begin{bmatrix} \cos \phi & 0 & \sin \phi \\ 0 & 1 & 0 \\ -\sin \phi & 0 & \cos \phi \end{bmatrix}
 \tag{1.2}$$

$$\begin{bmatrix} x \\ y \\ z \end{bmatrix} = M_{rot} \cdot \begin{bmatrix} x' \\ y' \\ z' \end{bmatrix}
 \tag{1.3}$$

A new vector $\mathbf{r}(x, y, z)$ is obtained to represent the generated surface:

$$\mathbf{r}(x, y, z) = \begin{bmatrix} x \\ y \\ z \end{bmatrix} = \begin{bmatrix} \cos \phi & 0 & \sin \phi \\ 0 & 1 & 0 \\ -\sin \phi & 0 & \cos \phi \end{bmatrix} \cdot \begin{bmatrix} x' \\ y' \\ z' \end{bmatrix}
 \tag{1.4}$$

$$= \begin{bmatrix} \cos\phi & 0 & \sin\phi \\ 0 & 1 & 0 \\ -\sin\phi & 0 & \cos\phi \end{bmatrix} \cdot \begin{bmatrix} T \cos\theta \\ T \sin\theta \\ h \end{bmatrix} \quad (1.5)$$

$$= \begin{bmatrix} T \cos\theta \cos\phi + h \sin\phi \\ T \sin\theta \\ -T \cos\theta \sin\phi + h \cos\phi \end{bmatrix} \quad (1.6)$$

An alternative expression for this surface may be written in terms of x^2 , y^2 , z^2 as:

$$\begin{aligned} x^2 + y^2 &= (T \cos\theta \cos\phi + h \sin\phi)^2 + (T \sin\theta)^2 \\ &= T^2 \cos^2\theta \cos^2\phi + h^2 \sin^2\phi + 2Th \cos\theta \cos\phi \sin\phi + T^2 \sin^2\theta, \end{aligned} \quad (1.7)$$

$$\begin{aligned} z^2 &= (-T \cos\theta \sin\phi + h \cos\phi)^2 \\ &= T^2 \cos^2\theta \sin^2\phi + h^2 \cos^2\phi - 2Th \cos\theta \cos\phi \sin\phi, \end{aligned} \quad (1.8)$$

$$\begin{aligned} x^2 + y^2 + z^2 &= T^2 \cos^2\theta \cos^2\phi + T^2 \cos^2\theta \sin^2\phi + T^2 \sin^2\theta \\ &\quad + 2Th \cos\theta \cos\phi \sin\phi - 2Th \cos\theta \cos\phi \sin\phi, \\ &\quad + h^2 \sin^2\phi + h^2 \cos^2\phi \end{aligned} \quad (1.9)$$

Therefore,
$$x^2 + y^2 + z^2 = h^2 + T^2. \quad (1.10)$$

Equation (1.10) shows that an Opticam generated surface have a spherical shape. And, the radius of curvature of the surface is defined by the displacement of the ring cutter (h) and the cutter radius (T). In the x - z plane ($y=0$), a radial cross section of the finished part is a circle (Equation 1.11).

$$x^2 + z^2 = h^2 + T^2 = R^2. \quad (1.11)$$

Both h and T can also be related to the tilt angle (ϕ) of the cutter spindle. Simple relationships among the radius of curvature of the finished surface, the ring cutter radius and the tilt angle of the cutter can be written as:

$$\begin{aligned} h &= R \cos \phi \\ T &= R \sin \phi \end{aligned} \quad (1.12)$$

therefore,
$$R = \frac{T}{\sin \phi}. \quad (1.13)$$

The above mathematical modeling of the ring tool grinding geometry shows that the radius of curvature of Opticam generated surfaces is precisely determined by the grinding geometry, i.e., the ring cutter radius and the cutter tilt angle. Freedom in controlling the grinding geometry in the Opticam spherical surface generator provides the machine an essentially unlimited flexibility in generating spherical optical surfaces with a large range of radius of curvature. Since the maximum value of $\sin \phi$ is limited to unity, the minimum radius that can be theoretically generated is equal to the tool radius. Practical limitations will allow ϕ to vary to about 60 deg., so that radius of approximately 1.15T to a flat can be generated for a single ring tool. Using a single cutting tool, the Opticam machine can generate spherical surfaces with virtually any radius of curvature by adjusting the tilt angle of the cutter spindle.

CHAPTER 2

SURFACE FIGURE ERRORS PRODUCED BY MACHINE SETUP ERRORS

Surfaces generated using deterministic ring tool grinding process have shapes that are precisely determined by the grinding geometry. Consequentially, uncertainties in the grinding setup result in finished parts with undesired shapes. Possible sources of error exist in the Opticam system are discussed in this chapter. Surface figure errors resulting from static tool misalignments are studied in detail. A mathematical model for the ring geometry, similar to the one developed in Section 1.2, is used to obtain mathematical descriptions on the Opticam generated surfaces with grinding geometry errors.

We again assume that both the ring shape grinding tool and part have rigid structures in the model. Furthermore, the shape of the generated surface is assumed to be determined only by the geometrical relationship between the ring cutter and the part during grinding process. Chemical interaction, grinding dynamics, area contact and infeed rate, etc. are not included in this study.

In order for the Opticam system to produce high precision optical surfaces, tool misalignments in the grinding setup must be corrected. To maintain high productivity for the Opticam machine at the same time, an on-line tool misalignment detection system is necessary. At the end of this chapter, we will discuss the needs for this real time tool misalignment detection system.

2.1 STATIC TOOL ALIGNMENT ERRORS

The deterministic ring grinding geometry used in the Opticam SX machine requires a precise alignment between the ring cutter and the generated surface. Under the ideal grinding condition, the ring cutter edge is coincident with the vertex of the generated surface throughout the generation process. Geometrical errors in the grinding setup result in figure errors on the finished parts. Displacements of the ring cutter edge from its ideal position in the Opticam system are defined as static alignment errors.

Static tool alignment errors in the Opticam system can be classified into two basic types based on the direction of the error [Quesnel et. al. 1994]. X-direction tool misalignment is defined as the displacement of the cutter in the plane of the tilt of the cutter spindle. Perpendicular to the tilt (x-z) plane, displacement of the cutter along the y-axis is called y-error. Surface figure errors produced by these two types of tool misalignments are different and independent of each other.

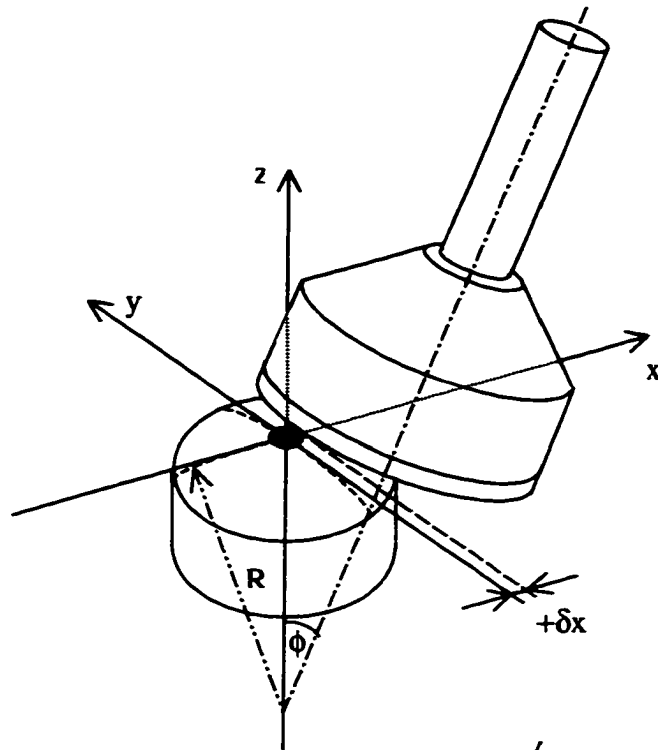
For the static tool error studies, tool wear, errors in both the diameter and the tilt angle of the ring cutter are not included for simplicity. Machine dwell effects (see Section 2.2.2) are also ignored in the analysis.

2.1.1 X-direction tool misalignment

X-direction tool misalignment is the displacement of the ring cutter edge with respect to the vertex of the generated surface in the tilt plane of the cutter spindle (x - z plane). Figure 2.1 illustrates the tool alignment errors in both positive and negative x -directions.

In Figure 2.1, the ring grinding setup is placed in a Cartesian coordinate system, where the z -axis coincides with the optical axis of the generated part. The ring cutter axis is tilted in the x - z plane by an angle ϕ from the z -axis. This tilt angle is defined by the cutter radius (T) and desired part radius (R) through the simple relationship provided by Equation (1.4).

(A)



(B)

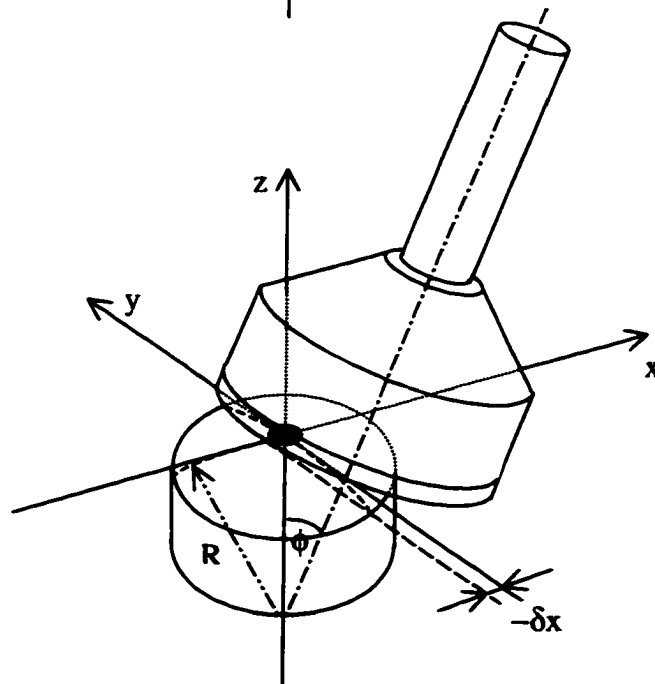


Figure 2.1. Perspective views of the grinding setup with x-direction tool misalignments:
(A) +x-error; (B) -x-error.

It can be seen from the drawings that misalignment of the ring cutter in the x -direction results in a displacement of the ring cutter edge from the vertex of the generated surface. Top views of the grinding setups are shown below in Figure 2.2. The tilted ring cutter is represented by the ellipses in the drawing. The apparent elliptical shape of the cutter is a result of the tilt. The large circles represent generated parts. The dotted portion of the ellipse represents contact between the cutter and the generated surface.

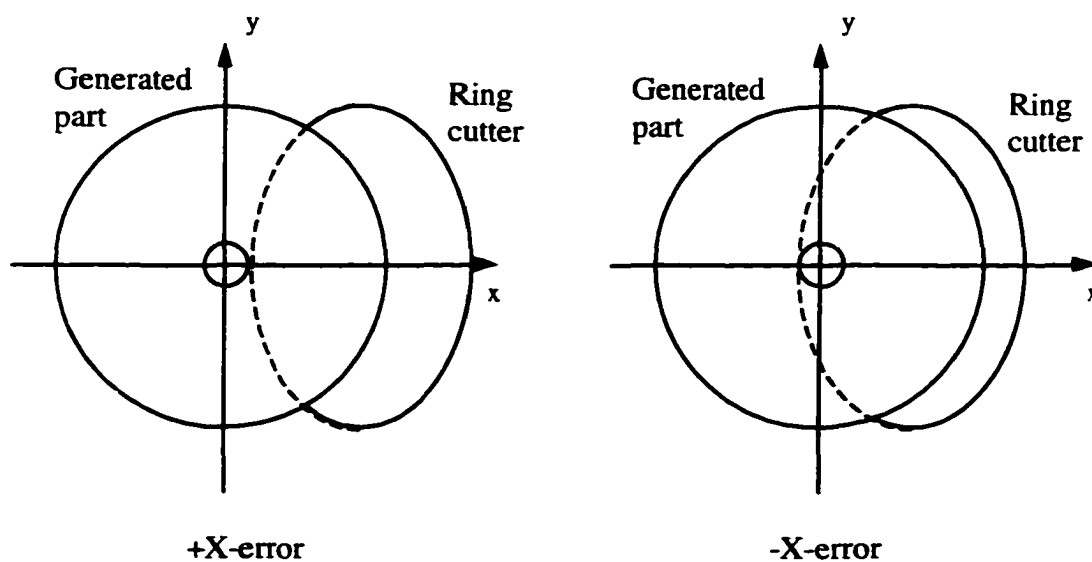


Figure 2.2. Top views of the grinding setup with x -errors.

In case of x -direction tool misalignments, the ring cutter edge will no longer coincide with the part vertex. Consequently, the finished surface will have a small region near the vertex left unground. This unground portion on the part, called the nib, is indicated in Figure 2.2 by a small circle in the center. Intuitively, this nib size on the finished surface

is linearly proportional to the amount of tool misalignment in the x-direction [Rich and Lindquist 1993].

Cutter misalignments in the x-direction also result in a radius of curvature error on the final part. Although the generated surface still has a spherical shape, the finished radius of curvature will differ from the original design value. Figure 2.3 shows the effect of the x-direction tool misalignment using a simple geometry. It shows that the x-error changes the effective tool height value (h) in the grinding setup, providing that the tilt angle of the cutter spindle is preserved. As a result, an error in the radius of curvature on the final surface is expected. The radius of curvature of the generated surface can be calculated, from Figure 2.3, in this case as for +x-error:

$$R = \sqrt{T^2 + (h + \delta h)^2} = \sqrt{T^2 + \left(\frac{T}{\tan \phi} + \frac{\delta x}{\sin \phi} \right)^2}, \quad (2.1)$$

and

$$R = \frac{1}{\sin \phi} \sqrt{T^2 + 2 \cdot T \cdot \cos \phi \cdot \delta x + \delta x^2}. \quad (2.2)$$

where:

R' = generated radius of curvature;

T = radius of the ring cutter;

ϕ = tilt angle of the cutter spindle;

δx = displacement of the ring cutter edge from the part vertex.

A x-error in the grinding setup produces a radius of curvature error on the finished surface. It also results in a nib at the vertex of the part. Tool misalignment in the x-

direction in the Opticam SX machine may be determined by evaluating either the radius of curvature error or the diameter of the nib on the test surface.

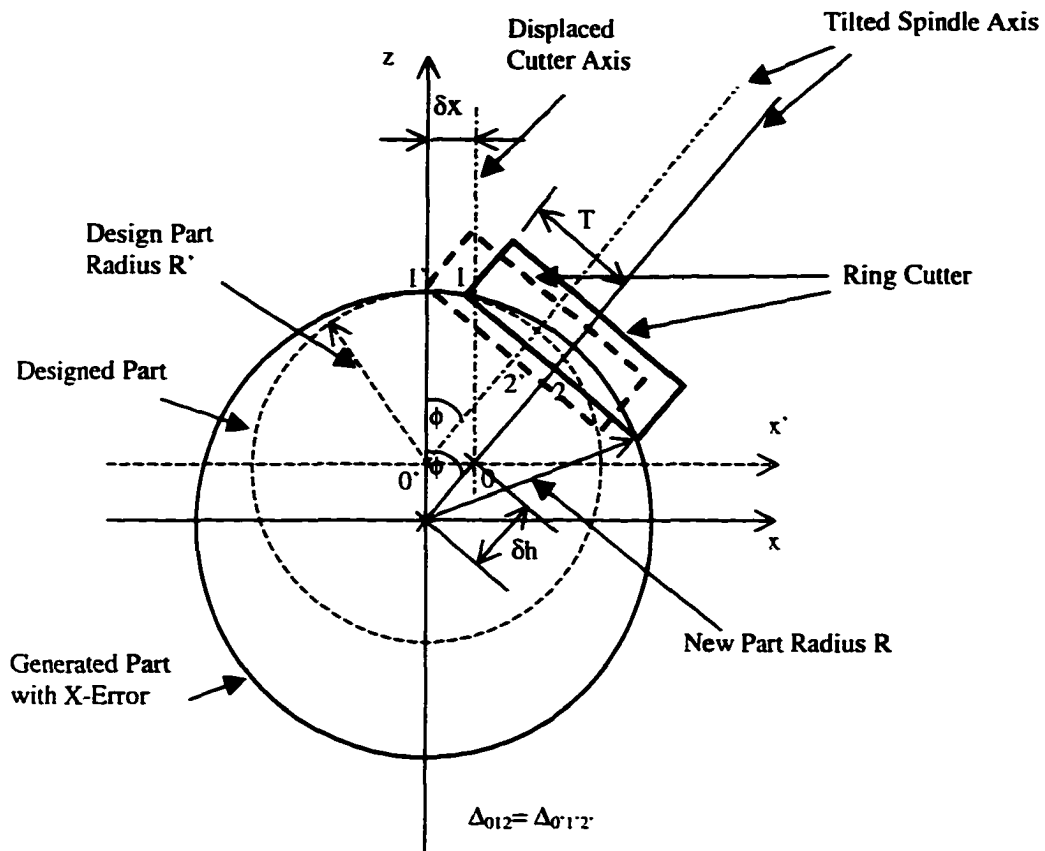
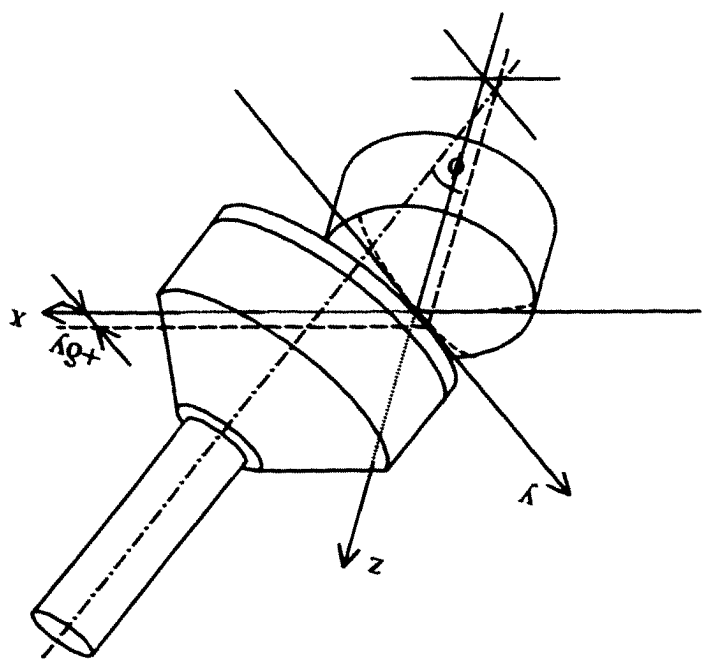
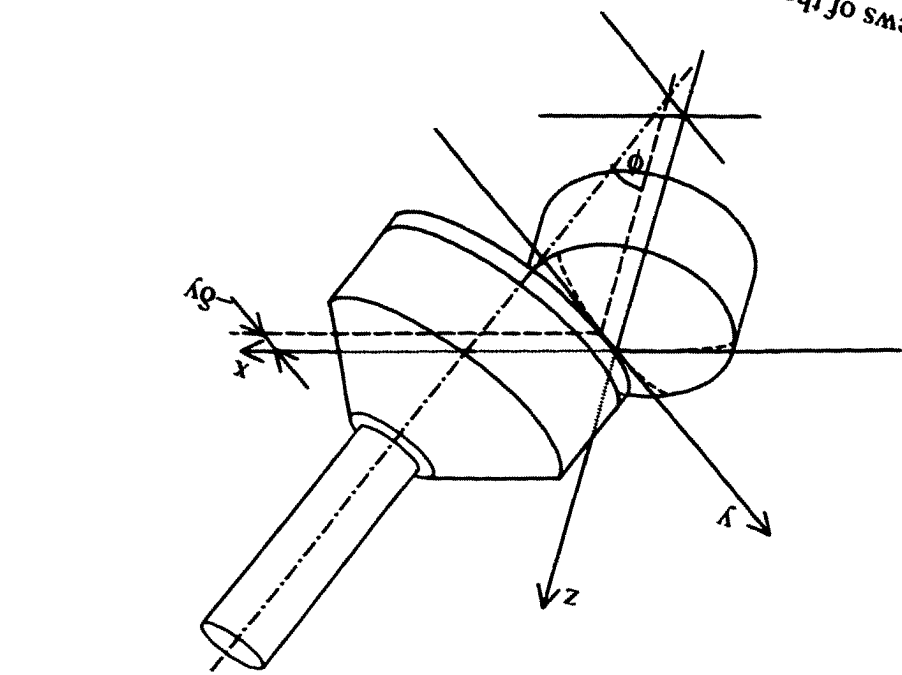


Figure 2.3. Mathematical model of the ring grinding setup with +x-error.

2.1.2 Y-direction tool misalignment

Y-direction tool misalignment is defined as the cutter alignment error in the direction that is perpendicular to the plane of the tilt of the cutter spindle axis. Schematic drawings in Figure 2.4 demonstrate the tool alignment errors in both positive and negative y-directions.

Figure 2.4. Perspective views of the grinding setup with y-direction tool misalignments:
(A) +y-error; (B) -y-error.



(B)

(A)

Top view drawings similar to the ones used for the x-errors are shown in Figure 2.5 for the y-direction tool misalignments. In the drawing, the tilted ring shape cutter is again represented by the ellipses. The large circles are the generated parts. The dotted portion of the ellipse represents the contact between the cutter and the part. Noticed that, as opposed to x-errors, y-direction alignment errors cause the cutter to contact the generated surface unevenly on either side of the ring.

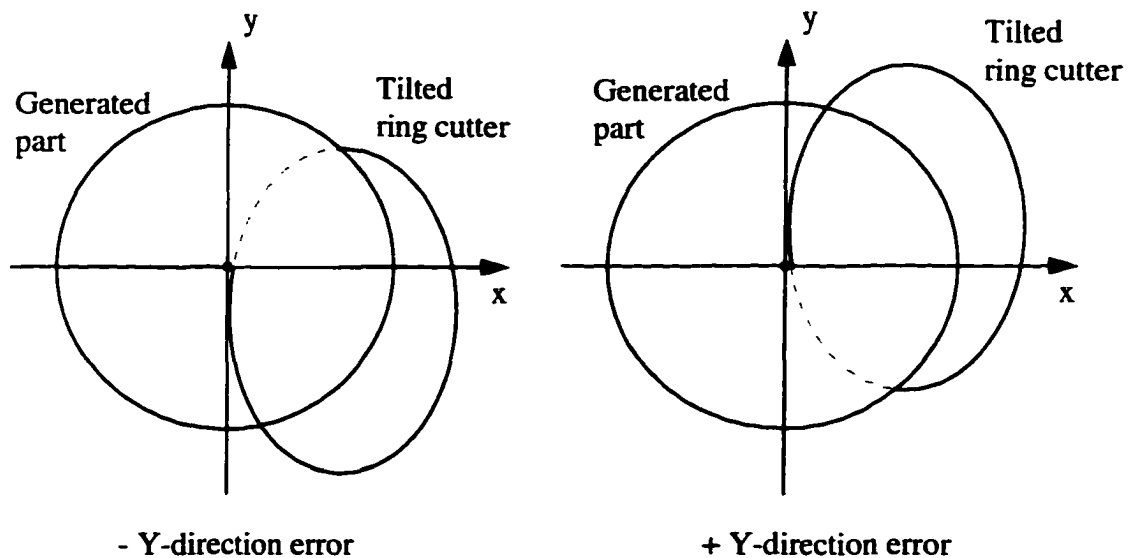


Figure 2.5. Top views of the grinding setup with y-errors.

Y-errors in the Opticam machine setup result in surfaces with non-spherical shapes, although the rotational symmetry of the surface is still preserved [Sinclair 1994; Rich and Lindquist 1993]. To a first order approximation, the surface deviation from a best-fit sphere has a conic shape. The surface contains a slope discontinuity at the vertex. The amount of this slope discontinuity is found to be linearly proportional to the amount

of tool misalignment in the y-direction (Section 5.4). Mathematically, the finished surface shape can be described by knowing the nominal radius of curvature of the finished surface and the amount of y-error in the grinding setup.

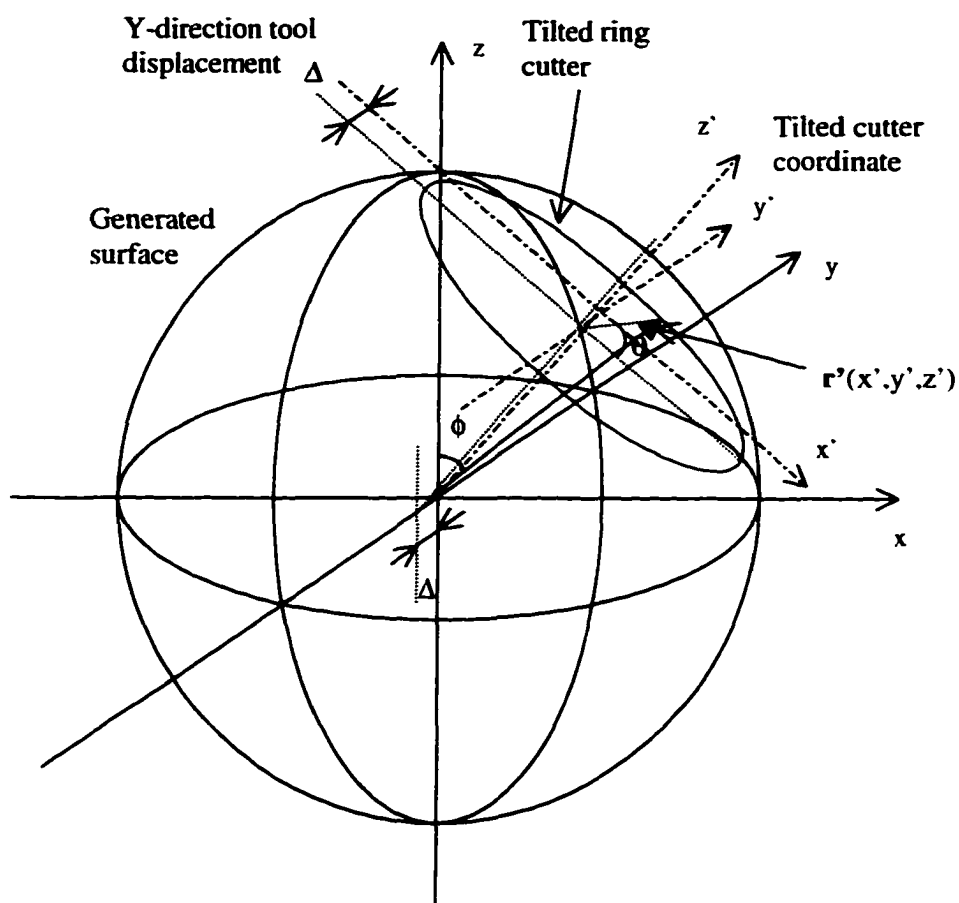


Figure 2.6. Mathematical model of the grinding setup with -y-error.

Mathematical derivation of the surface figure generated by the y-error is provided. The generated surface shape is derived from the path of the tilted ring cutter in a Cartesian coordinate system.

A vector $\mathbf{r}'(x', y', z')$ with a shift along the y' -axis is used to describe the misaligned ring cutter in the tilted coordinate system.

$$\mathbf{r}'(x', y', z') = \begin{bmatrix} x' \\ y' \\ z' \end{bmatrix} = \begin{bmatrix} T \cos \theta \\ T \sin \theta + \Delta \\ h \end{bmatrix}. \quad (2.3)$$

where:

T = radius of the ring shape cutter;

h = displacement of the cutter from its pivot center along the z' -axis;

θ = angle in the x' - y' plane from the x' -axis;

Δ = y -direction tool misalignment;

The rotation matrix M_{rot} is applied to the ring cutter matrix; and transfers it to the un-tilted part coordinate system.

$$\mathbf{r}(x, y, z) = M_{rot} \cdot \mathbf{r}'(x', y', z'), \quad (2.4)$$

$$M_{rot} = \begin{bmatrix} \cos \phi & 0 & \sin \phi \\ 0 & 1 & 0 \\ -\sin \phi & 0 & \cos \phi \end{bmatrix}. \quad (2.5)$$

where the angle ϕ is the tilt angle of the ring cutter spindle from the z -axis.

The ring cutter in the part coordinate system (x, y, z) is calculated as:

$$\mathbf{r}(x, y, z) = \begin{bmatrix} x \\ y \\ z \end{bmatrix} = \begin{bmatrix} \cos \phi & 0 & \sin \phi \\ 0 & 1 & 0 \\ -\sin \phi & 0 & \cos \phi \end{bmatrix} \cdot \begin{bmatrix} x' \\ y' \\ z' \end{bmatrix} \quad (2.6)$$

$$= \begin{bmatrix} \cos \phi & 0 & \sin \phi \\ 0 & 1 & 0 \\ -\sin \phi & 0 & \cos \phi \end{bmatrix} \cdot \begin{bmatrix} T \cos \theta \\ T \sin \theta + \Delta \\ h \end{bmatrix} \quad (2.7)$$

$$= \begin{bmatrix} T \cos \theta \cos \phi + h \sin \phi \\ T \sin \theta + \Delta \\ -T \cos \theta \sin \phi + h \cos \phi \end{bmatrix}, \quad (2.8)$$

We can rewrite the result in Equation (2.8) as:

$$x^2 + y^2 = (T \cos \theta \cos \phi + h \sin \phi)^2 + (T \sin \theta + \Delta)^2 \quad (2.9)$$

$$= T^2 \cos^2 \theta \cos^2 \phi + h^2 \sin^2 \phi + 2Th \cos \theta \cos \phi \sin \phi + T^2 \sin^2 \theta + \Delta^2 + 2T\Delta \sin \theta .$$

$$z^2 = (-T \cos \theta \sin \phi + h \cos \phi)^2$$

$$= T^2 \cos^2 \theta \sin^2 \phi + h^2 \cos^2 \phi - 2Th \cos \theta \cos \phi \sin \phi . \quad (2.10)$$

Therefore,

$$\begin{aligned} x^2 + y^2 + z^2 &= T^2 \cos^2 \theta \cos^2 \phi + T^2 \cos^2 \theta \sin^2 \phi + T^2 \sin^2 \theta \\ &\quad + 2Th \cos \theta \cos \phi \sin \phi - 2Th \cos \theta \cos \phi \sin \phi . \\ &\quad + h^2 \sin^2 \phi + h^2 \cos^2 \phi + \Delta^2 + 2T\Delta \sin \theta \end{aligned} \quad (2.11)$$

By simplifying Equation (2.11), we get:

$$x^2 + y^2 + z^2 = h^2 + T^2 + \Delta^2 + 2T\Delta \sin \theta$$

$$= h^2 + T^2 + \Delta^2 \pm 2T\Delta \sqrt{1 - \cos^2 \theta} . \quad (2.12)$$

From Equation (2.8), we obtain the relationship shown in Equation (2.13). We may then solve for angle θ in terms of the parameters defined in the grinding geometry (Equation 2.14).

$$z = -T \cos \theta \sin \phi + h \cos \phi. \quad (2.13)$$

$$\cos \theta = \frac{h \cos \phi - z}{T \sin \phi}. \quad (2.14)$$

We also have:

$$\sin \theta = \pm \sqrt{1 - \cos^2 \theta} = \pm \sqrt{1 - \left(\frac{h \cos \phi - z}{T \sin \phi} \right)^2}. \quad (2.15)$$

Y-direction displacements of the ring cutter cause uneven contact of the ring cutter with the generated part on either side of the edge. Under this condition, the generated surface figure will be defined by the side of the cutter that has the shortest distance from the center of rotation of the part. Therefore, the smaller value of Equation (2.12) should be picked and the negative values of $(\sin \theta)$ must be used to realize this situation.

Finally, a surface generated by the Opticam machine with y-direction tool misalignments can be described as:

$$\begin{aligned} x^2 + y^2 + z^2 &= h^2 + T^2 + \Delta^2 + 2T\Delta \sin \theta \\ &= h^2 + T^2 + \Delta^2 - 2T\Delta \sqrt{1 - \left(\frac{h \cos \phi - z}{T \sin \phi} \right)^2} \end{aligned}$$

$$\begin{aligned}
&= h^2 + T^2 + \Delta^2 - \frac{2\Delta}{|\sin \phi|} \sqrt{T^2 \sin^2 \phi - (h \cos \phi - z)^2} \\
&= R_0^2 + \Delta^2 - \frac{2\Delta}{|\sin \phi|} \sqrt{T^2 \sin^2 \phi - (h \cos \phi - z)^2} .
\end{aligned} \tag{2.16}$$

This surface has a non-spherical shape and a rotational symmetry about the z-axis. In the x-z plane ($y=0$), a radial profile of the surface is:

$$x^2 + z^2 = R_0^2 + \Delta^2 - \frac{2\Delta}{|\sin \phi|} \sqrt{T^2 \sin^2 \phi - (h \cos \phi - z)^2} , \tag{2.17}$$

Equation (2.17) contains three terms on the right-hand side. The first term (R_0) represents the nominal radius. The second term (Δ) produces a radius error on the finished surface. Because of the absolute value, the last term in the equation produces a symmetric non-spherical surface figure error. It describes the conical shape added to the surface, which results in a slope discontinuity at the vertex.

Figure 2.7 shows an error map of an Opticam generated part with 100 μm of y-direction tool misalignment. The part is measured using a phase shifting interferometer. Tilt and best-fit curvature are removed from the raw measurement data. The cone shape of the surface error can be seen clearly near the center of the error map. This conical surface error produces a slope discontinuity at the vertex of the surface.

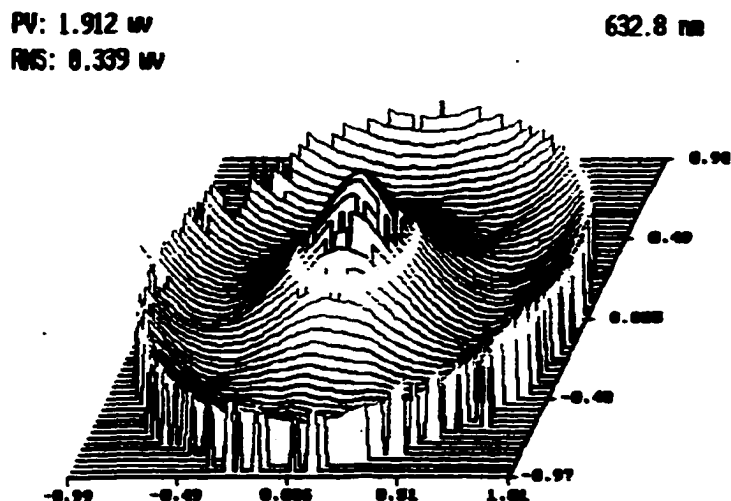


Figure 2.7. Surface error map of a part generated with 100 μm y-error.

It is necessary to realize that the “w” shape of the surface error shown in the above figure does not imply high points at the edge of the surface. It rather indicates a smaller departure of the surface from the best-fit sphere. Figure 2.8 demonstrates the best-fit sphere removal process for a surface with a near conical shape. The surface may be considered as a highly exaggerated representation of an Opticam generated surface with y-error. A profile of the surface is shown in the drawing, and the dotted circle is the best-fit sphere. The deviation between the two curves is the shape error of the original surface from its best-fit sphere. A plot of this surface figure error is also provided in Figure 2.8. The purpose of this drawing is to demonstrate the origin of the “w” shape error for Opticam generated surfaces with y-direction tool misalignments, and explain the 2D surface error map shown in Figure 2.7.

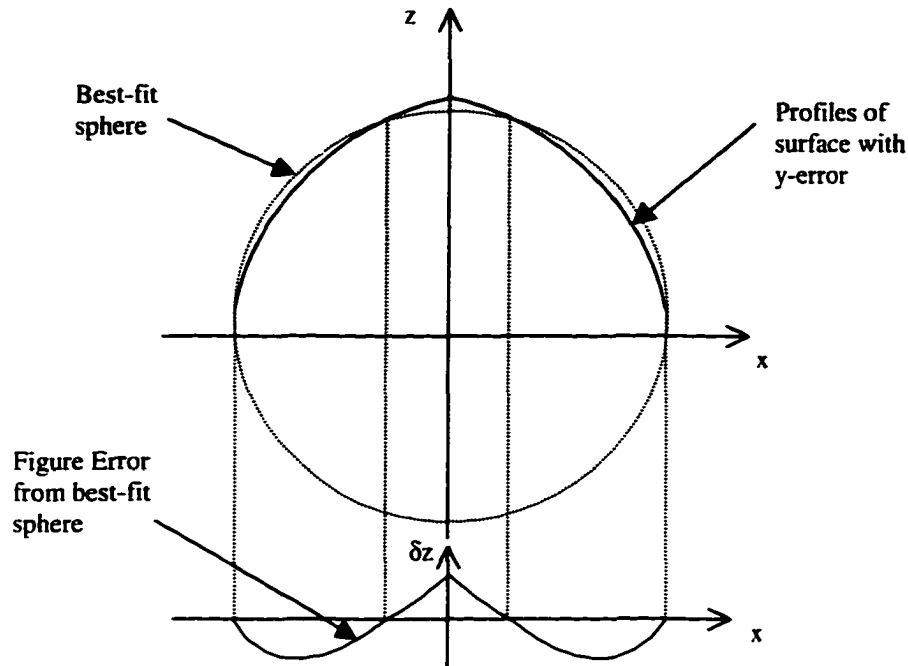


Figure 2.8. Surface error produced by y-direction tool misalignment.

It is realized that y-direction tool misalignment in either a positive or a negative direction results in the same amount of figure error on the final part. This feature of the y-error can be observed from Equation (2.16), where only the absolute value of the y-error ($|\Delta|$) is used in the surface description.

The sign of the y-errors cannot be identified from the magnitude of the surface errors. However, vibration of the cutting tool and the workpiece in the Opticam machine result in cutter marks on Opticam finished surfaces [Lambropoulos 1993; Stevens 1993; Lambropoulos and Golini, 1994]. Due to the uneven contact of the cutter from y-errors, different orientations of the cutter marks may be observed on the finished surface.

When the cutting tool is misaligned in the positive y-direction, only the trailing edge of the ring tool will be in contact with the surface. A spiral pattern of marks will be produced. A cutter misalignment in the negative y-direction will produce a set of cutter marks that spiral in the opposite direction. A crossed flower shape pattern is seen when the grinding setup contains no y-error (Figure 2.9). Hence, by inspecting the orientation of the cutter marks, the contact side of the cutter can be found and the direction of the y-error may be determined.

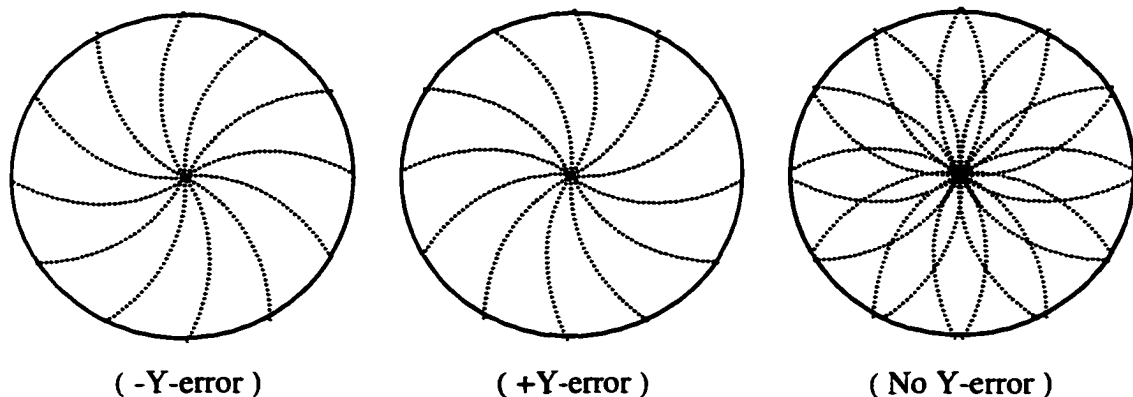


Figure 2.9. Cutter marks on Opticam generated surfaces.

Peak-to-valley (PV) and RMS errors on an Opticam generated surface with a given amount of y-errors can be calculated from Equation (2.16) after removing the best-fit curvature. It can be shown that the PV error on the surface is linearly proportional to the amount of tool misalignment in the y-direction [Sinclair 1994]. A plot of the PV error of surfaces with increasing amount of y-error and a fixed radius of curvature is shown in Figure 2.10. R/2 surfaces were used; machine dwell errors were not included in this calculation. The R number of a surface is defined as the ratio of the base radius of the

surface and the diameter of the clear aperture of the surface. An R/0.5 surface represents a hemisphere.

It is also noticed that sensitivity to the y-error decreases as the base radius of the generated surface increases. Surface errors produced by the same amount of y-error are less significant on surfaces with longer radii of curvatures. Flat surfaces are not sensitive to y-errors at all.

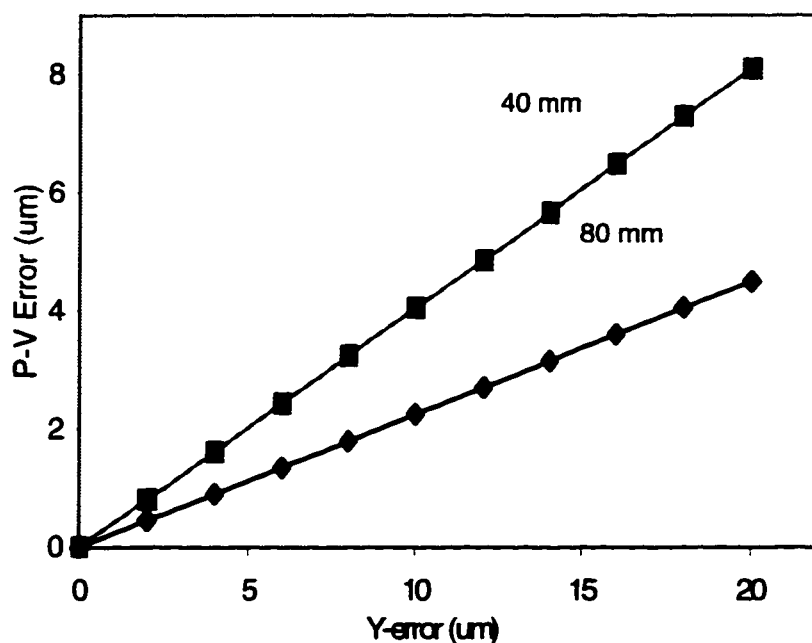


Figure 2.10. Surface PV error vs. y-error for R/2 surfaces.

Y-errors are important due to their nature of producing surfaces with non-spherical shapes. The magnitude of the existing amount of y-direction tool misalignments in the

Opticam system may be determined from the measured PV surface errors on an Opticam generated surface using the linear relationship between the two quantities.

2.2 OTHER SOURCES OF ERRORS

Static tool misalignments are not the only sources of error in producing parts with unexpected shapes. When ring cutter is perfectly aligned with the spindle axis of the part, final parts may still have figure errors. The errors may come from uncertainties in the ring tool diameter and the cutter tilt angle. Tool wear during the grinding also has a serious impact on the finished surface shape. Typically, these errors result in a radius of curvature error on the finished part. Machine dwell of the tool over the vertex of the generated surface is also important. It tends to produce a central dip at the vertex of the finished surface. The generated part will have a "m" shape error, as opposed to the "w" shape error seen for y-errors, when machine dwell error is significant.

2.2.1 Errors in the tool radius and the tilt angle

We have shown in Section 1.2 that the radius of curvature of a ring tool generated surface is defined by the ring tool radius and its tilt angle through a relationship:

$$R = \frac{T}{\sin(\phi)} \quad (2.18)$$

where:

R = desired radius of curvature of the finished surface,

T = radius of the ring shape cutter,

ϕ = tilt angle between the cutter spindle and the part spindle.

When uncertainties exist in the radius of the ring cutter or the tilt angle of the cutter, surfaces generated will have radius of curvature errors. Tool radius error produces an error in the radius of curvature on the final surface, and it can be calculated as:

$$T = T + \delta T, \quad (2.19)$$

$$\delta R = \frac{1}{\sin \phi} \cdot \delta T \quad (2.20)$$

A cutter tilt angle error in the grinding setup also produces a radius error on the final part (Equation 2.22).

$$\phi' = \phi + \delta\phi, \quad (2.21)$$

$$\delta R = \frac{T \cos \phi}{\sin^2 \phi} \cdot \delta\phi. \quad (2.22)$$

For small tool radius and tilt angle errors, higher order radius of curvature errors may be neglected. To a first order approximation, both tool radius error and the tilt angle error

produce radius of curvature errors on the final parts that are linearly proportional to the magnitude of the errors when static tool misalignments are ignored.

Tool wear during the grinding process also produces shape errors on the finished parts. Tool wear effectively changes the tool radius and bevel the edge of the ring cutter. Depending on the alignment condition, a nib may be produced at the vertex as in the x-error case [Sinclair 1994].

2.2.2 Machine dwell error

For a perfectly aligned ring grinding setup, the ring edge cutter is constantly in contact with and removing materials from the vertex or center of the generated surface during surface generation. As a result, machine dwell process tends to produce a low point at the vertex of the finished part. An error map of a part with machine dwell error is shown in Figure 2.11. It is noticed that the machine dwell error produces surface deviation from the best-fit sphere that is exactly opposite to the type of error resulted from the y-direction tool misalignment. Surface errors produced by machine dwell are generally small, typically half of a micrometer peak-to-valley. This error is observed only when the static tool alignment errors are small.

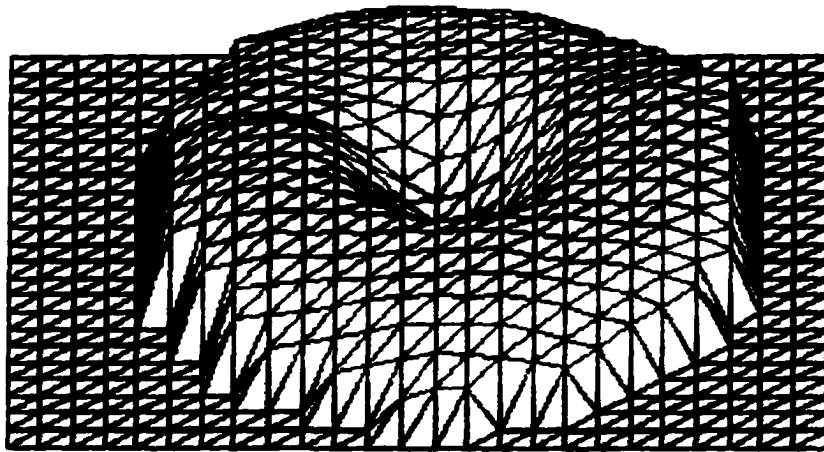


Figure 2.11. Surface error map of a part with machine dwell error.

The existent of this machine dwell error prevents the production of surface with a perfect figure, even when machine alignment errors are eliminated. However, it has been found that this error may be used to balance the tool misalignment errors in the machine setup to achieve best overall surface figure. The balance between the machine dwell error and the tool alignment error will be discussed in detail in Chapter 7.

2.3 TOOL MISALIGNMENT DETECTION SYSTEM

In order to achieve high accuracy and efficiency in optical surface finishing for the Opticam machine, it is necessary for the generated parts to have minimal figure errors before polishing. Static tool alignment errors in the grinding process must be detected and corrected. Y-direction tool misalignments produce parts with non-spherical shapes.

They are considered more important compared to other types of machine setup errors. This dissertation will emphasize the detection of the y-direction tool misalignments.

Current tool alignment control process requires the machine operator to generate sample parts, which are remotely measured in the metrology lab. Interferometers or mechanical stylus profilers are commonly used to determine figure errors on the finished parts. Based on the cutter mark patterns on the surface and measured figure errors, the operator can determine the types and the amount of alignment errors in the setup. Spherometers are also used in practice to determine tool alignment errors in the Opticam machine. They are used to measure radius of curvature errors across the finished parts. Tool misalignment errors are estimated from the detected part radius error. This technique does not require the workpiece to be removed from the grinding setup. However, because of the lack of simple conversion between the radius error and the tool alignment errors, the accuracy of the tool error estimation relies heavily on the experience of the machine operators.

Current tool misalignment detection techniques require several iterations before the machine is accurately aligned. Productivity of the Opticam system is greatly limited. Moreover, due to the long cycle time of these tests, frequent system alignment checkup is practically prohibited. A fast and accurate detection system is needed for this task.

An ideal detection system is considered to have the ability to detect surface errors and relate them to the amount of tool misalignments in the grinding setup. It must be able to conduct measurement on-line without removing the test surfaces from the generator. The detection procedure must be fast, possibly during the tool change, without affecting the production of the Opticam generator. The system should be able to provide real-time feedback to the Opticam machine operator and allow real-time control of the machine geometry to correct tool misalignments.

The on-line metrology system is required to use a non-contact detection method. It must have a non-rigid metrology frame; so it can be adapted into the existing machine system. The system must also be compatible with the wet machine environment, and not sensitive to machine vibrations. The system should be applicable to surfaces with various states of surface finish from ground to polished. Most importantly, this system must be capable of measuring surfaces with a variety of radius of curvature ranging from concave to convex.

CHAPTER 3

CONVENTIONAL SURFACE METROLOGY SYSTEMS

Existing metrology systems for surface figure measurements are classified into four basic types: interferometric systems, moiré fringe projection systems, mechanical stylus profilers and moiré deflectometers. Their principles, advantages and disadvantages are briefly reviewed. It is not our intent to cover all the available metrology techniques, but the most commonly used ones. The goal of this chapter is to discuss the limitations on these systems that prevent them from being applied to the Opticam generator. At the end of this chapter, we will introduce a new metrology technique that combines the advantages and overcomes the limitations conventional systems have.

3.1 OPTICAL INTERFEROMETRIC SYSTEMS

Optical interferometric systems are built based on the interference phenomena. Two coherent wavefronts intersect in space; their amplitudes add or subtract depending on the phase difference between the two. The result of this interaction is a set of alternating bright and dark fringes, which are called interference fringes or an interferogram [Born

and Wolf 1980; Hecht 1987]. Bright fringes in the interferogram correspond to the points where the phase difference between the two interacting wavefronts is a multiple of 2π . Dark fringes correspond to the points with phase difference in multiple numbers of π . Adjacent bright or dark fringes in the fringe pattern have a 2π phase difference. An interferogram is essentially a plot of constant phase difference between the two interfering wavefronts.

In the optical interferometric systems, two interfering wavefronts are produced by a reference surface and a test surface respectively. Phase differences are produced by the optical path differences (OPD) between the two wavefronts, which directly result from the shape differences between the reference and the test surface. The distance between adjacent bright or dark fringes in the interferogram corresponds to an OPD of one wavelength. In this case, fringes in the interferogram represent contours of constant OPD between the two wavefronts, and contours of constant height difference between the test and the reference surfaces.

A schematic drawing of a Fizeau type interferometer is shown in Figure 3.1. Light reflected off the reference surface and the test surface are collected by a CCD camera. These two beams intersect in space and produce interference fringes on the CCD array. This interference pattern is stored and analyzed to determine the deviation of the test

surface from the reference. A height map of the test surface may be obtained by analyzing the interference fringe pattern and knowing the reference surface shape.

In Figure 3.1, a converging wavefront is produced at the output of the interferometer to match the shape of the test surface. For flat test, a flat reference surface will be used, and a collimated beam will be output from the interferometer [Bunnagel 1968; Malacara 1994]. Different configurations for interferometric measurements can be setup for testing flat and curved reflecting surfaces. This technique may also be used to test parts in transmission [Malacara, 1994].

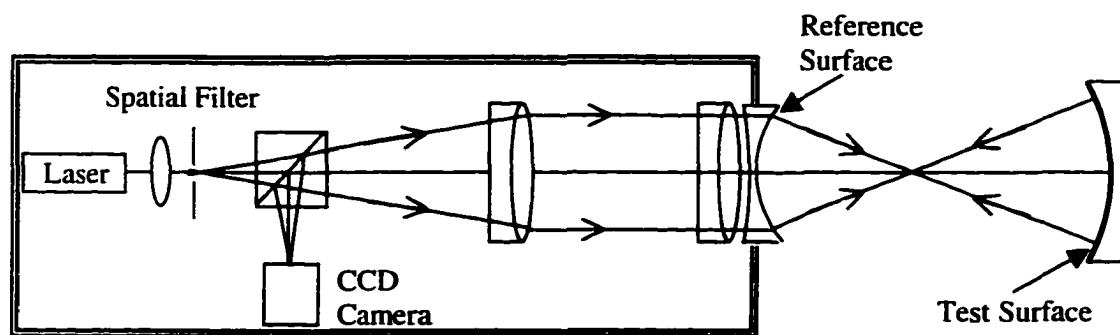


Figure 3.1. Simple Fizeau interferometer testing a concave mirror.

Modern computer technology and invention of the charged couple device (CCD) make interferometry one of the most favorite metrology techniques today. Phase shift technique enables an automated, fast and accurate way of analyzing interferograms [Bruning et. al. 1974]. A set of interferograms with a known amount of phase shift in between are captured by a CCD camera and saved in digital forms. A surface height map of the measured surface is automatically calculated from these interferograms.

The interferometric test is a relative measurement of the test surface against the reference. A larger shape difference between the test surface and the reference surface will be seen as an increase in the number of fringes in the interference pattern. The sampling frequency defined by the CCD camera and digitization process in the phase-shifting interferometers limits the maximum number of interference fringes allowed in one interferogram. In order to avoid fringe aliasing in the captured interferogram, the sampling condition described by the Whittaker-Shannon sampling theorem [see e.g. Gaskill 1978] must be met.

Although sub-Nyquist interferometry [Greivenkamp 1987; Lowman 1995] allows aliased interferograms to be used, Nyquist frequency of the sensor array is still used to define the maximum allowed fringe spatial frequency in most conventional interferometers. In other words, maximum departure and maximum slope of the test surface from the reference are limited. This restriction demands the reference surface to have almost the same shape as the test surface for interferometric measurements. As a result, a large collection of reference surfaces must be made in order to measure surfaces with different shapes. Furthermore, because an interferometer provides a relative measurement of the test surface from the reference, high quality references are required to achieve high accuracy. This requirement makes interferometers more expensive compared to other systems.

Disadvantages of the interferometric systems are their costs and environmental sensitivities. Interferometers are delicate optical instruments; they are designed to measure surface height variations as small as a few hundredths of a wavelength. They are extremely sensitive to vibrations and air turbulence, and they require both temporally and spatially coherent light sources. The working distances for the interferometric systems are usually limited. Test surfaces must be specular and the range of the measurable surface shapes depends on the availability of the reference surfaces. All these limitations prevent the interferometric systems from being used in the Opticam grinding environment.

3.2 FRINGE AND MOIRÉ PROJECTION

Fringe projection techniques [Rowe and Weldford 1967] for surface height measurements have been used for many years. They require the projection of a fringe or grating pattern on the test surfaces. Fringe shadows on the test surfaces are viewed at an angle from the direction of projection. The observed fringe patterns are interpreted as contours of constant surface height on the test surface. They can be evaluated quantitatively to obtain a 2D height map of the test surface. Projection fringe contouring technique has been covered in detail by Gasvik (1987).

Figure 3.2 shows a schematic drawing of a fringe projection setup. A collimated illumination of a straight equally spaced grating pattern is used to produce equally spaced surface contour. The shadow of the fringe patterns are view at a different direction. The departure of the viewed fringes from straight lines represent the departure of the surface from a plane reference surface [Creath and Wyant 1992]. The analysis of the viewed shadow pattern is similar to interferometry with a equivalent wavelength (λ_{eq}) instead of the optical wavelength of the light source. The equivalent wavelength of a fringe projection setup is defined by the grating period and the viewing angle:

$$\lambda_{eq} = \frac{p}{\sin \alpha} \quad (3.1)$$

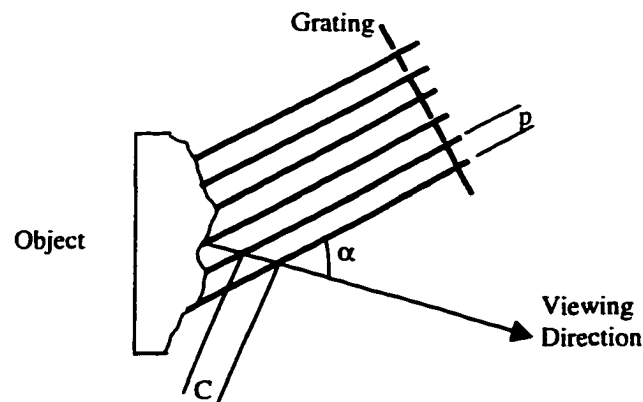


Figure 3.2. Fringe projection.

Moiré fringes are beat patterns produced by two gratings of approximately equal spatial frequency [Oster and Nishijima 1963]. This beat pattern is usually used to detect differences between the two grating patterns. Projection moiré [Brooks and Helfinger 1969] and shadow moiré techniques (see Figure 3.3) are very similar to the fringe

projection method, except that in moiré techniques projected fringe patterns on the test surface are observed through a grating. Shadow moiré uses the same grating for both projection and observation; projection moiré uses two different gratings. Interference between the grating shadows and the observation grating results in a set of moiré fringes. These moiré fringes may be used to calculate surface topography [Meadows et. al. 1970; Takasaki 1973; Chiang 1983]. Similar analogy for the fringe pattern and the equivalent wavelength used in the fringe project technique can be applied to the moiré fringe patterns seen in both the shadow moiré and the projection moiré systems.

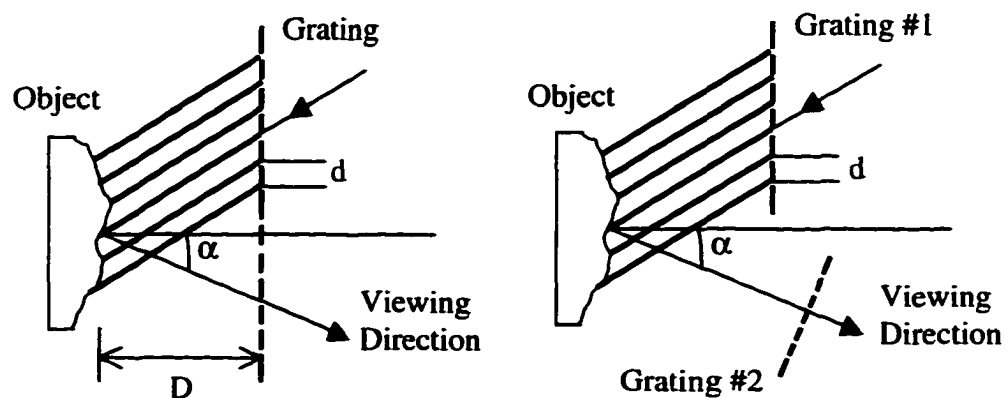


Figure 3.3. System setups for shadow and projection moiré:
(A) Shadow moiré; (B) Projection moiré.

Both moiré and fringe projection use non-contact methods to measure surface height functions. They both require a matt surface finish. The advantages of these systems are their simple structures and ability to measure rough surfaces. In addition, the working distances for these setups are usually flexible. Computer analysis of the observed fringes or moiré patterns allows an automated process for calculating surface topography.

Measurement sensitivities for both moiré and fringe projection methods varies with the projected fringe frequency and the angle between the projection and the view direction [Creath 1991; Gasvik 1987]. Higher measurement sensitivity may be achieved by increasing the spatial frequency of the projected fringes or by increasing the angle between the projection and observation directions. For a fixed grating frequency, maximum sensitivity can be obtained when the viewing direction is perpendicular to the projection direction. However, unexpected surface shadows may obstruct projected fringe patterns when viewed at a large angle, especially for steep surfaces. This results in a loss of data in the calculated surface map.

The limitations on the measurement sensitivity and the special requirements on the surface finish prohibit the application of either fringe projection or moiré projection techniques in the on-line tool misalignment detection.

3.3 MECHANICAL STYLUS PROFILER

Mechanical stylus profilers use a contact method. Surface height profiles are obtained from the height variations of the probe tip as it moved across the test surface (see Figure 3.4) [Creath and Morales 1992]. Both high frequency surface roughness and low frequency surface figure may be measured using this technique. This technique

can be used to measure surfaces with a wide range of shapes without special adjustment. It can be used to measure specular surfaces as well as ground surfaces.

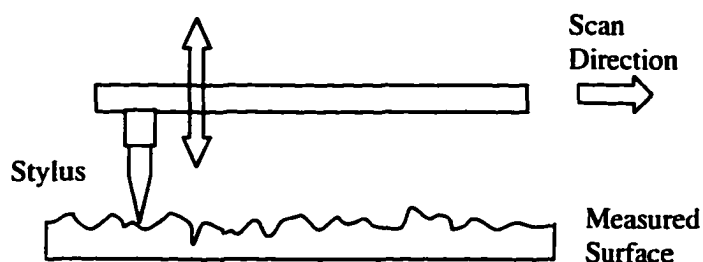


Figure 3.4. Stylus profiler.

The lateral resolution of stylus profilers is determined by the radius of the probe tip as well as the surface shape and the sampling interval between data points [Bennett and Dancy 1981]. The collected surface profile is a convolution of the actual surface profile and the probe tip due to the finite size of the probe tip. Surface height information are averaged over the tip area. Using probe with a smaller tip size will reduce this effect, although it may cause damage to the test surface due to concentrated local pressure produced by the probe tip on the surface. To ensure that the test surface is not damaged during measurement, tip size and the load of the probe tip must be adjusted, so that the test surface is not deformed. The tip size effect may also be corrected through the data analysis process for low frequency surface figure measurements.

Most stylus profilers only provide a 1D line profile of the test sample. Although 2D surface height maps may be obtained by raster scan of the entire sample, registrations

among the line scans are difficult [Creath 1992]. Finally, data acquisition time for profilometers is usually long when compared with other techniques.

Stylus surface profiler provides accurate measurement of the test surface. It is capable of measuring surface roughness with a root-mean-square (RMS) value as small as 0.5 Å with lateral resolutions of 0.1 to 0.2 μm [Creath 1992]. Post process of the collected data may be used to determine mid or low spatial frequency surface feature, e.g., waviness and surface figure. However, stylus profile technique may not be used for tool alignment detection because its long data acquisition time and requirement on the contact between the probe and the test surface.

The disadvantage of the stylus type surface profiler is the limited travel range of the probe. The maximum measurable surface height variation depends on the maximum travel allowed for the probe. The dynamic range of travel of the probe for the stylus type surface profiler is usually small. A Form Talysurf Series 2 stylus surface profiler (by Rank Taylor Hobson Ltd.) was used to obtain surface figure error and determine PV errors on all Opticam generated surfaces during our final study (Chapter 7). The measured data are used as references in calibration of the on-line detection system. This instrument has a 6 mm nominal probe travel and a 10 nm height resolution.

3.4 MOIRÉ DEFLECTOMETRY

Moiré deflectometry is used to map ray deflections caused either by a reflecting surface or by a phase object. Comparing with interferometry, moiré deflectometry response to ray deflections rather than phase retardation [Kafri 1985, 1988; Pfeifer 1995]. The advantage of this technique versus interferometry is that it is a pure geometrical method and does not require a high temporal coherent light source, although some degree of spatial coherence of the source is necessary. It has a relatively simple system setup, and has a considerably low environmental stability requirement. The measurement sensitivity of the moiré deflectometry system is also tunable.

A moiré deflectometric system (Figure 3.5) can consists of two identical Ronchi gratings separated by a distance (d). The two gratings have lines that are having angle $+\theta/2$ and $-\theta/2$ relative to the x -axis respectively. When $\theta \neq 0$, the setup is called finite moiré deflectometry. When $\theta=0$, the system is called infinite moiré deflectometry. In a moiré deflectometer, moiré fringes are formed in parallel to the y -axis with a pitch [Pfeifer 1995; Livnat 1982; Uitterdijk 1994]:

$$p' = \frac{p}{2 \sin\left(\frac{\theta}{2}\right)} \cong \frac{p}{\theta}. \quad (3.2)$$

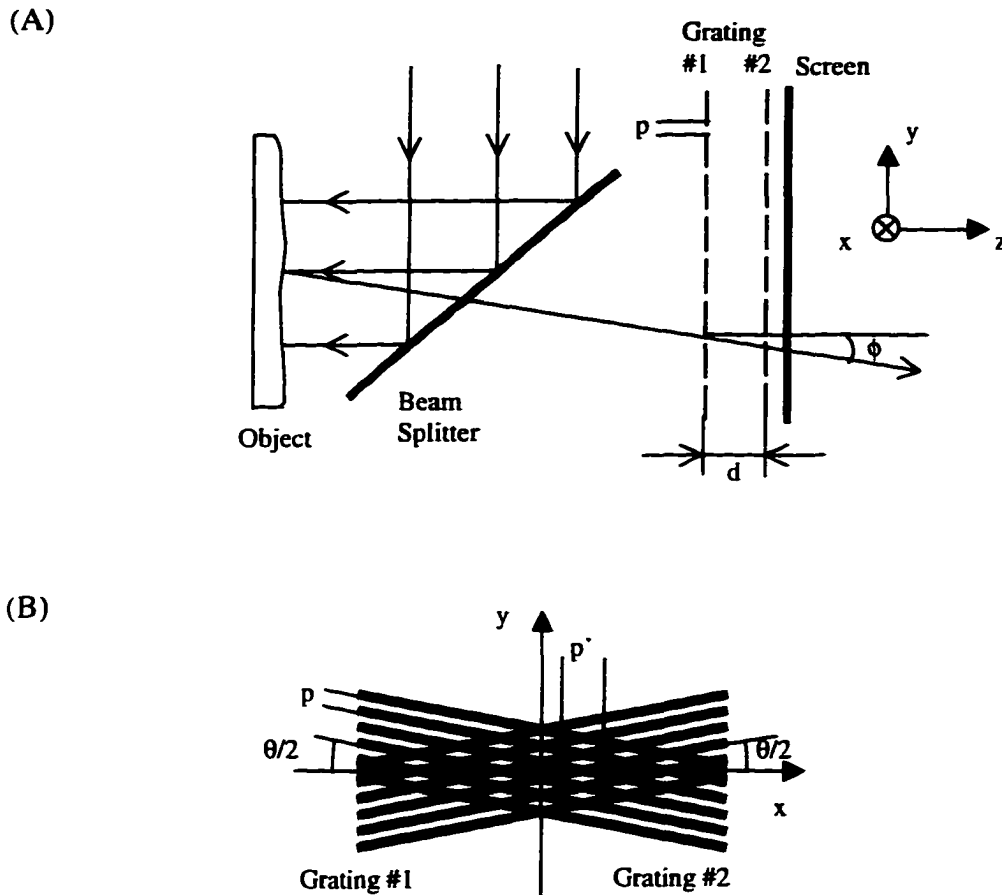


Figure 3.5. Moiré deflectometry system: (A) System setup testing a reflecting surface; (B) Observed moiré fringe pattern with no surface error.

For a reflecting surface, the collimated incident light beam is reflected through the two gratings. Surface height irregularities produce ray deflections, which result in a distorted moiré fringe pattern on the screen. The deflected ray angle ($\Phi(x,y)$) can be evaluated:

$$\Phi(x, y) = \frac{2\partial S(x, y)}{\partial y}, \quad (3.3)$$

where $S(x,y)$ is the surface height function, and the derivative is taken in the direction that is perpendicular to the grating direction. In case of a finite moiré deflectometry setup, where $\theta \neq 0$, function $\Phi(x,y)$ can be described by [Pfeifer 1995]:

$$\Phi(x,y) = \frac{2\delta h(x,y) \tan\left(\frac{\theta}{2}\right)}{d}, \quad \theta \ll 1. \quad (3.4)$$

Where $\delta h(x,y)$ denotes the deviation of the distorted moiré fringes from a straight fringe at a location (x,y) in the image plane; d is the grating separation and θ is the tilt angle between the two gratings.

Surface height function ($S(x,y)$) can be calculated by obtaining the deflection angle function ($\Phi(x,y)$). Ray deflection function ($\Phi(x,y)$) is determined from the distortions in the interference fringe pattern, called moiré deflectograms. The moiré deflectogram can be measured using several methods including intensity measuring method, automatic fringe analysis method [Servin 1990] and heterodyne detection method [Stricker 1986, 1985]. Phase shifting technique may also be applied to the moiré deflectometry systems. Using phase shift, moiré deflectograms in two orthogonal directions may be analyzed [Pfeifer 1995]. Figure 3.6 shows a schematic drawing of a moiré deflectometer system testing a concave mirror surface.

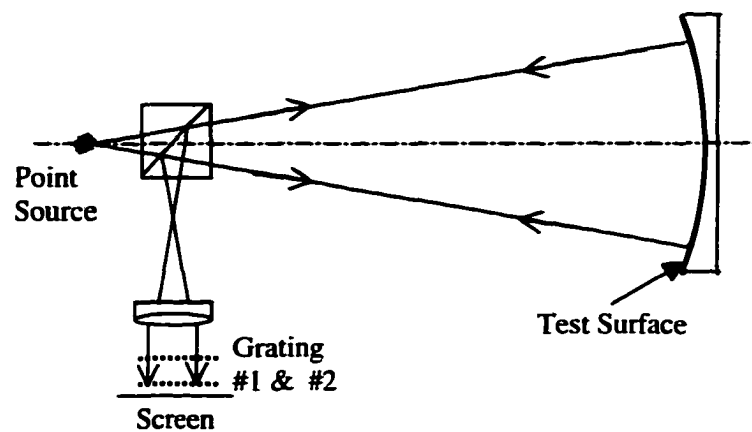


Figure 3.6. Moiré deflectometric setup for testing a concave mirror.

The moiré deflectometer is considered the simplest form of a shearing interferometer. It measures surface slope function as opposed to the surface height values measured in moiré or fringe projection systems. Moiré deflectometry has great advantages over other techniques in its simple setup, low cost, low requirements on mechanical stability, etc. However, it requires a spatially coherent source.

The observed moiré deflectogram can be analyzed using the same techniques used in interferometry. The detection sensitivity of moiré deflectometry is low when compared to interferometry. Just as for fringe and moiré projection systems, the detection sensitivity of moiré deflectometry is limited by the equivalent wavelength determined by the grating frequency, instead of the wavelength of the light source used in the detection setup.

3.5 NEW METROLOGY METHOD

Limitations of the conventional metrology systems prevent them from being used for on-line tool misalignment detection. To overcome these problems, a new metrology technique is developed. It is similar to the moiré deflectometer, although only one grating is used in the new system. It uses a non-contact detection method. Reflected images of a single grating pattern are captured and analyzed for distortions. The image analyzing process is equivalent to the moiré deflectogram analysis process. In this case, the distorted grating pattern is evaluated against a perfect virtual grating pattern generated by the computer program. From the calculated image distortions, slope function of the test surface may be obtained. The calculated surface slope function is then used to determine tool misalignment in the Opticam grinding geometry.

Different from the moiré deflectometry, the new technique does not have any special requirement on the coherent properties of the light source. There is no "shadow casting" of one grating pattern onto another. This makes the system setup even simpler. It, at the same time, inherits the advantages of the moiré deflectometry that it is a simple geometrical ray trace process. This method allows direct interpretation of the captured image and the data processing routine is simple.

The detection sensitivity of the new technique is tunable by varying the frequency of the imaged fringe pattern or the distance between the test surface and the target. This new technique has a simple and flexible layout structure, and it can be easily adapted to the Opticam machine environment. The detection system also has a low requirement on the machine stability. Most importantly, this technique may be used to measure surfaces with an essentially unlimited range of radius of curvature, from concave to convex.

Theoretical description of this new technique is discussed in the Chapter 5.

CHAPTER 4

INTERFERENCE FRINGE ANALYSIS METHODS

Automated interference fringe analysis involves calculation of the phase functions of the interferograms. Direct phase calculation provides a fast and accurate way for interferogram evaluation. It is a factor of ten to a hundred more accurate compared to the fringe position digitization process [Greivenkamp and Bruning 1992; Robinson and Reid 1993; Creath 1991]. Basic techniques used in fringe phase measurements can be classified into two types: temporal method and spatial method. In the spatial methods, the phase information is separated across the image plane in one interferogram. In the temporal methods, on the other hand, the phase information is separated into a time sequence of several interferograms [Kujawinska 1993]. Spatial fringe analysis methods are preferred for our application over the temporal methods because that they do not require special phase shifting hardware and multiple interferograms. Phase information can be retrieved from single fringe pattern.

In this chapter, we will review two spatial fringe analysis methods. The techniques discussed require no phase shifting or phase stepping [see e.g. Robinson and Reid 1993]; only one frame of interferogram is necessary to obtain a 2D phase map of the test

surface. The two techniques reviewed are: spatial synchronous method and Fourier method. Theories behind these two methods and their advantages and disadvantages will be discussed.

4.1 SPATIAL SYNCHRONOUS METHOD

Phase information in an interferogram may be retrieved by heterodyning the phase-modulated image with a perfectly sinusoidal fringe pattern with the same spatial frequency [Ichioka and Inuiya 1972; Mertz 1983; Womack 1984; Malacara and Devore 1992].

For a fringe pattern with an unknown phase modulation, the intensity function of the image can be expressed as:

$$I(x, y) = I_0 + I'(x, y) \cos(2\pi\xi x + \phi(x, y)), \quad (4.1)$$

where ξ is the carrier frequency of the fringe pattern. This fringe pattern contains an intensity modulation only in the x-direction. I_0 is the DC intensity and $I'(x,y)$ is the intensity modulation in the image. Both I_0 and $I'(x,y)$ are real functions. The phase function related to the part or the wavefront shape resides in the cosine function as $\phi(x,y)$.

Two reference signals with the same spatial frequency as the $I(x,y)$ in the x-direction used for the heterodyning are written as:

$$R_1(x, y) = \cos(2\pi\xi x); \quad (4.2)$$

and

$$R_2(x, y) = \sin(2\pi\xi x). \quad (4.3)$$

Products of the original fringe pattern with either of the reference signal result in:

$$\begin{aligned} I(x, y)R_1(x, y) &= I_0 \cos(2\pi\xi x) + \left(\frac{I'(x, y)}{2} \right) \cos(4\pi\xi x + \phi(x, y)) \\ &+ \left(\frac{I'(x, y)}{2} \right) \cos(\phi(x, y)) \end{aligned} \quad (4.4)$$

and

$$\begin{aligned} I(x, y)R_2(x, y) &= I_0 \sin(2\pi\xi x) + \left(\frac{I'(x, y)}{2} \right) \cos(4\pi\xi x + \phi(x, y)) \\ &+ \left(\frac{I'(x, y)}{2} \right) \sin(\phi(x, y)) \end{aligned} \quad (4.5)$$

Low pass filtering of these two new signals (Equations 4.4 & 4.5) yields:

$$S_1(x, y) = \left(\frac{I'(x, y)}{2} \right) \cos(\phi(x, y)), \quad (4.6)$$

and

$$S_2(x, y) = \left(\frac{I'(x, y)}{2} \right) \sin(\phi(x, y)). \quad (4.7)$$

The 2D phase information ($\phi(x, y)$) can then be computed from the ratio of these two signals:

$$\phi(x, y) = \tan^{-1} \left[\frac{S_2(x, y)}{S_1(x, y)} \right]. \quad (4.8)$$

Due to the definition of the arctangent function, where the return values are limited to be within the $-\pi/2$ to $\pi/2$ period regardless of the actual phase values. Phase discontinuities will be seen in the calculated raw phase map using Equation (4.8). A phase unwrapping process must be taken to correct this error in order to obtain the correct phase function of the interferogram. The phase unwrapping technique is described in Section 4.3.

4.2 FOURIER TRANSFORM METHOD

Fourier transform method of fringe analysis was originally demonstrated by **Takeda et. al. (1982)**. Fourier transform of a given fringe pattern is used to extract phase information. In digital computing process, a Fast Fourier Transform (FFT) [see e.g. **Cooley 1992**] routine is used to realize this calculation.

The theory behind this method is that a Fourier transform of an image contains both the phase and the carrier frequency information of the image. For a uniform periodic bar target, there is essentially one fundamental frequency component. The carrier frequency information of the image can be separated from the phase by shifting the harmonic component to the origin in the spatial frequency domain. An inverse Fourier transform of the shifted function yields the phase values as a function of the position in the image.

A mathematical proof of this algorithm is shown below. The intensity distribution of a sinusoidal bar image with unknown phase distortions can be mathematically expressed as:

$$I(x, y) = I_0 + I'(x, y) \cos(2\pi\xi x + \phi(x, y)) \quad (4.9)$$

or in the exponential form:

$$I(x, y) = I_0 + c(x, y)e^{i2\pi\xi_0 x} + c^*(x, y)e^{-i2\pi\xi_0 x} \quad (4.10)$$

where:

$$c(x, y) = \frac{1}{2} \Gamma(x, y) e^{i\phi(x, y)}. \quad (4.11)$$

This bar image has a carrier frequency represented by ξ . I_0 represents the DC intensity. $\Gamma(x, y)$ is the intensity modulation in the bar image, and it is a real function. The phase function resides in the exponential function as $\phi(x, y)$.

A Fourier transform of this image intensity function (Equation 4.10) gives a δ -function [see e.g. Gaskill 1978] as the DC component of the image and a pair of shifted transform functions $c(x, y)$ at the spatial frequencies $\pm\xi_0$.

$$\tilde{I}(\xi, \eta) = I_0 \delta(\xi, \eta) + \tilde{c}(\xi - \xi_0, \eta) + \tilde{c}^*(\xi + \xi_0, \eta) \quad (4.12)$$

By using a filter function in the spatial frequency domain, the function $\tilde{c}(\xi, \eta)$ can be isolated and shifted to the origin to remove the carrier frequency. The DC and the $\tilde{c}^*(\xi, \eta)$ terms in Equation (4.12) are eliminated. We end up with a new spectral distribution function as:

$$\bar{I}_{\text{new}}(\xi, \eta) = \bar{c}(\xi, \eta) \quad (4.13)$$

An inverse Fourier transform of this new function gives the original function $c(x,y)$ (Equation 4.13).

$$I_{\text{new}}(x, y) = c(x, y) \quad (4.14)$$

The phase values can then be determined from the arctangent of the ratio of the imaginary and real parts of the $c(x,y)$ function in modulo 2π as shown in Equation (4.15).

$$\phi(x, y) = \tan^{-1} \left\{ \frac{\text{Im}[c(x, y)]}{\text{Re}[c(x, y)]} \right\} \quad (4.15)$$

The above derivation is a two dimensional analysis. Single dimension analysis of the image is also used, because the fringe carrier frequency is in x-direction only. Besides, a 2D FFT takes significantly longer time than a 1D process. However, a 2D Fourier transform provides better signal to noise ratio and signal separation than the 1D process [Nugent 1985; Bone et. al. 1986].

Following example demonstrates the phase calculation process using the Fourier transform method. The FFT calculation for this example is conducted in a 1D form along individual rows of the image to reduce the computation time. The phase function of a distorted image of a sinusoidal bar pattern (see Figure 4.1) is calculated.

The Fourier transform of the original image provides a representation of the image in the spatial frequency space (Figure 4.2). This image spectrum is filtered by a rectangular bandpass filter and then shifted to the origin in spatial frequency space (Figure 4.3). An inverse transform of the filtered spectrum is then used to calculate the phase map of the original image (Figure 4.4).

The calculated raw phase function contains discontinuities (see Figure 4.4) due to the wrapping of the arctangent function. This error must be unwrapped to achieve corrected phase values. A 2D phase unwrapping process is completed for this example. Phase maps of the original image before and after the phase unwrapping are shown in Figure 4.4 and Figure 4.5.

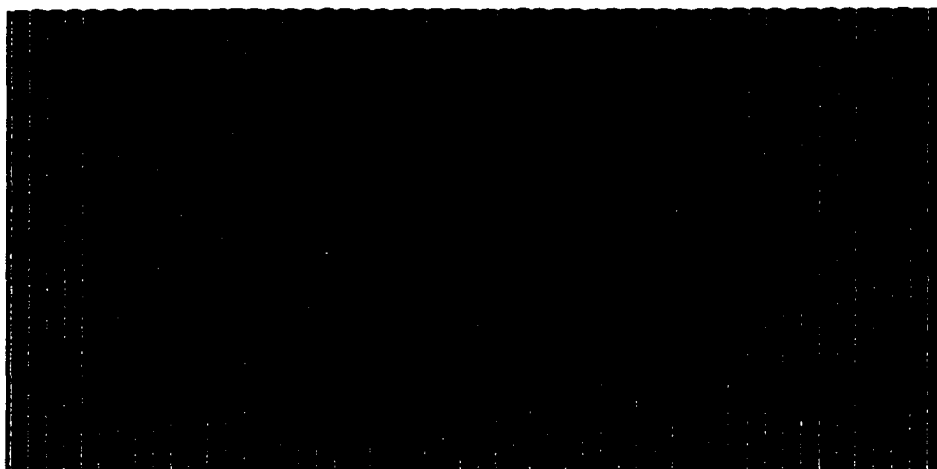


Figure 4.1. Distorted bar image.

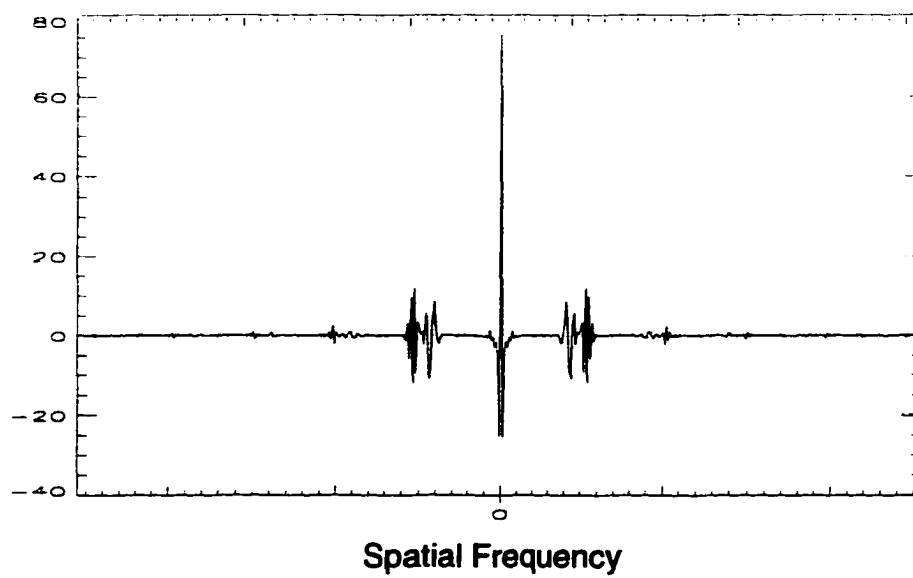
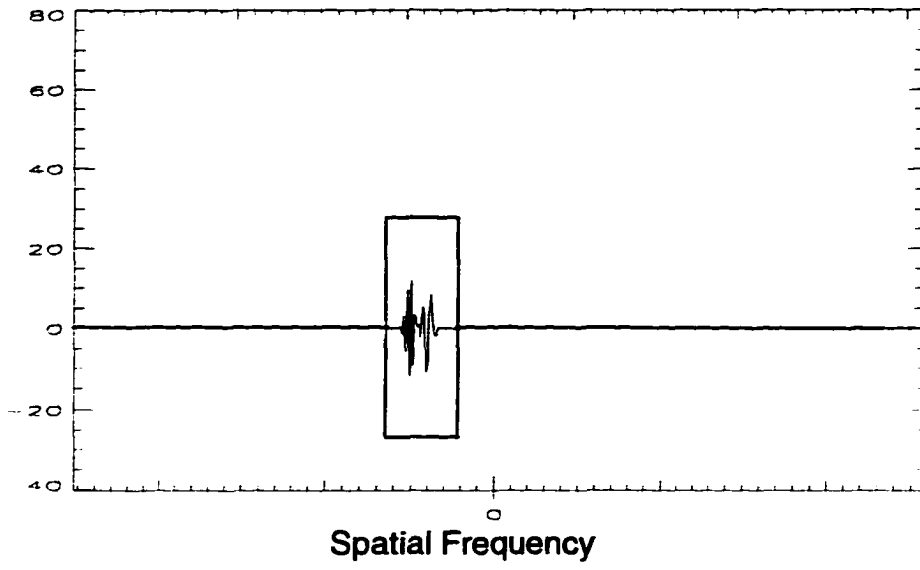


Figure 4.2. Spatial frequency spectrum of the distorted image along a horizontal line.

(Filtered Frequency Spectrum)



(Shifted Frequency Spectrum)

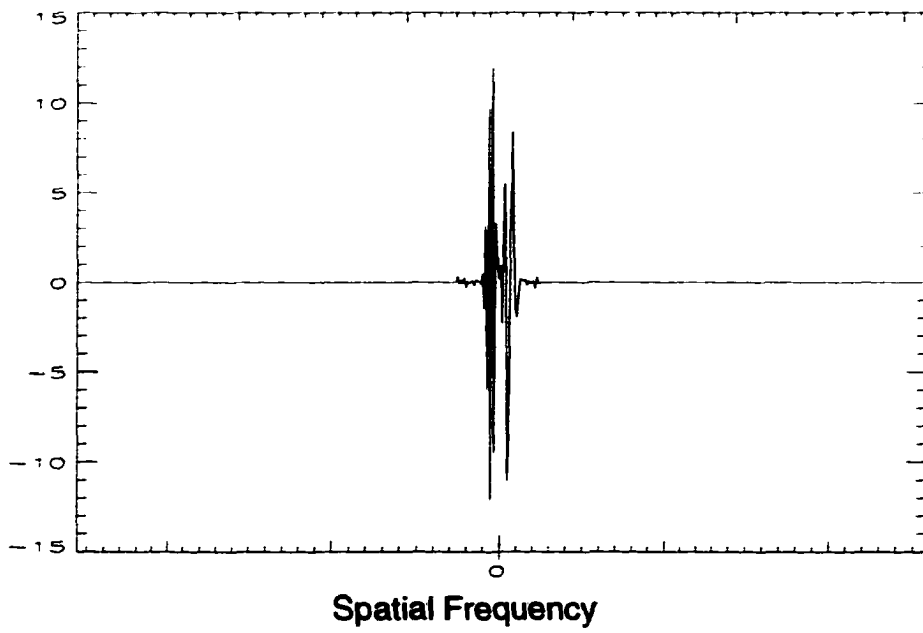
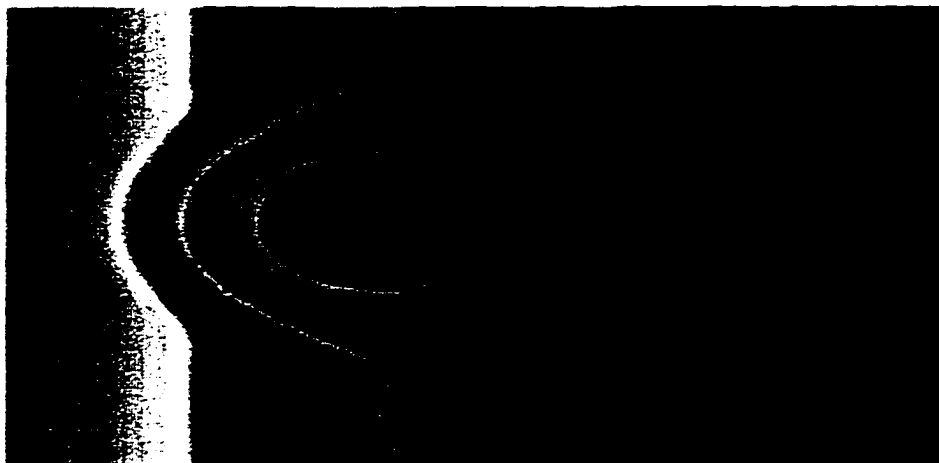


Figure 4.3. Filtered and shifted spectrum.

(A)



(B)

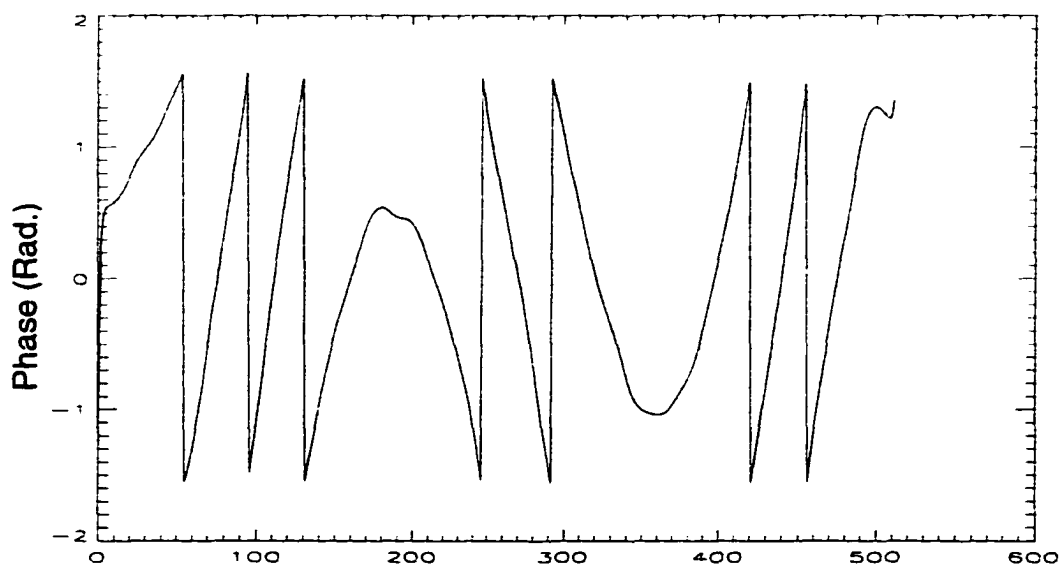
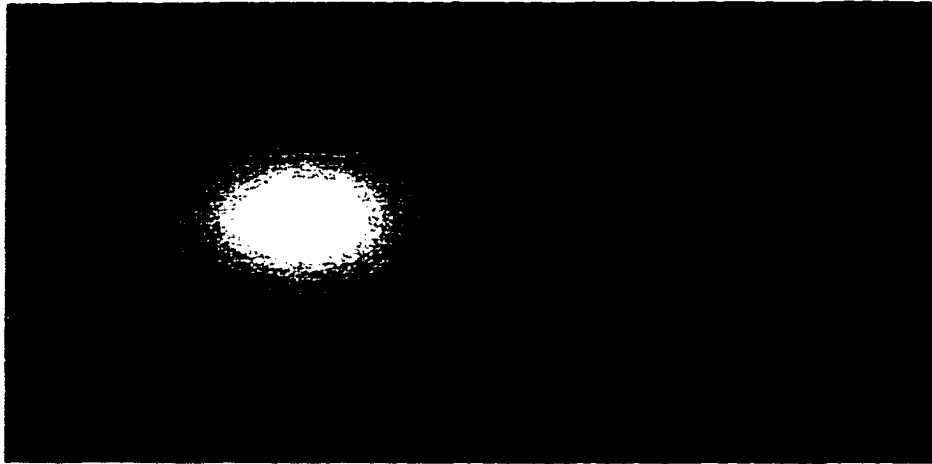


Figure 4.4. Calculated raw phase function: (A) 2D phase map;
(B) Line profile of the phase map.

(A)



(B)

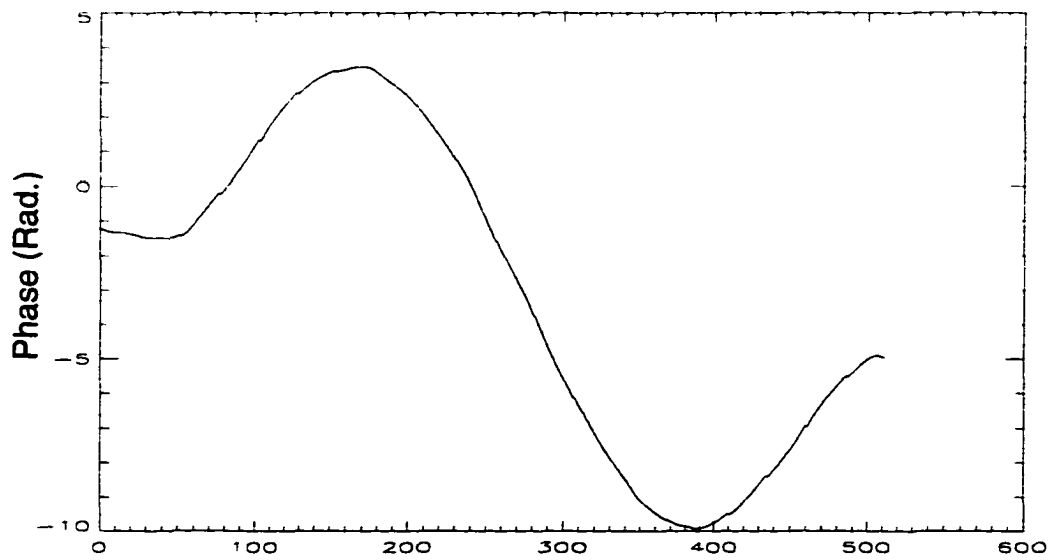


Figure 4.5. Unwrapped phase function: (A) 2D phase map; (B) Line profile of the phase map.

The advantage of the Fourier transform method is that only a single interferogram is necessary to calculate a 2D phase function of the image. No special phase shift process and hardware is required. It can also be used for real time image processing. The difficulty in this technique, however, is the determination of the spatial carrier frequency and the selection of the proper spatial filter size and shape [Robinson and Reid 1993].

4.3 PHASE UNWRAPPING

Both the spatial synchronous detection and the Fourier transform method require correction of the phase wrapping problems in the calculated raw phase map. Definition of the arctangent function limits the calculated phase values from Equation (4.7) to be within the $-\pi/2$ to $\pi/2$ period, regardless of the actual phase values. This limitation restricts us to measure distortions to no more than π radians. However, by assuming that the phase change in the wavefront between adjacent points is less than π , the phase discontinuities in the raw phase map can be removed. This assumption is equivalent to assuming a continuous test surface or that the Nyquist sampling rate is met.

A 1D phase unwrapping process starts by extend the calculated phase range to 0 to 2π period by independently evaluating the sign of the real and the imaginary parts of function $c(x,y)$. Then the new phase function is evaluated point by point, a multiple

number of 2π phase value is added or subtracted until a less than π phase difference is found for the point from its neighboring points.

A different method may be used for a 2D phase unwrapping calculation. **Robinson (1993)** has reviewed several phase unwrapping methods, and discussed their advantages and disadvantages. The simplest phase unwrapping technique is considered to be the linear scanning method. Sequential linear scanning method requires a raster scan unwrapping process through the data, line by line. **Takeda (1982)** introduced an improved version of this linear scanning technique. The new technique unwraps the phase function along individual row independently. The phase discontinuities between rows are removed by scanning through the central column of the data one more time. The improved linear scanning method is very efficient in correcting phase wrapping errors in a 2D phase map. It is used for the phase unwrapping calculation in the above example. Figure 4.4 and Figure 4.5 provide a comparison of the phase function before and after the unwrapping procedure.

4.4 FRINGE ANALYSIS METHOD USED IN THE ON-LINE TOOL MISALIGNMENT DETECTION SYSTEM

The new metrology technique developed for tool misalignment detection measures surface slope errors from the calculated phase discontinuities in the reflected image of a bar target. Depending on the base radius of the test surface, reflected image of the bar

target will have an apparent spatial carrier frequency that can vary due to the changes in the magnification. The variation in fringe carrier frequencies in the reflected images produces difficulties to the synchronous detection method. On the other hand, Fourier transform method is less sensitive to this variability. For this reason, the Fourier transform method was chosen as the image analysis algorithm in the on-line tool misalignment detection system. Sequential linear scanning method is used for the phase unwrapping calculation. Detailed descriptions on this are provided in Section 5.4.

CHAPTER 5

DESCRIPTION OF THE NEW METROLOGY SYSTEM

This chapter describes in detail the concepts behind the new metrology technique for the on-line tool misalignment detection. Basic optical imaging theories are reviewed. A conceptual layout of the system is described. The Fourier transform method for fringe analysis is used for the image distortion calculation in the detection system. The measured image distortion is used to determine the slope change at the vertex of the test surface. The improved linear scanning phase unwrapping technique is used for correction of the phase wrapping error. At the end of this chapter, a computer simulated ray-trace analysis of this detection system and the results are provided.

5.1 THEORETICAL BACKGROUND

In geometrical optics, object to image relationship can be obtained through real ray traces. Geometrical optical properties of the image are obtained from the ray incident positions in the image plane from the object. Reflected images produced by a mirror surface can be obtained by tracing rays reflected off the mirror.

Law of reflection [see e.g. Hecht 1987] described the incident and reflected ray relationship (Figure 5.1). It states that:

1. The incident and reflected rays lie in the same plane of incidence, where plane of incidence is defined by the surface normal and the ray of incident;
2. Incident and reflected rays are symmetric about the surface normal:

$$\theta_i = -\theta_r \quad (5.1)$$

where:

θ_i = angle between the incident ray to the normal of the interface;

θ_r = angle between the reflected ray to the normal of the interface.

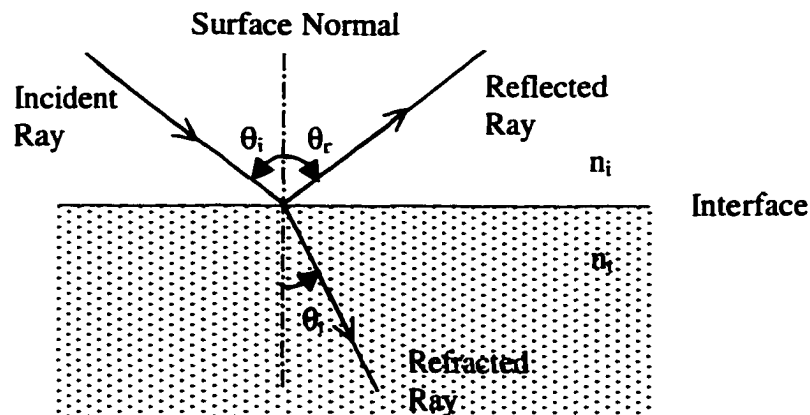


Figure 5.1. Law of reflection.

5.1.1 Image distortions

In reflection, direction of the reflected ray is determined by the angle between the incident ray and the local normal direction of the reflecting surface. Parallel rays are

reflected collimated off surface when the surface normal is constant over the area of incidence. In other words, rays incident on a flat surface from the same direction will be reflected into a same direction independent upon the ray incident positions on the surface. Accordingly, images produced by a flat mirror will be an exact duplicate of the original object with no distortion, as demonstrated in Figure 5.2.

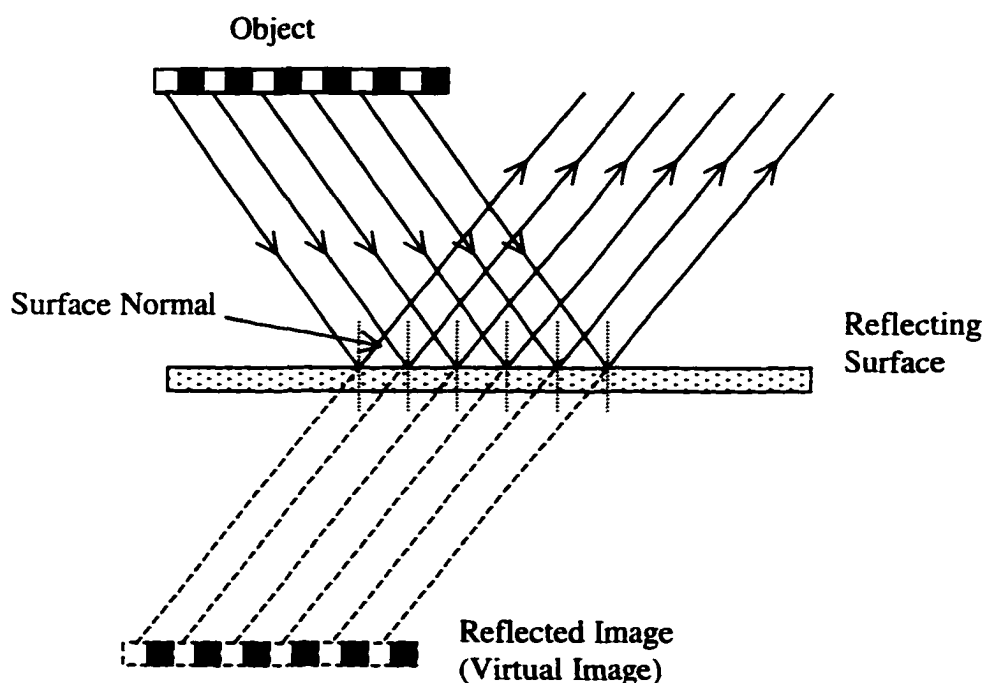


Figure 5.2. A flat surface produces reflected images with no distortion.

When a curved surface is used to produce mirror images of an object, however, the reflection of the object will be distorted due to the variations in surface slopes across the reflecting surface. Just as though using a funny mirror, evenly spaced points on the object are imaged into unevenly spaced points in the image (see Figure 5.3).

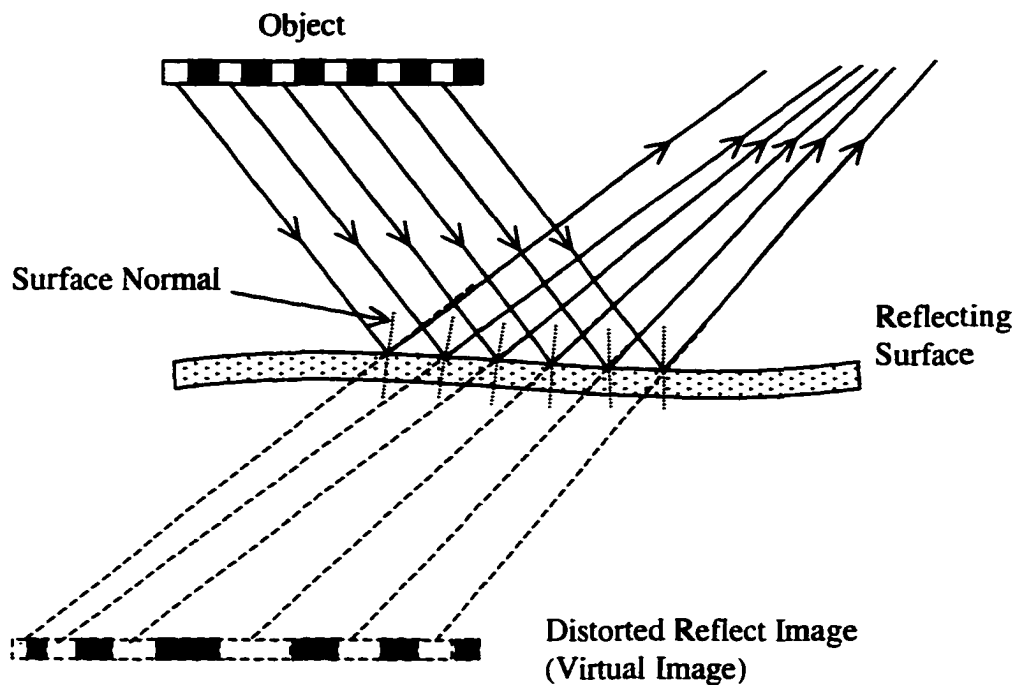


Figure 5.3. Distorted image produced by a curved surface.

Reflected images contain information on the slope function of the reflecting surface. A non-distorted image indicates a uniform and flat reflecting surface. On the other hand, a distorted image implies slope irregularities on the surface. The amount of distortions in the reflected image provides information on the magnitude of the slope changes. Distortions in the reflected image are also functions of the distance between the object and the reflecting surface.

Since the reflecting surface in Figure 5.3 has no base curvature, there is no optical power associated with the surface. Consequently the virtual image produced by this

surface has unit magnification, and the image and the object are symmetric about the reflecting surface. On the other hand, a reflecting surface with base curvature may result in reflected images that are not symmetric about the surface and have non-unit magnifications. The location and the magnification of the reflected image changes as the base curvature of the surface varies. Deviations of the surface from the base sphere result in distortions in the reflected images. Both the reflected image and the image distortion are simply scaled spatially by the magnification of the setup.

5.1.2 Reflected image produced by Opticam generated surfaces with y-errors

As described in Section 2.1.2, Opticam generated surfaces has a non-spherical shape when the ring cutter consists a y-direction alignment error with respect to the vertex of the part during the generation process. To a first order approximation, the surface error has a cone shape with a slope discontinuity at the vertex. When this type of surface is used to produce reflecting images, slope discontinuities at the vertex will result in distortions in the center of the images.

Using geometrical ray traces, the image formation process of a cone structured reflecting surface is demonstrated in Figure 5.4. This cone surface may be considered as a highly exaggerated representation of an Opticam generated surface with y-error. For simplicity, only a one dimensional ray trace is completed along a radial profile of the

reflecting surface in the drawing, and the base radius of the surface is ignored. The location of the reflected image is determined by the object to surface distance and the base curvature of the reflection surface. In this diagram, the surface is flat on either side, and the virtual image formed is located at the symmetric position with the object on the opposite side of the reflecting surface.

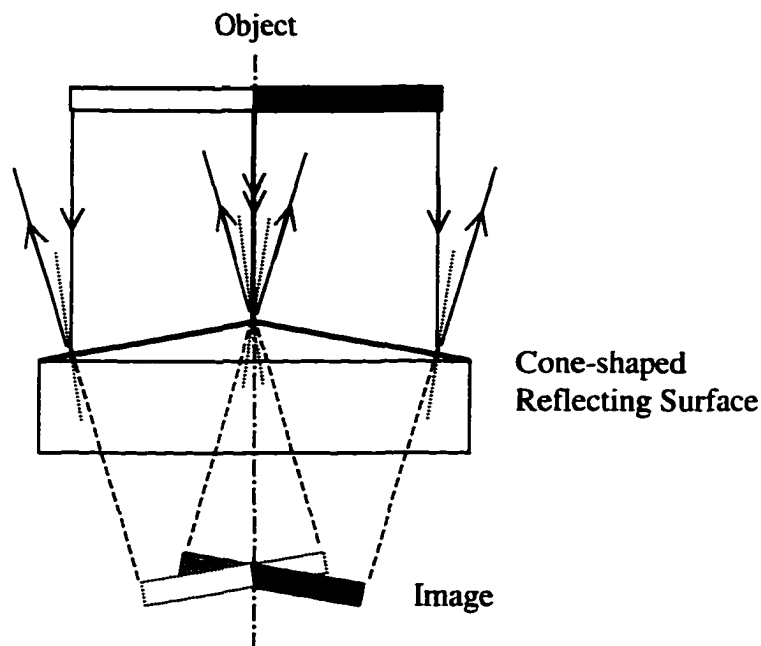


Figure 5.4. Reflected image formed by a cone-shaped surface.

The reflected image has been separated into two pieces. The two parts of the image are produced by either side of the discontinued reflecting surface. The reflected image is distorted, but in particular a discontinuity in the bar pattern will be seen in the center at where the two sides come together. The amount of distortion, or discontinuity, in the reflected image is a function of the relative tilt angle between the two sides of the

reflecting surface and the distance between the surface and the object. Surfaces generated with different amount of y-error have different amounts of slope discontinuity at the vertex; reflected images produced by these surfaces will have different amount of image distortions. These two quantities are linearly related (Section 5.4).

5.2 TOOL MISALIGNMENT DETECTION USING AN IMAGING METHOD

Surface slope discontinuities can be retrieved from the amount of image discontinuities in the produced reflected images. Based on this, a new metrology technique is developed. It is capable of measuring surface slope errors from the reflected images it formed. The detected slope errors can then be used to determine the amount of y-direction tool misalignments using their linear relationship.

A conceptual layout of the new metrology system is shown in Figure 5.5. In this setup, a sinusoidal bar patterned target is located on the right of the system. A CCD camera is placed above the test surface. A beam splitter in the setup folds the optical path and provides a coaxial alignment between the target and the CCD camera. A system aperture stop for the imaging system is located near the objective lens. The front surface of the test part acts like a mirror and produces a reflected image of the bar target. This intermediate image of the bar target is captured by the CCD camera. Video output of the camera is digitized and analyzed to determine slope discontinuities on the test surface.

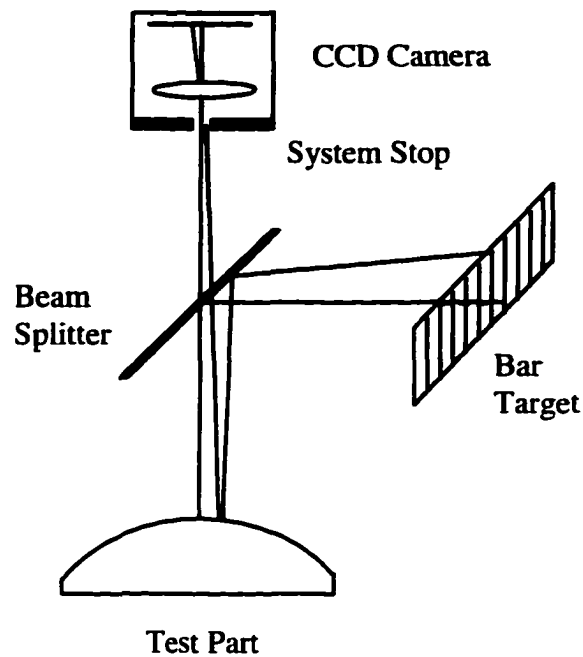


Figure 5.5. Tool misalignment detection system layout.

The captured images will be distorted when the test surface contains slope discontinuities from y-direction tool misalignments. Calculation of image distortions in the reflected images may be used to determine the amount of slope discontinuity on the test surface and eventually the amount of tool misalignment in the y-direction.

This new metrology technique is similar to the moiré deflectometry method, as it is also based on geometrical ray trace. However, the moiré deflectometry requires a spatially coherent illumination source. Since the new technique is based on imaging, no special illumination source will be required. This improvement allows an even simpler system setup for the new metrology system compared to a moiré deflectometer.

In order to detect tool misalignment in the grinding setup, only the slope change on both sides of the test surface near the vertex must be determined. There is no need for a high, or even moderate, spatial resolution of the surface height or slope information for this application. This is a common requirement for moiré and fringe projection and moiré deflectometry. In fact, some degree of averaging on the surface slope function in the system will reduce the noise level in the captured image and improve the detection sensitivity.

In the detection system setup, the amount of averaging of the surface slope function is determined by the size of the aperture stop in the imaging unit, as shown in Figure 5.6. Increasing the aperture size allows more reflected rays to be collected and contribute to the captured image, consequently the surface slope information over a larger area on the test surface will be averaged. Although, the averaging of the surface slope function helps in reducing the noise level in the detection, the slope discontinuity at the vertex of the test surface is averaged at the same time. The averaging may therefore overwhelm the information on the slope change at the vertex. Increasing of the aperture size also reduces the depth of focus of the imaging unit. In order to maintain a wide range of focusing ability to accommodate the image location change due to the change in the radius of curvature of the test surface, system aperture size must be adjusted accordingly. Moreover, aberrations in the system will be increased when the aperture is enlarged.

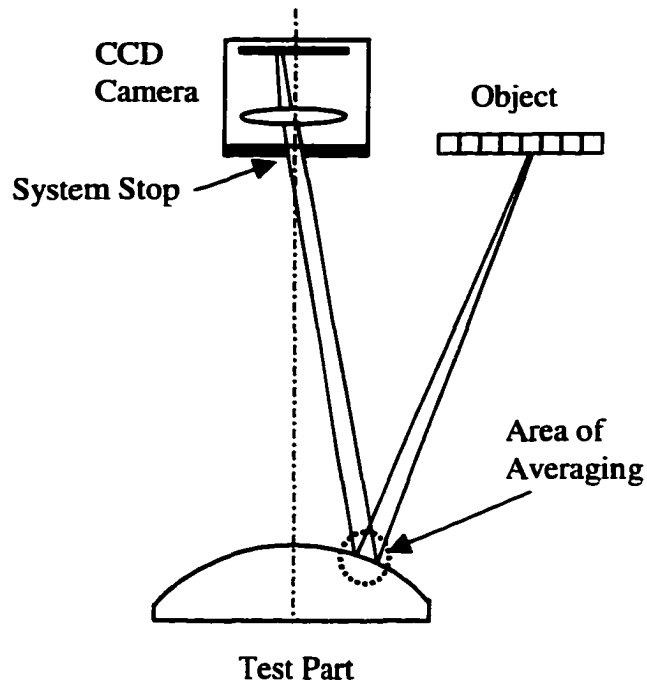


Figure 5.6. Surface slope averaging due to finite aperture size.

The new metrology technique uses a non-contact detection method. It directly measures the surface slope function from the distortions in the reflected images formed by the test surface. Due to its imaging nature, the system can be applied on surfaces a large range of radius of curvature, from concave to convex.

5.3 IMAGE PROCESSING ALGORITHM

Distortions in the reflected images must be evaluated in order to determine the surface slope discontinuity. Mathematically, distortions in an image can be quantitatively

calculated as phase variations from point to point in the reflected image of a periodic bar target. Calculating the phase-function of an image of a periodic target is equivalent to the fringe analysis process used in interferometry. The Fourier transform method described in Section 4.2 is then used image analysis in the on-line tool misalignment detection system. Using this method, only one frame is needed to obtain a 2D phase map of the reflected image.

In order to calculate the phase function ($\phi(x,y)$), the linear phase term ($2\pi\xi x$) in the image must be removed. The Fourier transform technique does this by translating the filtered spectrum to the origin in frequency space (Section 4.3). The translation is limited to frequencies that are represented by the sampled values, which is related to the physical dimension of the original signal and the FFT array size. Several techniques may be used to determine the correct carrier frequency (ξ) value [Bone et. al. 1986]. In our analysis program, the fringe carrier frequency is determined as the frequency component that has the largest value other than the DC. Small residual linear phase error in the calculation did not seem to have a significant effect on the phase calculation in our application. Constant tilt in the calculated phase function, resulting from the residual error in determining the carrier frequency, may be corrected by removing the linear tilt term in the phase map of the image after the Fourier analysis.

The determinations of the shape and the bandwidth of the spatial filter are always difficult problems [**Robinson and Reid 1993; Takeda and Mutoh 1983**]. They directly affect the noise level and the detection sensitivity of the system. Techniques may be used to determine the optimal shape and bandwidth of the spatial filter are proposed by **Bone et. al. (1986)**. In our image analysis program, a rectangular function is used as the spatial filter. The half bandwidth of this filter is determined as a half distance from the DC to the determined carrier frequency in spatial frequency domain. These selections are used and they seemed to provide good detection results as our experiments show. Depending on the noise level in the captured images and the fringe carrier frequency, more optimized filter and bandwidth may be considered. Both the filter shape and the bandwidth may be changed easily in our image analysis program (Section 6.5).

A Fast Fourier Transform (FFT) routine is used to provide Fourier transform calculations in our program. The program will automatically scale the input image to a 512 by 256 pixels data array. Larger array may be used to achieve higher sampling of the image and higher accuracy, although computation time will be increased dramatically. Image array size is set to be values of 2 to the Nth power to reduce FFT calculation time [see e.g. **Hayes 1992**]. In order to avoid alias, image array is padded before FFT calculations. To further reduce processing time, 1D FFT calculation is used for each individual row of the 2D image in our analysis routine. Phase unwrapping, however, is proceeded in a 2D fashion using the improved linear scanning unwrapping method (Section 4.3).

The discontinuity in the calculated phase function is determined by line fitting either side of the phase function and obtaining the separation between the two lines. Before this calculation, residual tilt in the phase map is corrected by removing the linear term from the 2D phase function along the x-direction.

5.4 COMPUTER SIMULATIONS

A real ray trace program was written in C language to simulate the detection process. The description of a real part produced with nominal amount of y-error (Equation 2.16) is put in the ray trace program and used to generate reflected images of a bar target. Figure 5.7 shows the system layout used for the ray trace simulation. The beam splitter in the conceptual setup is removed for the simulation for simplicity.

In the program, rays are traced backward from a group of equally spaced points on the CCD array through the center of the aperture stop. These rays are reflected off the test surface with directions calculated using the Law of Reflection. Reflected rays continue propagate until they intersect the object plane. Intensity values on the object at the location where the ray intersect is recorded and used to form a image pattern on the CCD array.

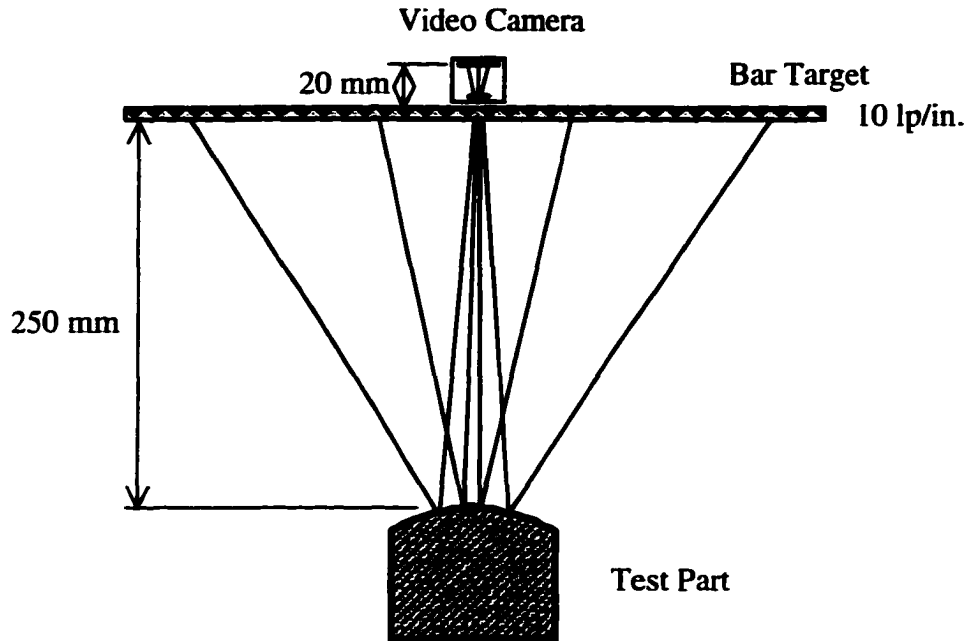


Figure 5.7. System setup used in the ray trace analysis.

Two sets of convex surfaces with radii of curvature of 40 mm and 80 mm respectively were used for the ray trace simulation. The distance between the bar target and test surface was set to be 250 mm. A 10 lp/in. grating pattern was used, and the CCD array was located 20 mm behind the target. Finite aperture size was ignored in the ray trace analysis; no averaging effects were included.

Because of the rotational symmetry of the Opticam generated surfaces, the ray trace analysis was further simplified by tracing rays in one dimension along a radial direction on the test surface. Two-dimensional images for presentation had been generated by duplicating the 1-D ray trace results in the vertical direction for better visualization.

Hence, all horizontal lines in the 2-D image have the same amount of distortion. An actual image of a bar target formed by a real part will show varying distortion in the vertical direction as well as in the horizontal direction (see Figure 5.10).

Figure 5.8 shows a computer-generated image of a sinusoidal bar target formed by a surface with 80 mm base radius and 20 μm of y-direction tool alignment errors. A phase calculation of the image through the vertex of the part is shown in Figure 5.9. A phase step is clearly shown in the middle of the phase profile plot. Again, the magnitude of this phase step is determined from the separation between the two fitted lines on either side of the calculated phase function. The ripples in the phase plot are caused by the loss of high frequency components during the Fourier transform process. In real detection process, noise in the image that has similar frequencies to the bar pattern frequency will also contribute to the noise in the phase plot.

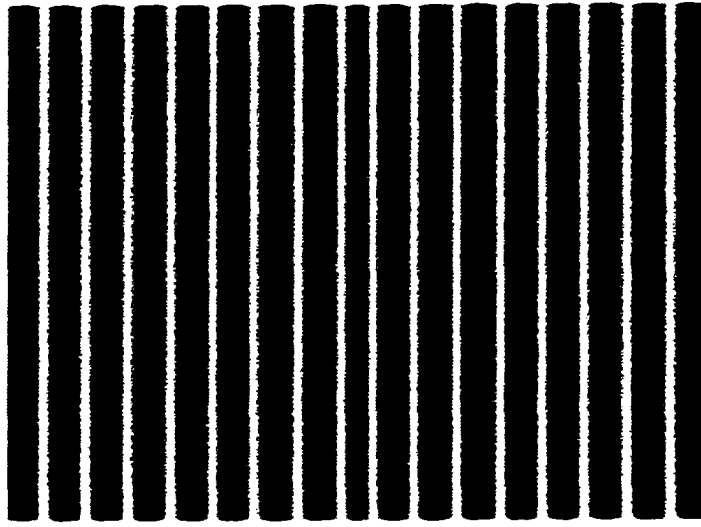


Figure 5.8. Computer generated image of a bar target reflected off a surface with 100 μm y-error.

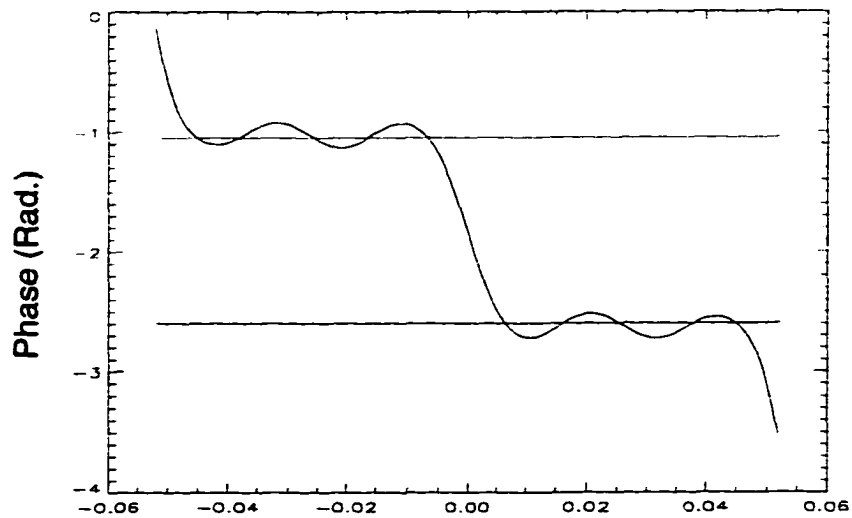


Figure 5.9. Calculated phase profile of the image in Figure 5.8.

For comparison, Figure 5.10 and 5.11 shows a real detection image of a bar target off an Opticam generated surface with 100 μm y-error and the calculated phase profiles of

the image. The test surface has a 120 mm base radius and the captured image covers a 2 cm area on the test part. The fringe distortions in the captured image appear to be less obvious than in the computer simulate image. This variation is caused by the averaging effect in the experimental system discussed in Section 5.2.



Figure 5.10. Captured reflected image of a bar target off a surface with 100 μm y-error.

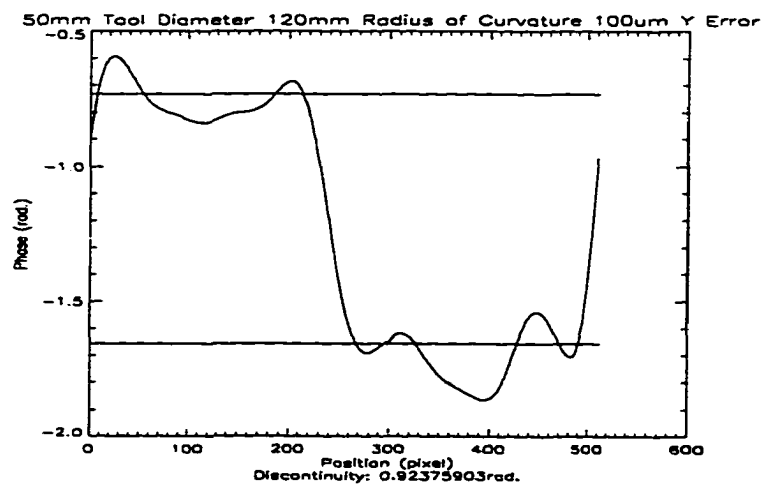


Figure 5.11. Calculated phase profile of the image in Figure 5.10.

Tool misalignment errors are calculated from the measured phase discontinuities in the reflected images. The linear coefficient between the phase discontinuity and y-error is determined through calibration using one data point in the chart, 80 mm radius surface with 100 μm y-error is used in this case.

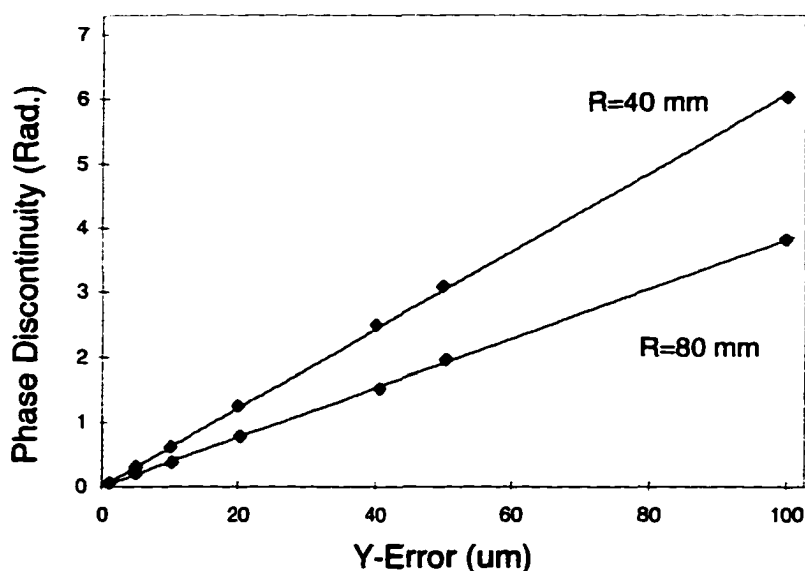


Figure 5.12. Phase discontinuity vs. y-error.

Ray trace analysis also helped us in determining the minimum target size required for this system. The size of the target certainly depends on the field of view of the system, the working distance, the base curvature of the test part and the focal length of the objective lens used. Surfaces with smaller radii of curvature require bigger targets. It is found that, a target 200 mm in width is sufficient for measuring surfaces with radii of

curvature down to 40 mm. This is assuming a 2 cm field on the test surface at 250 mm working distance and 40 mm focal length objective.

Results of the computer simulation prove that the validity of this detection concept. Using this simulation procedure, we also verified the linear relationship between the measured phase discontinuity in the reflected image and the amount of y-direction tool misalignment for a fixed system geometry and a fixed surface radius of curvature (Figure 5.12). It also shows that sensitivity to y-error is reduced as the base radius of the finished surface increases. The ray trace analysis also shows that the field of view of the detection system is very small, where less than 2 cm diameter area near the vertex of the test surface is used. Sensitivity of the detection system is studied using this simulation routine. The magnitude of the phase discontinuity in the reflected image is a function of spatial frequency of the bar target and the working distance of the setup. We found that detection sensitivity increases linearly with an increase of bar target frequency or an increase of working distance, assuming the focal length of the imaging lens is varied to keep the same apparent bar target frequency.

CHAPTER 6

PROTOTYPE SYSTEM DESIGN

Design of the on-line metrology system requires considerations of the machine clearance in the existing Opticam SX machine. An off-axis system layout used in the prototype system is introduced in this chapter. Its advantages and disadvantages over the original on-axis setup are provided. A modular design of the prototype hardware unit gives the system maximum flexibility in alignment, maintenance and possible upgrade. The structure and the function of individual module are presented in detail.

An image analysis software package is developed to incorporate with the hardware unit. It is a menu-driven window based program. It has a familiar graphical-user-interface (GUI), and requires minimum training to operate. A screen shot of the program is provided in this chapter.

In order for the on-line detection system to measure surfaces independent on the actual surface finish, a surface wetting technique is proposed. This technique allows the on-line detection system to take advantage of the wet grinding environment in the Opticam system, and measure surfaces from ground to polished.

6.1 NEW OFF-AXIS GEOMETRY

In order to reduce the overall dimensions of the hardware package, an off-axis detection layout is utilized in the prototype design. In the new layout, both the camera unit and the bar target are located above the test surface. Both units are shifted off the center of the test surface. The camera is tilted from the vertical direction in this setup.

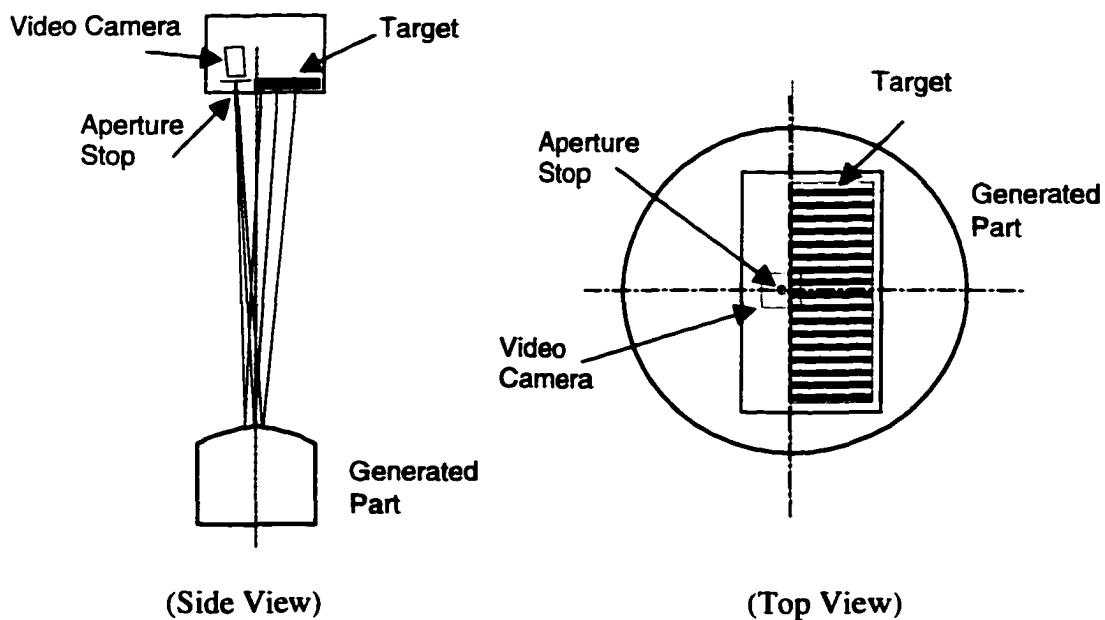


Figure 6.1. Off-axis layout of the detection system.

This new arrangement brings the camera and the bar target together. It allows the two units to be setup into a single package. Overall system dimension is greatly reduced as a result of this. At the same time, by eliminating the beam splitter from the original on-axis design, light efficiency in the new setup is greatly improved. Without the beam splitter,

the field of view and the working distance of the detection unit are no longer limited. A longer working distance can now be accommodated by adjusting the tilt angle and the position of the camera to point at the vertex of the test surface. Flexibility in the working distance allows the system to be easily adapted into the existing machine environment. Furthermore, an increase in the working distance magnifies the amount of distortion in the reflected images, therefore providing the ability to improve the sensitivity of the tool misalignment detection.

The shortcoming of the new off-axis geometry resides in the induced aberrations from the tilt of the imaging system [Shack 1992(a), 1992(b)]. For the purpose of this application, residual distortion in the imaging system is of our primary concern. It has a direct impact on the system detection sensitivity. The original on-axis setup allows the co-axial alignment among the imaging unit, the test surface and the bar target. Aberrations in this system are well controlled. Residual distortions in the imaging system are insignificant, especially because of the relatively small field of view of the system; a less than 2 cm diameter area centered about the vertex of the test surface is used for the detection. In the off-axis system, the tilt of the imaging system with respect to the optical axis defined by the test surface induces aberrations in the system on axis. The induced aberrations, especially distortion in the imaging system, can no longer be ignored.

To overcome this problem, a calibration procedure to determine the amount of residual distortion in the imaging is necessary. This calibration process is completed by

conducting a regular measurement on a perfect spherical surface. In this case, calculated distortion in the reflected image may only come from the system setup and the aberrations in the imaging unit. This calibration result is saved and used to compensate the calculated raw phase values during the tool misalignment detection process. This calibration procedure not only allows the correction of system aberrations, it is also used to eliminate errors result from the distortions in the printed bar target pattern.

Although aberrations in the imaging system vary with the changes in the working distance, the change is found to be minimal. System calibration result from one working distance setup may be used for a large range of setup conditions.

6.2 HARDWARE DESIGN

Hardware design of the prototype system includes four basic units: imaging, illumination, bar patterned target and electronic control. All four units are setup into one single package. Thin aluminum plates are used to enclose the entire system; it prevents the system components from the coolant agents used in the Opticam generating system. Figure 6.2 shows a picture of the prototype system. The system hardware unit has a $10\frac{3}{4}$ "(w) x $10\frac{3}{4}$ " (l) footprint with $13\frac{3}{4}$ " height. The base plate of the detection system has an 8" (w) x 6" (l) rectangular opening for the trans-illuminate bar target.

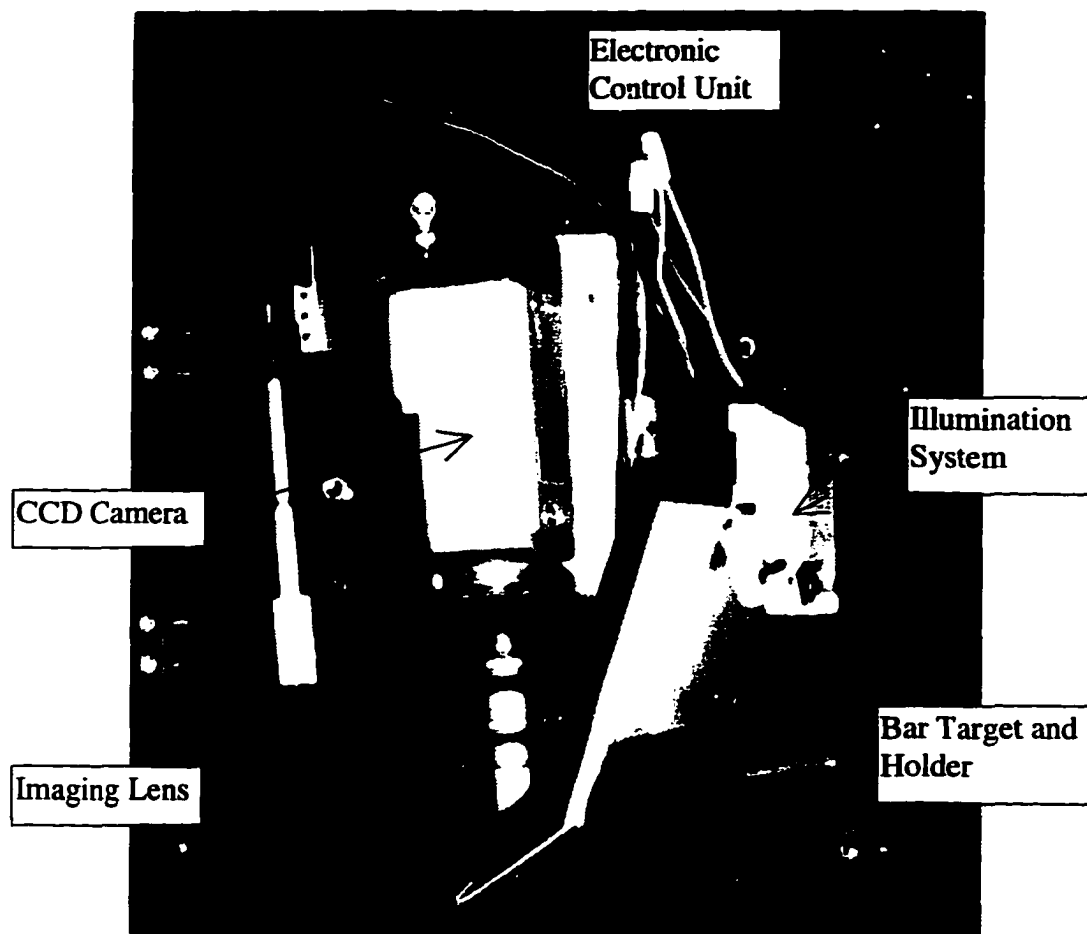


Figure 6.2. Hardware unit of the prototype tool misalignment detection system.

The hardware system utilizes a modular design, where the imaging, the illumination and the electronic systems are separated units. Each unit can be removed and adjusted without affecting the neighboring systems. An air exhausting fan located on top of the system provides sufficient air flow in the box to protect the imaging lens and the CCD camera from the heat dissipated by the light source. The overall system is compact, and many provisions have been made for easy alignment of the unit when mounted in the Opticam generator.

6.2.1 Imaging System

The imaging system, which includes a CCD camera and an objective lens, is designed to have a high flexibility in focusing and alignment. The black and white CCD camera (Hitachi Model KP-110) has 570(H) x 485(V) pixels resolution. It has a composite video output, and it is interfaced with a frame grabber for image capturing. The whole imaging system (see Figure 6.3) is placed on an adjustable tilt stage, while the CCD camera is mounted on a translation stage for focus adjustment. The entire imaging unit can also be laterally shifted in the plane of the tilt to accommodate different working distances.

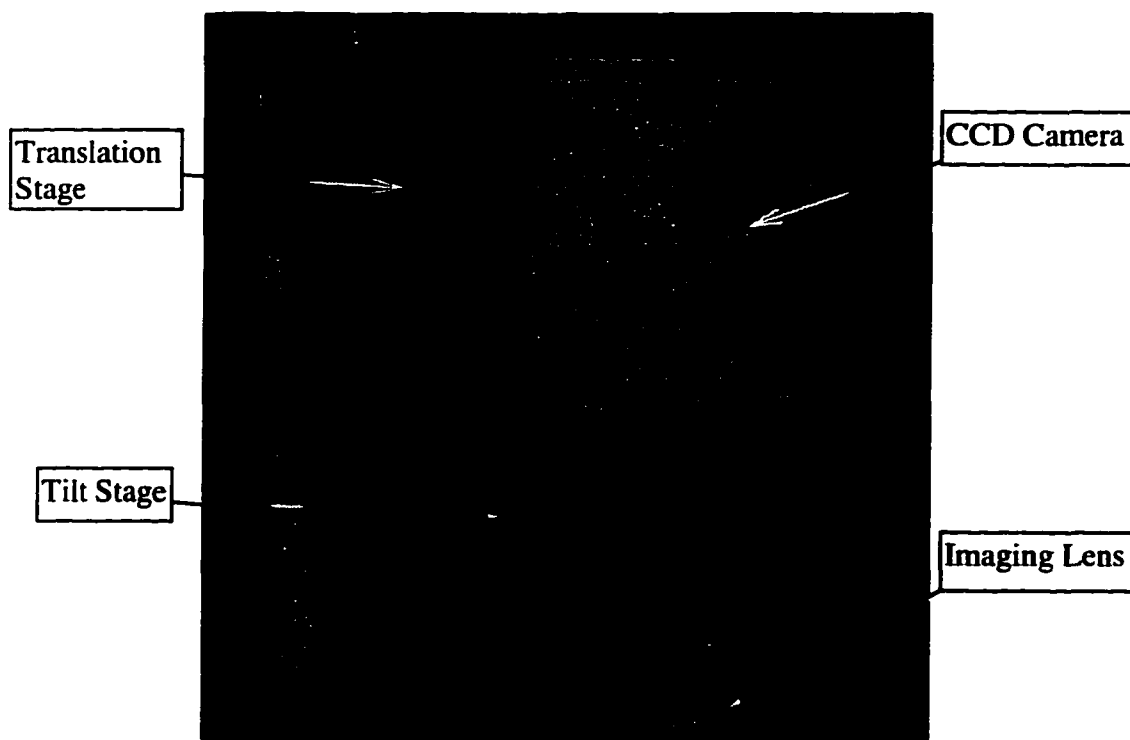


Figure 6.3. The imaging lens and the CCD camera on the tilt stage.

The translation of the CCD camera gives the system a large range of focusing ability. Location of the reflected image shifts as the radius of curvature of the test surface changes. Calculation of the position of the image captured by the CCD camera shows that an approximate 35 mm total travel of the CCD array will be sufficient for complementing a -200 mm to $+200$ mm radius of curvature change on the test surface (Figure 6.4). This calculation is based on assumptions of a 250 mm working distance, an objective lens with 50 mm effective focal length (EFL) and a 280 mm lens to test surface distance. The calculated image distance is measured from the objective lens. In the prototype unit, the translation stage has a total travel of about 60 mm.

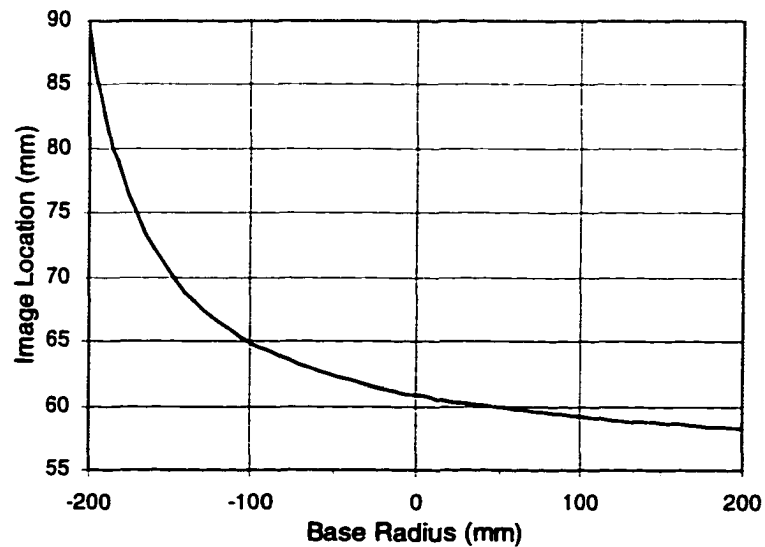


Figure 6.4. Image location shift as a function of the surface base radius.

The objective lens used in the prototype design is an off-the-shelf camera lens. It is mounted on a C-mount base and it can be detached. Different image magnifications and imaging conjugates can be achieved by changing this lens.

The objective lens has an adjustable effective focal length, from 50 mm to 75 mm. However, the focal length setting is not critical because of the focusing ability provided by the translation motion of the CCD array. During our experiments, the lens is adjusted to have a 50 mm effective focal length. The lens unit also has an adjustable aperture stop. It may be used to accommodate for different lighting conditions. Depending on the system setup, e.g., the working distance, the base curvature and the surface roughness of the test surface, the camera aperture can be adjusted to maintain a best contrast in the reflected images. Closing down the system aperture reduces the speed of the image system and improves the depth of focus of the system. However, this adjustment reduces the image contrast and increases the noise levels in the captured image. System $F/\#$'s on the order of $F/10$ have been found to be a reasonable compromise for system performance.

6.2.2 Illumination System

The illumination system (Figure 6.5) uses a 300W, 120VAC quartz-halogen projector bulb in order to provide sufficient light output. A bright target helps to increase signal-

to-noise ratio in the captured images, consequently the resolution of the tool misalignment detection may be improved while keeping a slow f-number to maintain the depth of focus of the system. The light bulb is mounted on a holder with a spring-loaded mechanism for easy assembly and exchange. A fold mirror in the illumination unit is used to fold the light path and reduce the physical dimension of the unit. This fold mirror can also be rotated to control the light output direction.

Heat management is often a problem for halogen bulbs. This is specially a problem for our system, where the illumination unit is placed very close to the bar target and the CCD camera in order to reduce the physical size of the entire system. In order to control heat dissipated by the light bulb and provide sufficient airflow in the system, an internal fan is placed over the illumination unit on the top cover of the system. A mechanical plate is also placed between the illumination unit and the CCD camera unit to reduce heat. Heat absorbing glass used in the unit helps to protect the illuminated bar target from the heat.

Uniform illumination of the target must be considered during the design process. In order to achieve uniformity in the target illumination by using a condensed light source at a close distance, an opal glass diffuser is placed after the heat absorbing glass (see Figure 6.6) to diffuse the light. Small amount of intensity non-uniformity in the captured image still exists, and it is removed by the image processing software before the phase calculation process (see Section 6.3).

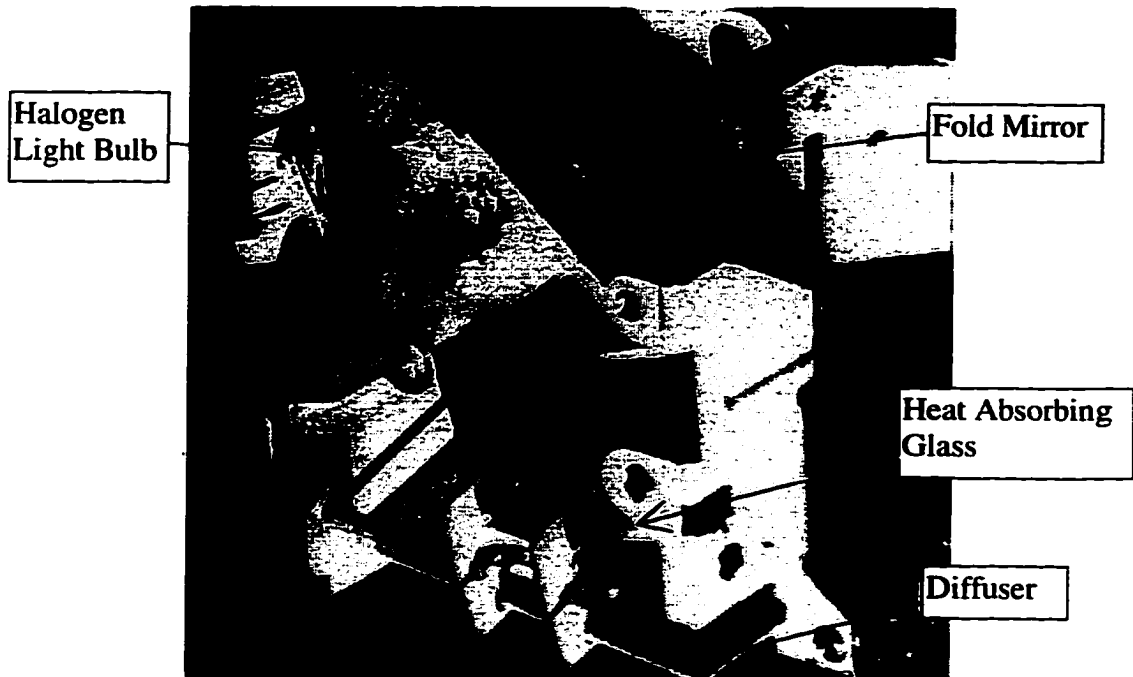


Figure 6.5. Picture of the illumination unit.

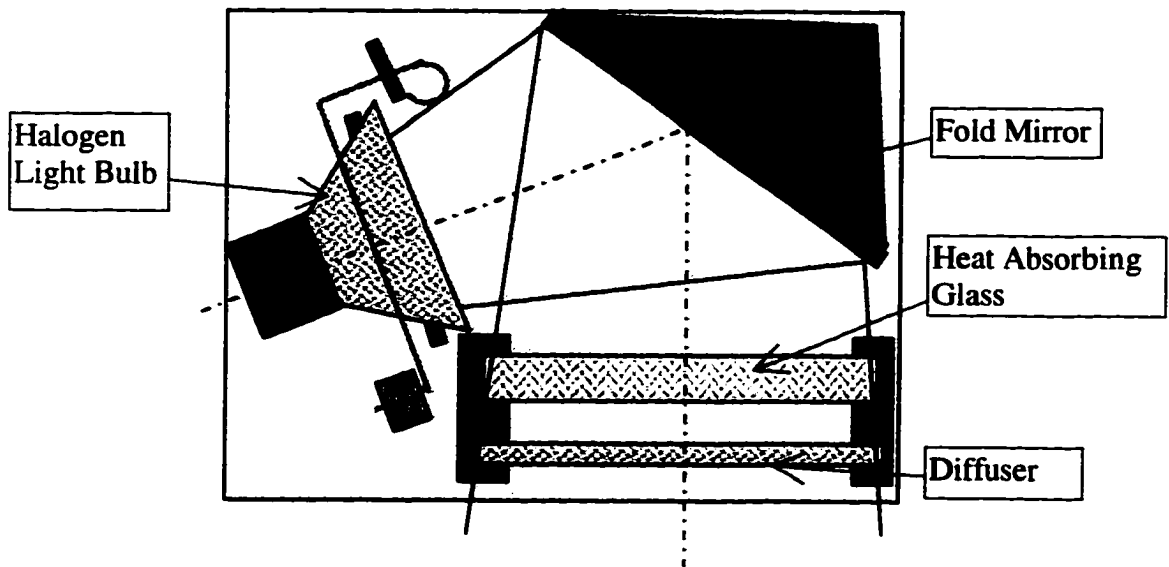


Figure 6.6. Schematic drawing of the illumination unit.

6.2.3 Bar Target and Target Holder

A sinusoidal grating pattern is generated using a computer program and printed on a transparent plastic sheet using a 600 dpi laser printer. Distortion in the grating pattern produced during the printing process is small, and it can be compensated by the system calibration.

The generated transparent bar target is laminated on the front side of a plastic plate. The plastic plate keeps the target from warp despite the heat from the halogen bulb. Front side mounting of the target eliminates “ghost” images formed by a potential total internal reflection from the other surface of the plastic plate. The target plate is placed in a rigid aluminum frame in the prototype design. This target holder can easily slide in and out of the detection unit for target change, without removing the detection system from the Opticam generator.

The detection sensitivity of the system increases as the spatial frequency of the bar target increases (Section 5.4). Test surfaces with different radii of curvature produce reflected images with different magnification and fringe period. In order to maintain good resolution of the reflected image and avoid aliasing, a lower frequency target should be used on surfaces with steeper radii. The highest allowable bar target frequency is determined by the working distance of the detection setup, the base curvature of the test

part and the CCD array pixel spacing. In the prototype system, a 10 lp/in sinusoidal fringe pattern was used. The procedure used to determine the maximum spatial frequency allowed of the bar target is shown as following.

The CCD sensor array (see Section 6.2.1) has an approximately 12 μm pixel size. Assuming a 6 pixels per fringe period sampling rate, the maximum allowed fringe frequency on the CCD array is calculated to be approximately 13.8 lp/mm. For a detection setup with 250 mm working distance, 280 mm camera to surface distance, 50 mm EFL for the objective and 100 mm base radius test surface, the image magnification of the entire setup is about 0.03. The required target frequency is then determined by multiple the magnification value with the fringe frequency on the CCD, which is 0.41 lp/mm or approximately 10 lp/in.

6.2.4 Electronic Controls and Frame Grabber

A remote electronic control box is built to operate the heat fan, the light bulb and the CCD camera using low voltage electronic relay circuits. Individual module units in the system may be switched on and off independently. The camera system may be turned on for visible inspection of the test surface and the system alignments. The halogen light bulb may be switched on only during the detection process to further control the heat in the detection unit.

A Matrox Meteor PCI bus based frame grabber made by Matrox, Inc. is used to interface with the CCD camera for image capturing. The frame grabber supports NTSC/PAL/SECAM, RS-170/CCIR and standard RGB input. The NTSC interface is used in the prototype system to communicate with the CCD camera. Under the NTSC format, the frame grabber supports a 640(W) x 480(H) image format. Although standard color video is allowed for this frame grabber, only one color channel is used, and black and white images are used for the fringe analysis. The high-speed PCI bus interface allows the frame grabber to capture images at 30 fps live video rate. This feature is used to provide live videos of the Opticam generator setup on the computer screen during the detection and the alignment procedures. The frame grabber is controlled by a desktop PC designated for the on-line detection system through the image analysis program introduced next.

6.3 SOFTWARE DESIGN

A software package is designed to be fully integrated with the hardware unit of the prototype system. The program codes are provided in Appendix. It calculates the phase discontinuities in the captured images and determines the amount of tool misalignments in the grinding setup. The program starts by initializing the frame grabber and brings up a scalable live video window for visual inspection of the test surface.

During the detection process, the operator inputs the nominal radius of curvature of the test surface and instructs the frame grabber to capture the reflected image off the test surface. The captured image will be displayed in the left side child-window in the main program (see Figure 6.7). The operators have the option of selecting different region of interest in the captured image for analysis. The selected region is then preprocessed to remove low frequency intensity non-uniformity and high frequency noise. Finally, this preprocessed image is analyzed using the Fourier transfer method, and phase discontinuities in the image will be calculated. The detected y-error is automatically displayed in the input/output window. Profile plots of the calculated 2-D phase function of the analyzed image may also be displayed on the screen for visual verification. Constant tilt in the calculated phase function is automatically corrected before the phase discontinuity calculation. Manual adjustment of the tilt in the phase function is allowed using keyboard interface. Linear fitting of the phase function on either side along the center row of the phase map is used to determine the amount of phase discontinuity in the image. A flow chart (Figure 6.8) shows the major steps in this image analysis program. A typical detection and analysis cycle for the program takes less than 10 sec on a PC equipped with a Pentium processor.

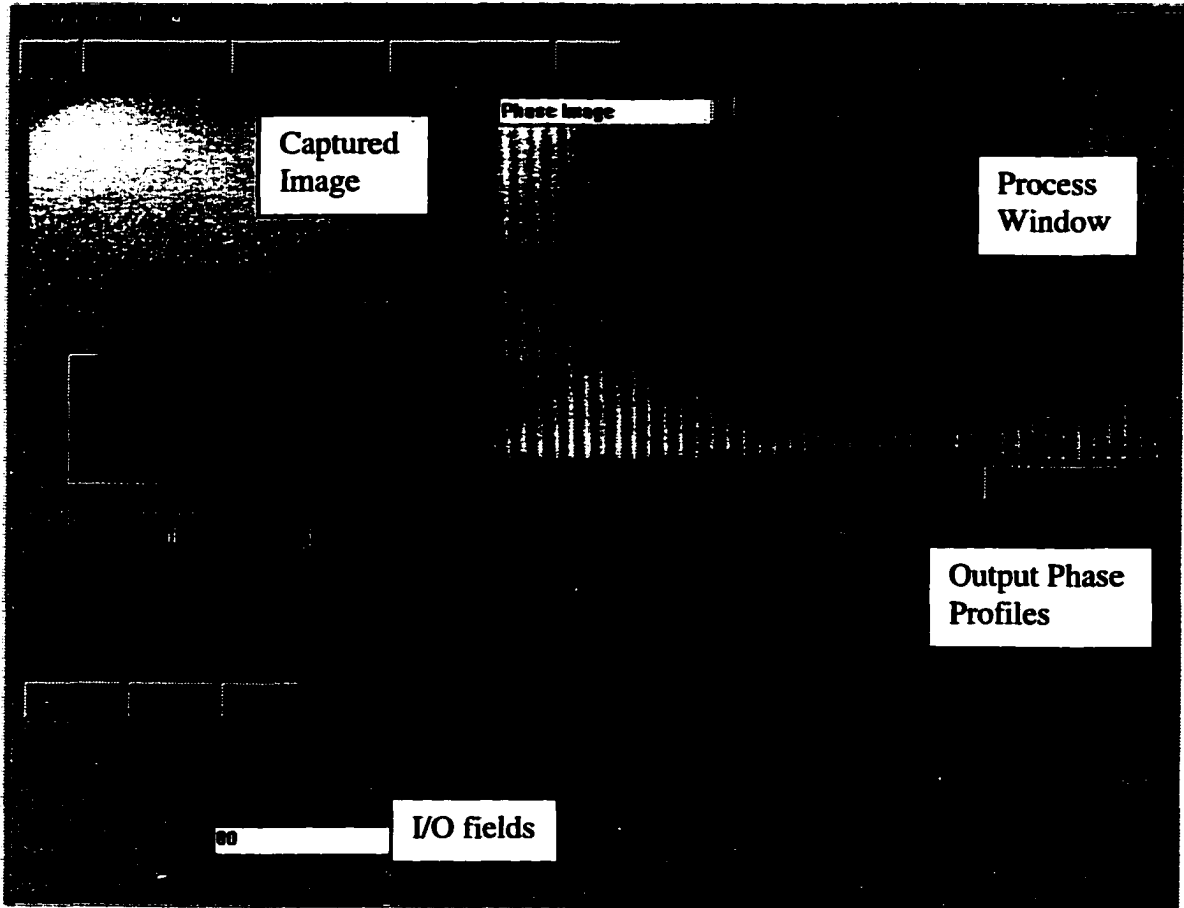


Figure 6.7. Screen capture of the image analysis program.

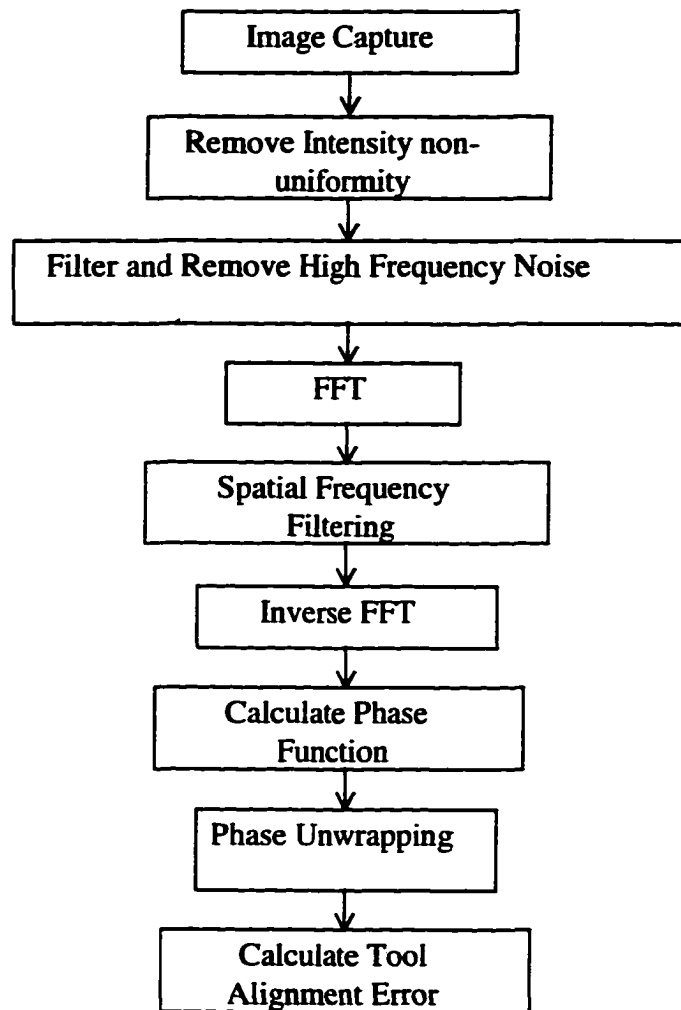


Figure 6.8. Flow chart of the image analysis program.

The program is written to have a user-friendly interface. It has the familiar windows graphical interface. A screen shot of the program is shown in Figure 6.7. The entire program is menu driven and little or no training is necessary for operating the program. The usual Windows features are included in the program.

When the hardware setup is changed by using a different working distance or a bar target with different spatial frequency, the program can be re-calibrated for the linear coefficient between the phase discontinuity and the y-error. This process is completed by measuring a part with a known radius of curvature and a known amount of y-error. A simple change in the conversion factor in the software is calculated by this procedure.

6.4 SURFACE WETTING TECHNIQUE

Surfaces produced by the Opticam generator have finishes that vary from ground to almost polished. In order for the detection system to obtain good images of the bar target, a specular reflection is required. To achieve this condition for all the surfaces, a surface wetting technique is proposed and used for the tool misalignment detection procedure.

The generated surface is sprayed with cutting coolant in the Opticam generator while it is spun at approximately 200 rpm. Centripetal force spreads the coolant agent on the surface uniformly to form a thin layer that conforms to the actual part shape. This layer of liquid acts like a reflectance coating on the test surface. It provides good reflectance for the test part independent of the state of finish of the surface. This situation mimics the conditions inside the Opticam machining center, and in fact, takes advantage of the wet environment to allow any part to be measured.

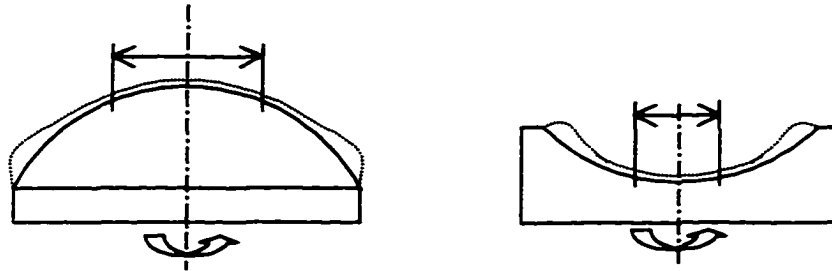


Figure 6.9. Schematic drawing of the surface wetting process.
(Indicated regions are the areas the liquid layer conforms to the surface)

The part spindle speed and the viscosity of the wetting agent are the two most important factors that affect the conformance between the liquid agent and the test surface. A high spindle speed will result in a high centripetal force, which helps in repelling the liquid off from the surface center and producing a thin layer of coating on the test surface. In addition, wetting agents with lower viscosity have the tendency of spreading the liquid more uniformly across the test surface than higher viscosity agents.

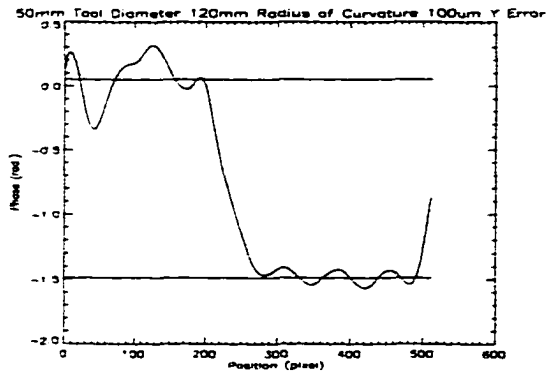
In the Opticam SX, the part spindle is mounted in a vertical direction. Due to the gravitational force, the surface wetting agent have the tendency of falling into the center of the concave surface, which makes surface wetting more difficult on concave surfaces. Nevertheless, experimental results show that a good conformance between the coolant and the part may be obtained within a 2 cm diameter area at the center of the concave surface, with 200 rpm and radius greater than 50 mm. This provides a sufficient surface area for tool misalignment detection.

A comparison of reflected images of a ground test surface taken before and after the surface wetting process is shown in Figure 6.10. The image modulation can not be seen without surface wetting.



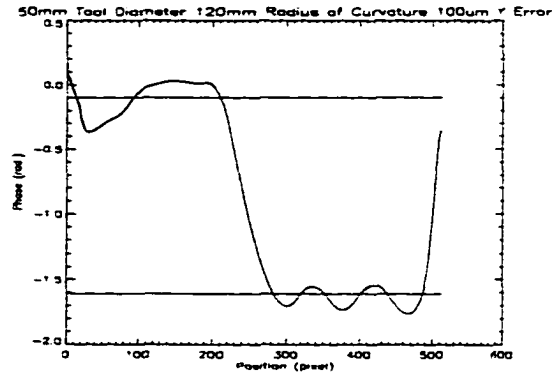
Figure 6.10. Comparison of image contrast for dry and wet surfaces.

Sample parts have been tested using this surface wetting method. Results prove that the thin liquid layer does not significantly change the basic surface feature. The measured phase discontinuities in the reflected images of a surface with and without wetting are shown in Figure 6.11. The measured phase discontinuities in this example show a 0.04 radians difference. This variation in the phase values corresponds to a less than 1 μm uncertainty in the detected y-error. However, the amount of error in the detected tool misalignment result from the surface wetting varies with the radius of curvature and the surface finish of the test part. Less error is encountered for surfaces with lower surface roughness. This error also depends on the viscosity of the wetting agent and the part spindle speed.



Phase Discontinuity : 1.54 rad.

(Dry Surface)



Phase Discontinuity : 1.50 rad.

(Wet Surface)

Figure 6.11. Calculated phase discontinuities of the reflected images off a test surface before and after surface wetting.

CHAPTER 7

EXPERIMENTAL RESULTS

The prototype tool misalignment detection system has been tested on-line in the Opticam SX generator at the Center for Optics Manufacturing, at the University of Rochester. The experimental results presented in this chapter were obtained during the time period from February 24th to March 1st, 1997. Sample surfaces with different radii of curvature and different amount of y-errors were generated. The combined effects of the tool misalignments and the machine dwell on the overall surface figure errors was investigated. Detection sensitivity of the prototype unit was determined.

At the end of the cutter infeed process in the Opticam system, the ring cutter is not immediately withdrew from the generated surface, rather it is kept grinding on the part at a fixed z-position for a few seconds. This process, which is called machine spark out, is generally used to improve final surface finish and remove surface roughness. Sub-surface damage on the generated surface, however, is not affected by the machine spark out.

It was suspected that the machine spark out and the machine dwell both contribute to the central dip on the Opticam generated surface when tool alignment errors are

corrected. In order to study the machine dwell errors on surfaces with different radii of curvature, machine spark out time and tool spindle speed during the grinding process were varied. We have also examined the noises present in the captured reflected image produced due to the surface wetting agent. Surfaces finished with fine grinding tool were generated and tested without applying surface wetting agent. Detection sensitivities on both the specular and the ground surfaces were studied and their differences were discussed.

7.1 DETECTION SETUP

In the Opticam SX spherical surface generator, both the part and the tool spindles are mounted in the vertical direction. During the grinding process, the tool spindle is tilted respect to the vertical z-axis by a calculated angle. The modified SX system (OptiPro) allows the new tool head to be tilted to a maximum 90 degree angle in the x-z plane. This modification enables the machine to generate non-spherical surfaces by contouring. This change however restricts the real-estate at the right-hand side of the tool spindle for add-on equipment. The Opticam SX generator also has limited y-direction motion for the tool spindle head. The part spindle is on a translation stage with motion confined only in the x-direction. The full travel of the tool spindle is about 100 mm along the y-axis. These restrictions produce many constrains on the design of the mounting mechanism of the on-line detection prototype system.

Because of the limitation on the y-direction motion, the prototype unit has to be mounted in the x-z plane with the tool spindle. During our experiments, the detection unit is mounted adjacent to the cutter head on a removable frame (see Figure 7.1). Due to the tilt of the tool head, the detection unit can not be permanently mounted in the machine; it must be removed during the grinding process. Maximum allowed working distance for the detection setup is also limited to about 250 mm, because of the presence of the tool exchanger. Figure 7.1 shows a picture of the prototype detection system mounted inside the Opticam SX. To make a measurement, the part is translated from the generating station under the cutter spindle to a measurement position under the detection unit.

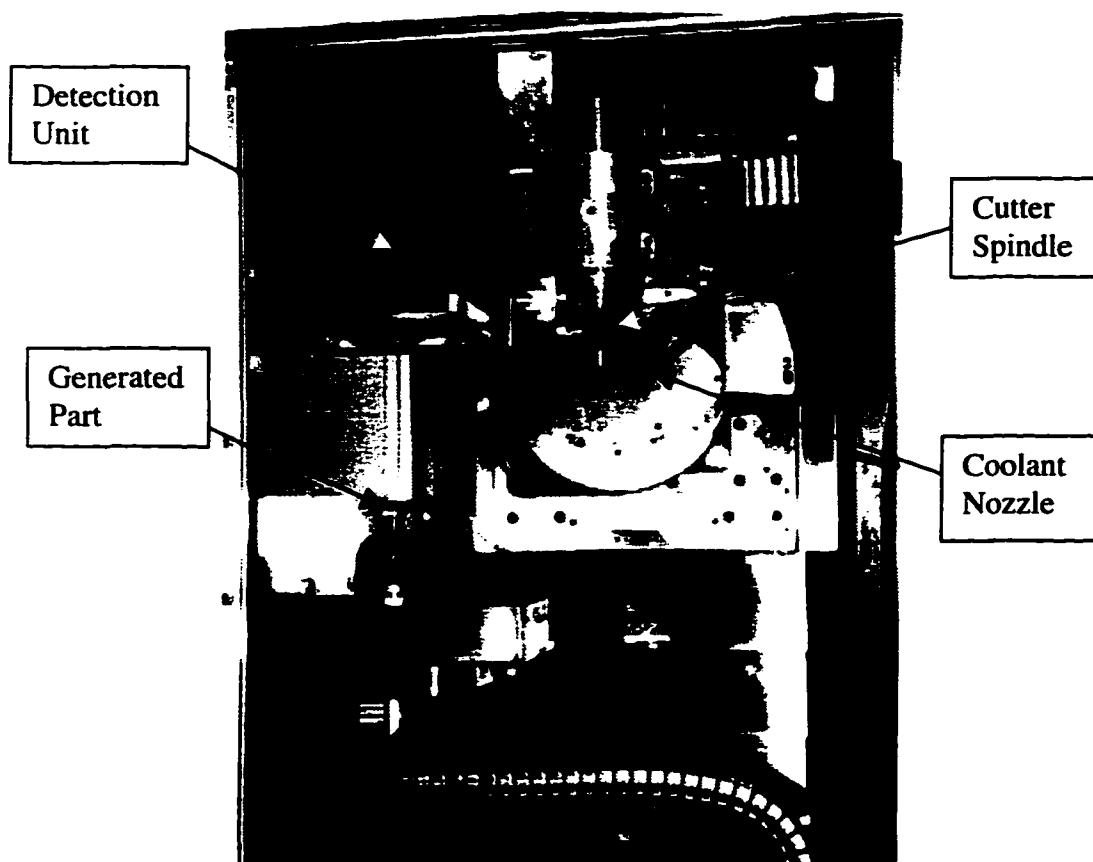


Figure 7.1. Tool misalignment detection system inside the Opticam SX generator.
(generated part is under the detection unit)

A medium cutting tool with 10 to 20 μm grid size was used for the surface generation. The ring cutter inner and outer diameters were approximately 48 mm and 52 mm respectively. Grinding conditions for all the sample surfaces were controlled and kept the same to avoid bias in the collected data. The part spindle speed was 250 rpm and the tool spindle speed was 10,000 rpm. The tool in-feed rate was 40 μm per minute on all generated parts. Material removal was 75 μm for each generated part.

Three sets of convex surfaces were generated during our final study with 50 mm, 80 mm and 100 mm base radius respectively. Nominal y-errors were introduced on these samples with 2 μm increments from 0 μm to 12 μm ; y-errors larger than 15 μm were examined in 5 μm increments up to 50 μm on all samples.

7.2 SURFACE FIGURE ERRORS FROM CUTTER MISALIGNMENTS AND MACHINE DWELL

Y-direction tool misalignments in the Opticam produce surface figure errors on the final parts that correspond to a high spot at the vertex. On the other hand, machine dwell produces a surface shape error in the opposite direction; a slight hole is ground into the vertex. Figure 7.2 shows a 3-D error map of a surface with machine dwell error, while Figure 7.3 shows the type of surface figure error produced by y-direction tool misalignments. Opticam generated surfaces have an overall surface figure error that is the combined result from both the tool misalignment and the machine dwell. Surface

figure errors produced by the y-direction tool misalignments increase in approximately a linear fashion with the amount of misalignment. The machine dwell errors, however, do not vary with a fixed, 15 second, spark out time on parts with the same base radius (see Section 7.5).

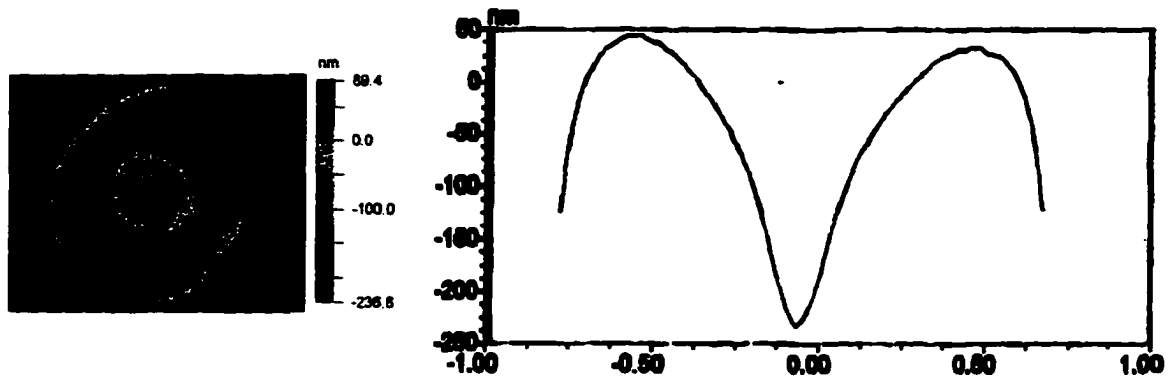


Figure 7.2. Surface error map of a part with machine dwell error.

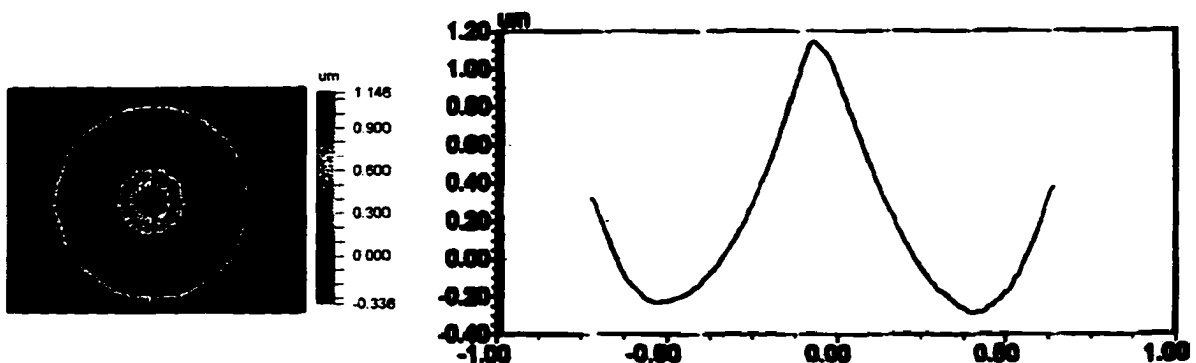


Figure 7.3. Surface error map of a part generated with y-error.

For the study of surface figure errors containing both the machine dwell and the tool misalignments, we produced a series of surfaces with the same radius of curvature but with different amounts of y-error. By holding the spark out time constant during the

grinding process on these samples, machine dwell errors on all the samples were kept constant. Resulting samples were measured using a mechanical surface profiler along a radial line, and the surface peak-to-valley errors against their best-fit spheres were determined. The measured peak-to-valley errors are plotted versus the introduced y-errors as shown in Figure 7.4. As expected, the overall surface figure errors increase linearly with the amount of y-error when the alignment error is relatively large, greater than 10 μm . The surface PV error has a minimum at a point where the tool misalignment error is balanced by the machine dwell error. The surface figure error goes up for smaller amounts of y-error. In this region, the dwell error dominates the surface figure error and overwhelms any error due to tool misalignments.

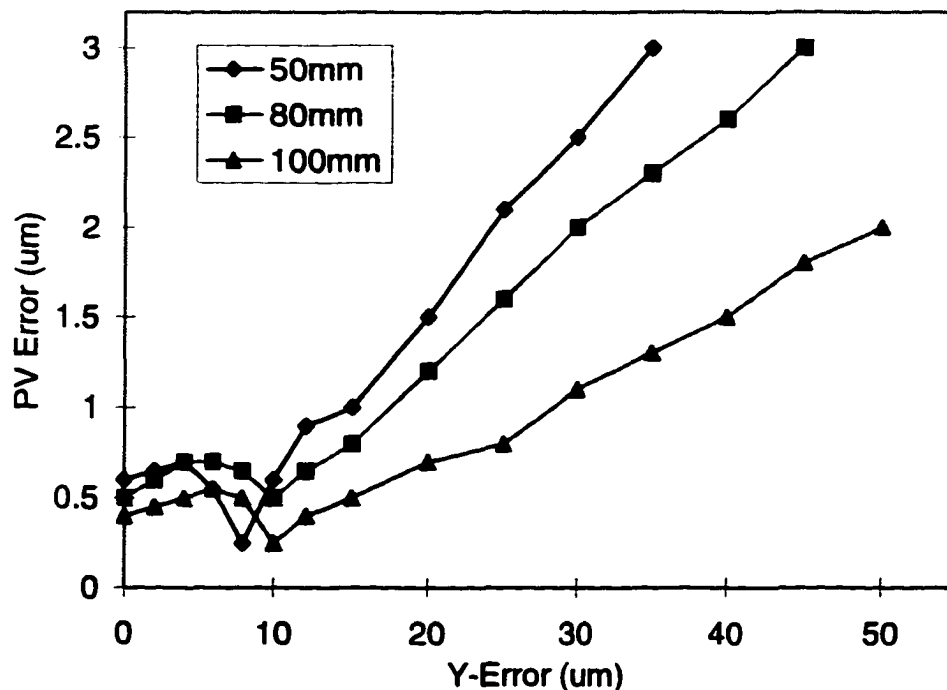


Figure 7.4. Surface PV error vs. y-error for surfaces with different radius of curvature.

This study has been conducted on surfaces with three different radii of curvature. Despite the differences in sensitivity to the tool misalignments at different base radii, all three sets of data show very similar behavior in the region of small y-error.

Experimental results show that the machine dwell errors are generally small; they are significant only when the tool misalignment errors are minimal. When the tool misalignment errors are eliminated in the grinding setup, generated surfaces will have figure errors associated with the machine dwell. Our results indicate that the best final surface figure is achieved when a small amount of tool misalignment is applied to balance the machine dwell error.

The result of this study suggests that a small amount of tool misalignment in the Opticam machine has a positive effect on the surface generation process. The best overall surface figure is produced when a y-direction tool misalignment of about 10 μm is introduced to balance the dwell error. Also, the surface figure error measurement should be the figure of merit in determining the detection sensitivity of the on-line tool misalignment system rather than using the absolute measured y-error when surface figure is the ultimate goal.

The on-line tool misalignment detection system measures surface slope function from the reflected image off the test surface. It is designed to detect tool misalignment from the slope discontinuity produced by y-error. It can also be used to detect machine dwell errors. Machine dwell error produces surface slope discontinuity at the vertex of the generated surface that is opposite to the one resulting from y-error. Measured phase discontinuity in an image produced by a part with machine dwell error has an opposite sign to the one resulting from y-error (Figure 7.5). The on-line detection system will be unable to detect small tool misalignments when the surface figure error produced by the tool misalignments is balanced by the machine dwell error on the Opticam generated parts.

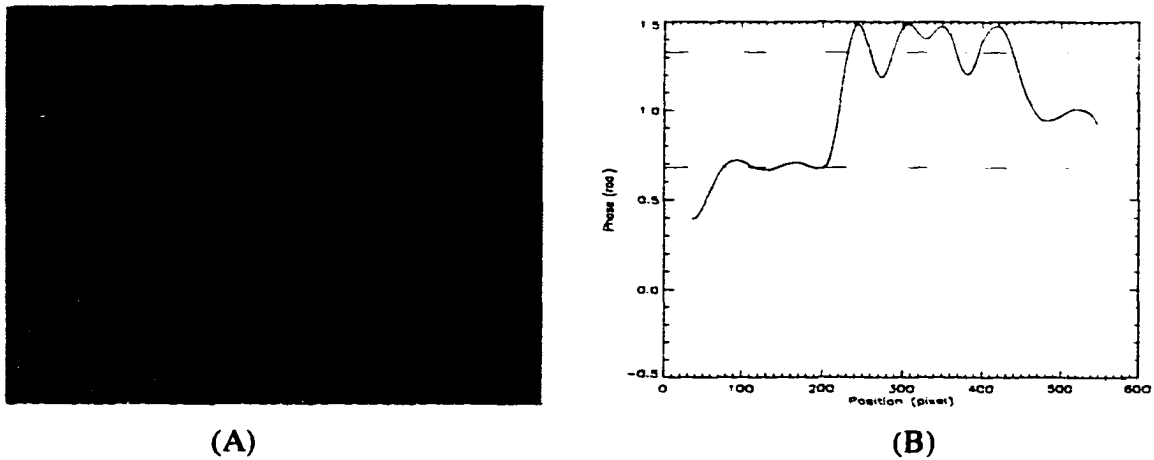


Figure 7.5. Opticam generated part with machine dwell error: (A) Captured image; (B) Calculated phase profile along a horizontal line.

7.3 DETECTION SENSITIVITY

The initial detection setup of the prototype unit requires both the optical alignment and the calibration of the software program. The prototype system was installed with a 250 mm working distance and the imaging unit was adjusted to the appropriate tilt angle. The imaging lens aperture was set to achieve good light efficiency while maintaining sufficient depth of focus.

During the grinding process, the detection system was removed from the SX generator and the tool spindle was tilted. After the surface was generated, the tool spindle was tilted back to the vertical direction and the detection unit was put into the machine. Without removing the finished surface from the part spindle, the part was translated along the x-direction to the test position directly under the detection unit. While the part spun at 250 rpm, surface wetting agent was applied to the test surface. Liquid on the test surface was allowed to settle for a few seconds and conform to the actual surface shape. The detection system was then instructed to capture a reflected image of the sinusoidal bar target off the test part. This captured image was automatically analyzed and the tool misalignment was calculated. To avoid variations in the machine dwell effects, all sample surfaces were generated with a fixed 15 second spark-out time.

Bias or offset in the nominal tool alignment was also examined. For this purpose, sample parts at a fixed radius of curvature (80 mm) with both positive and negative y-errors were generated. Figure 7.6 shows the measured surface peak-to-valley errors using a mechanical surface profiler versus the nominal tool misalignment in both the plus and the minus y-directions. The symmetry in the plot provides evidence that there was no bias in the residual system alignments: at the position defined to be zero, the generator was properly aligned. This plot also shows the expected result that y-errors in either direction result in the same surface errors.

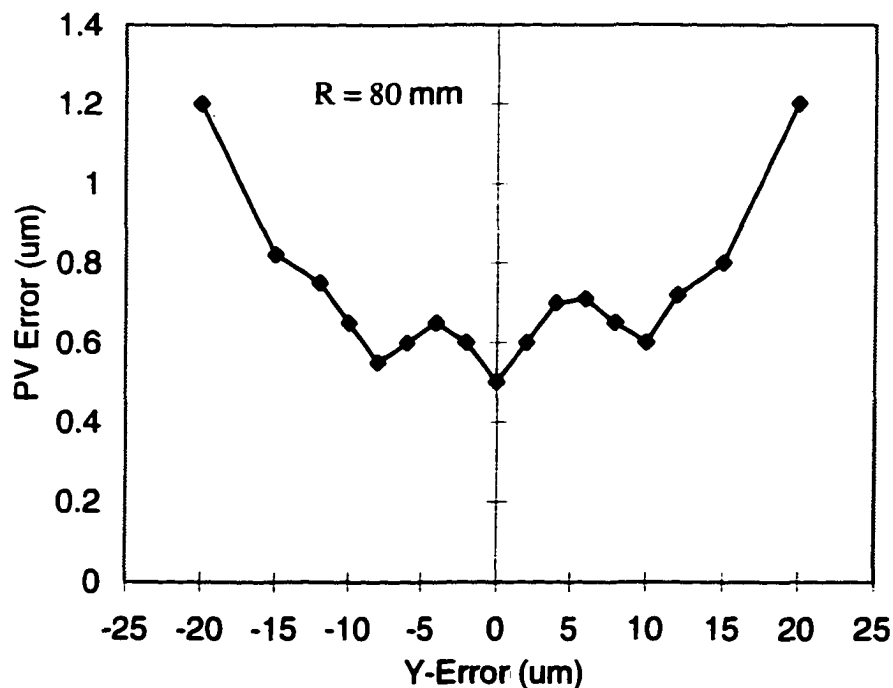


Figure 7.6. Surface PV vs. \pm y-error.

The on-line tool misalignment detection system calculates surface slope errors from the distortions in the reflected image off the test surface. To avoid residual errors from

the detection system, calibration of the system is conducted before the tool misalignment measurements. The calibration used an interferometrically certified surface with an approximately 80 mm radius of curvature and no figure error. The measured data of the perfect part is used as the reference to correct all experimental data in the proceeding experiments. This calibration process corrects residual system distortions, including imperfections of the sinusoidal bar target and aberrations in the image unit of the system.

Three sets of surfaces with three different radii of curvatures were generated to determine the sensitivity of the prototype system. For each set, the introduced y-errors were varied from 0 μm to 50 μm . The actual surface errors for all samples were again determined from their radial surface profile measured using a mechanical surface profiler. The measured y-direction tool misalignment values are plotted against the nominal y-errors in Figure 7.7. A linear regression calculation is conducted to determine the correlation coefficient between these two sets of data. Excellent correlation was found between the calculated or measured y-errors and the nominal values. The R-square value of the linear fit of the data points is 0.943.

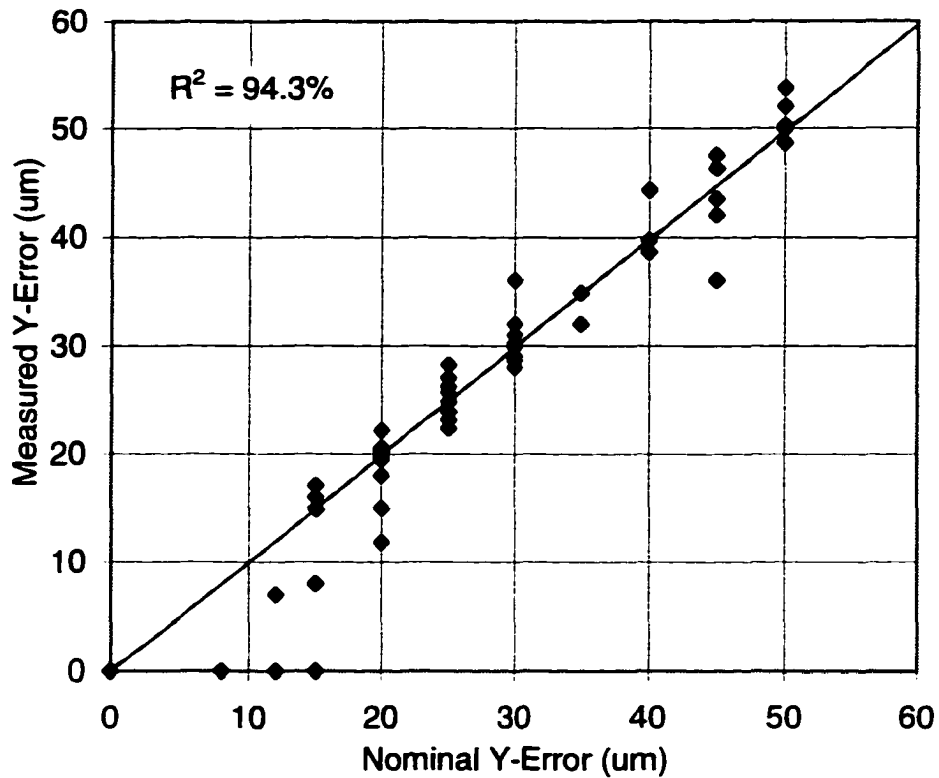


Figure 7.7. Measured y-error vs. nominal misalignment.

Note that the most noticeable deviation of the data points from the line fit of the data setup is in the region of 10 µm tool misalignment. This area in the plot corresponds to the region where the tool misalignments are balanced by machine dwell errors. The on-line detection system was unable to detect y-errors because of this.

As we have discussed earlier, the detection sensitivity of the on-line tool misalignment detection system should be referred to the actual surface figure error rather than the absolute y-direction tool misalignments (see Section 7.2). Figure 7.8 shows the

residual peak-to-valley surface errors of the test samples versus the corresponding measured y-errors. A decreasing sensitivity of the tool alignment errors with increasing base radii of curvature of the generated surfaces can be seen. Flatter surfaces are more tolerant of tool misalignments.

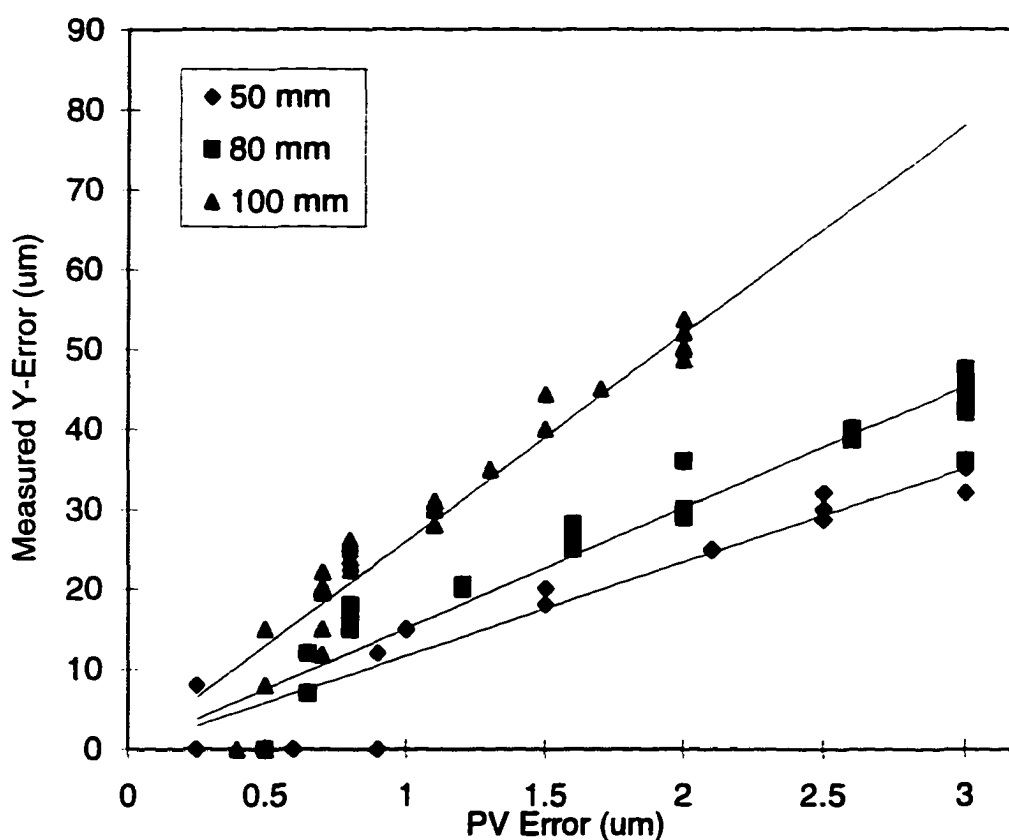


Figure 7.8. Residual surface PV error vs. y-error.

During the experiments, we found that the detection sensitivity depends greatly upon the quality of the captured image. For specular surfaces, the detection sensitivity of our system is better than 0.5 μm peak-to-valley surface error. On ground surfaces, however, surface wetting is required to improve surface specularity during the detection process.

The prototype system was able to detect surface errors that are greater than 1.0 μm peak-to-valley. This reduction in detection sensitivity is due to the higher noise level in the reflected images off ground surfaces with wetting agent. The liquid coatings on these surfaces altered the actual surface shapes to a very small, but noticeable, degree.

The medium tool was used to generate all the test samples. Surfaces generated with a coarse grinding tool were not tested for our studies because coarse tools are mostly used for material removal rather than figure generation. Fine tools generate surfaces have much better surface finish and the tool misalignment detection sensitivity is greatly improved.

7.4 CUTTER MARK ORIENTATION IDENTIFICATION

Because y -errors in both the positive and the negative directions produce the same type and amount of surface errors, the sign of the alignment errors can not be determined from the magnitude of the surface error (Section 2.3). Orientation of the cutter marks on the test surface should be inspected to retrieve this information. Unfortunately, appearance of cutter marks depends on glass material, grinding tool grid size and vibration characteristic of the machine. When overall surface finish is bad, the cutter marks are very difficult to visualize because of the scattering from the roughness of the base surface.

Different illumination arrangements were tested. Oblique angle illuminations were used to enhance the appearance of the cutter marks. In some cases, the cutter marks were still difficult to be identified. Our test results show that cutter marks are usually visible for surfaces generated by rough or medium tools. For a fine-tool ground surface, the cutter marks are usually harder to see.

7.5 MACHINE SPARK OUT TIME AND SURFACE DWELL ERROR

As noted earlier, machine dwell produces surface figure errors on the Opticam generated parts. In order to understand the effect of machine spark-out time on the surface figure, we corrected all the alignment errors in the SX machine and generated sample surfaces with different amounts of spark-out time. Surfaces with different base radii of curvature were also examined. It was found that the machine dwell errors did not vary with the changes in the spark-out time. Figure 7.9 shows the peak-to-valley error on surfaces produced with different amounts of spark out time. The test surfaces used in this experiment have a fixed radius of curvature of 80 mm. The dwell error was found to vary with the base radius of curvature of the generated surface and the tool spindle speed. During regular generation process, the tool spindle speed is about 10,000 rpm. In the dwell error study, the tool spindle speed is reduced to about 5,000 rpm for the low spindle speed study.

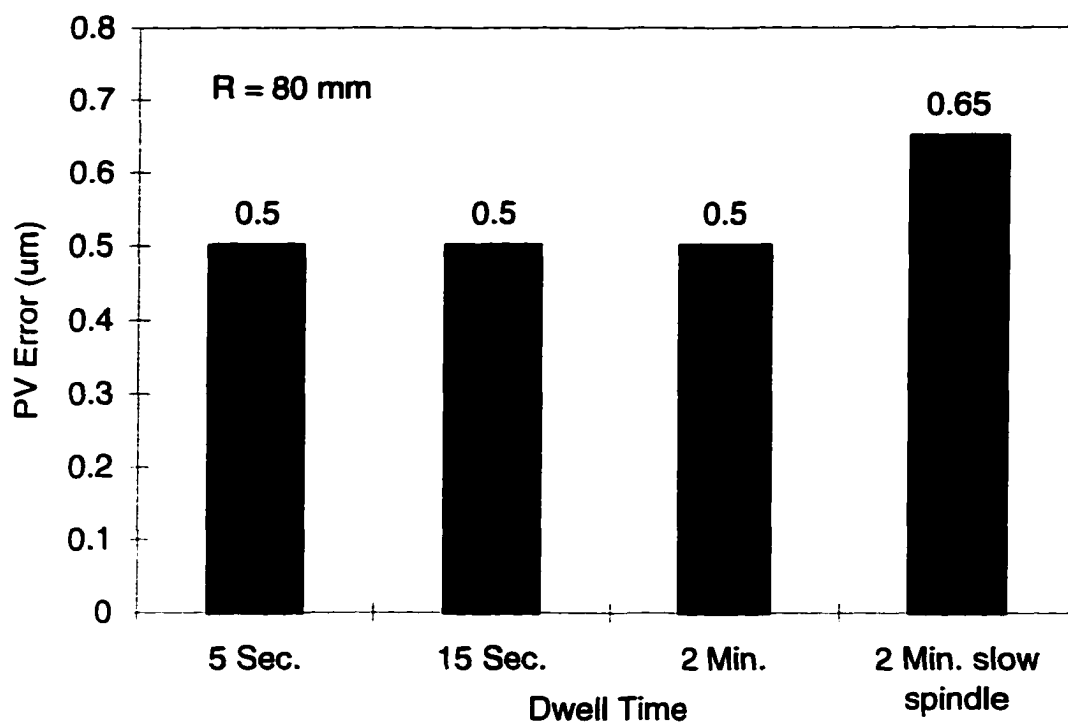


Figure 7.9. Surface PV error vs. machine dwell time.

7.6 STUDY OF SURFACE WETTING AGENT

We used both pure water and highly diluted LOH K-40 coolant as our surface wetting agent for our experiments. In the Opticam SX machine, the LOH K-40 coolant is used at an approximately 15:1 dilution ratio. At this concentration, the coolant agent has a much lower viscosity value, approximately 30 cps, compared to about 72 cps for pure water. The diluted LOH K-40 coolant agent also has a lower surface tension, which in theory makes it a better agent in preserving surface shape and increasing the apparent surface

specularity. However, during our experiments, we found a higher than expected noise level when the LOH K-40 coolant was used.

This observed problem is caused by the small particles mixed in the LOH K-40 coolant agent. In the Opticam machine, the coolant is recycled, and some debris produced during the grinding process is mixed into the coolant in spite of the filtering system in the coolant delivery unit. The existence of the particles in the coolant trapped on the test surface produces noise in the reflected image and reduces the detection sensitivity of our system. Using pure water can eliminate this problem, with higher surface tension as trade-off. Therefore, a clean and highly diluted LOH K-40 coolant, or other agent with the same property, is suggested by the results of this study.

CHAPTER 8

DISCUSSION AND CONCLUSION

The newly developed image based optical metrology system has been shown to be an alternative to the conventional techniques for detecting the changes in surface figure due to misalignment of the ring tool in a spherical surface generator. The result is used to determine the amount of misalignment. It has many advantages over conventional metrology systems in a simple setup, low mechanical stability requirements and no special requirements on the coherent properties of the light source. It is a geometrical ray trace based system. It uses a non-contact method to measure surface slope functions. Because of the imaging nature of this technique, it has essentially no limitation on the working distance and the radii of curvature of the measured surfaces. The detection system requires specular test surfaces, but ground surfaces in the Opticam system may be tested with the use of the surface wetting technique.

On-line test results suggest that the prototype detection system developed is capable of detecting y-direction tool misalignments. The detection sensitivity of the prototype system is found to be the tool misalignment that corresponds to approximately 1 μm PV surface error. Better detection sensitivity was achieved on specular surfaces where

surface wetting is not necessary. Increasing the working distance and the spatial frequency of the bar target can also improve the sensitivity of this metrology system. Due to the difficulties in identifying the cutter mark orientations on some of the finished parts, the direction of the y -error was not able to be reliably determined.

Future full integration of the on-line tool misalignment detection unit in the Opticam generator will help to further optimize the design of the detection system. It will also give the detection system more flexibility in selecting the necessary working distance based on the detection sensitivity requirements. A dedicated mounting structure for the detection unit will permit a true on-line non-interrupted detection procedure. Addition of an automatic image-focusing unit and a motorized stage control function in the prototype system will allow an automated detection procedure. By interfacing the computer output of the detection unit with the CNC control center in the Opticam generator, tool misalignment detection results can be transferred to the Opticam generator directly and automatically without human interaction. A close looped fabrication and testing system is possible. Productivity of the Opticam system will be greatly improved.

In the prototype system, captured images are processed in one dimension. The surface slope function is calculated in the direction that is perpendicular to the fringe orientation. This procedure is justified by the rotational symmetry of the Opticam generated parts. The slope function in different directions on the test surface may be measured by rotating the test surface or change the orientation of the bar target. Simple

modification of the target pattern to a concentric ring pattern may allow a one-step measurement of the 2D slope function of the test surface. In this case, captured images must be processed in a polar coordinate from at the center of the ring pattern.

8.1 X-ERROR DETECTION

The on-line detection system is designed to measure y -direction tool misalignments in the Opticam generator. X -direction tool misalignments also produce errors on the finished parts. The x -errors can be detected by measuring the radius of curvature errors on the finished surface or the present of the nib at the vertex. Spherometers are used in practice for the radius error measurements. Although our current detection system is capable of measuring radius of curvature of the Opticam generated parts, the accuracy of the measurement is limited. Detail discussion of this topic is provided later in this chapter.

Another way of detecting x -errors is through the identification of the nib at the vertex of the Opticam generated surface. Spherometers can be used to identify the nib at the vertex of the finished parts. This technique is very sensitive, although, it does not provide a quantitative measurement on the magnitude of the x -error. Microscopes are used to inspect surfaces with nibs at the vertices. This method allows the operator to measure the size of the central nib and determine the corresponding x -error directly. The

difficulty existed in this method is that the overall surface roughness on the finished surface scatter light which overwhelm the nib image. On most ground surfaces, nibs are not visible unless the x-errors are big.

The live video capability in our detection system allows the on-line part inspection. Different types of illumination geometry were tested to enhance the nib image. Oblique light illumination allows the imaging system to reject specular reflections. Consequently, scattered light by the nib on the test surface is enhanced. Different image magnifications may also be obtained easily by changing the objective lens in the imaging unit (see Section 6.2.1). However, experimental results show that the nibs on ground surfaces can not be seen until the x-error is greater than 100 μm , which is greater than the usual setup tolerance for the Opticam generator.

8.2 SURFACE HEIGHT MAP

The new metrology technique developed directly measures surface slope functions. It is possible to obtain surface height map by integrating the measured slope function. However, this process requires a correction of the non-linear mapping between points in the image and points on the test surface. This complication is produced by the non-telecentric imaging layout used in the prototype system, and it may be solved by upgrading the current system to an object-space telecentric imaging setup [see e.g.

Kingslake 1983]. An object-space telecentric system provides a linear mapping between the image and the test surface (Figure 8.1). The measured phase function of the test surface can be directly related to the actual surface slope function because of this linear correspondence. The potential problem for this setup, however, is the low light throughput for a telecentric imaging system. In order to achieve surface height information, the system f-number must also be adjusted to reduce averaging effect.

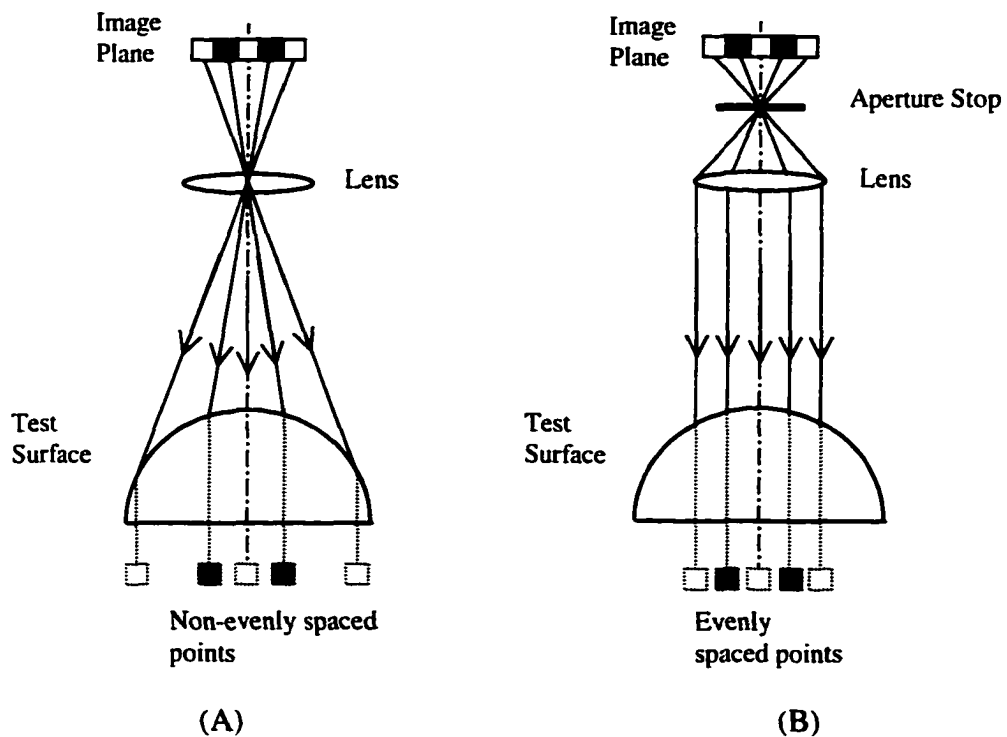


Figure 8.1. Comparison of non-telecentric and telecentric imaging systems:
 (A) Non-telecentric imaging system;
 (B) Object spacing telecentric imaging system.

8.3 RADIUS OF CURVATURE MEASUREMENT

The on-line detection system measures slope function from the reflected image off the test surface. This reflected image also contains information on the base curvature of the test surface primarily through the magnification or position of the observed image. It is desirable that a simple modification of the existing system will allow the measurement of the surface radius. One approach for this radius of curvature measurement, which is almost inherent in the existing design, is by determining the location of the intermediate image reflected off the test surface. With the information on the location of the reflected image, the optical power of the test surface and its base radius can be determined by knowing the target to surface distance. Similarly, the magnification of the image can also be used for surface radius measurement. In the Opticam SX machine, the target to test surface distance can be determined to a high degree of accuracy. Therefore, the accuracy of the radius of curvature measurement depends essentially on the accuracy of the image distance using this method.

The tool misalignment detection system is a cascaded imaging system. The intermediate image formed by the test surface is re-imaged by the CCD camera. In order to precisely locate the reflected image of the bar target, it is important for the CCD camera unit to have a small depth of field. In fact, the CCD camera must have a depth of field that is smaller than the maximum allowed tolerance on the reflected image location

for a given radius measurement accuracy. A mathematical analysis of the achievable accuracy for the radius of curvature measurement using the exiting detection system and setup geometry is provided as following.

Starting from the Gaussian imaging equation, an object to image relationship can be expressed as:

$$\frac{n'}{z'} = \frac{n}{z} + \phi \quad (8.1)$$

where:

n' = index of refraction in the image space;

n = index of refraction in the object space;

z = object distance;

z' = image distance;

ϕ = optical power of the system.

For a reflecting surface in air, the refractive index in the object space is unity. In the image space, the index of refraction is defined to be negative unity. The optical power of the mirror surface is calculated as:

$$\phi = \frac{(n' - n)}{R} = -\frac{2}{R} \quad (8.2)$$

Combine Equation (8.1) and (8.2), and we have:

$$-\frac{1}{z'} = \frac{1}{z} - \frac{2}{R} \quad (8.3)$$

also,
$$z' = \frac{zR}{2z - R} \quad (8.4)$$

Equation (8.4) describes the relationship among the image distance, the object distance and the base radius of the reflecting surface. By differentiating Equation (8.3) on both sides, we get:

$$\frac{1}{z'^2} dz' = \frac{2}{R^2} dR \quad (8.5)$$

$$\left(\frac{dz'}{z'} \right) = \frac{2z'}{R} \left(\frac{dR}{R} \right) \quad (8.6)$$

By substituting z' in Equation (8.6) by Equation (8.4), a simple relationship between the percentage errors in the image distance and the percentage error in the surface radius is obtained:

$$\left(\frac{dz'}{z'} \right) = \left(\frac{2z}{2z - R} \right) \left(\frac{dR}{R} \right) \quad (8.7)$$

With a given requirement in the radius of curvature measurement, the maximum allowed error in determining the location of the reflected image can be calculated using Equation (8.7).

Now, the depth of field of the CCD camera must be determined. The depth of field of an imaging system is defined as the amount of distance that the object allowed to be shifted and still remain within the blur criterion. This is the range of the objects that are appeared to be “in focus”. The depth of field can be calculated using Equation (8.10).

$$L_{near} = \frac{Lf(D + \beta')}{fD - L\beta'}, \quad (8.8)$$

$$L_{far} = \frac{Lf(D - \beta')}{fD + L\beta'}, \quad (8.9)$$

$$\delta = |L_{far} - L_{near}|. \quad (8.10)$$

where:

D = entrance pupil diameter;

f = effective focal length of the lens;

L = nominal object distance;

L_{near} = near field distance;

L_{far} = far field distance;

β' = linear resolution in the image space (blur criterion);

δ = depth of field.

In the current system setup, the resolution of the imaging unit is limited by the CCD array pixel size. This is assuming that the optical aberrations in the system are small and negligible. Therefore, the image blur size in the image space (β') is the pixel size of the CCD array, which is about 12 μm .

Using the derived equations, the current system setup is analyzed for radius of curvature measurement. The entrance pupil diameter (D) is the aperture stop diameter used in the imaging unit. This value can be adjusted. During the tool misalignment

detection process, the aperture is adjusted to achieve a good image contrast and sufficient depth of field. For the radius of curvature measurement, the aperture will be adjusted to the maximum allowed size without saturating the captured image. Large aperture size helps in reducing the depth of field of the imaging system. In our calculation, the aperture diameter is set to be 20 mm.

Figures 8.1 and 8.2 shows the depth of field of the imaging system (δ) versus the image position tolerance ($2dz'$) as a function of the base radius of the test surface. In the plots, radius of the test surface can be measured to the required accuracy only in the region where the depth of field curve is below the image location tolerance curve.

The results show that the current system is capable of measuring radius of curvature with a 10% accuracy in $|\Delta R/R|$ for most of the surfaces, $|R|$ greater than 25 mm. $|\Delta R/R|$ is a percentage error of the measured surface radius, where ΔR is the absolute error and R is the nominal radius of the part. A much smaller depth of focus is needed to achieve a 1% accuracy in $|\Delta R/R|$. The calculation is based on a 10 mm aperture size, a 50 mm EFL for the objective lens, a 250 mm working distance, a 280 mm camera to test surface distance and a 12 μm CCD array pixel resolution. This calculation did not include optical aberrations in the imaging system, actual detection result will be affected by them and the detection sensitivity may be reduced.

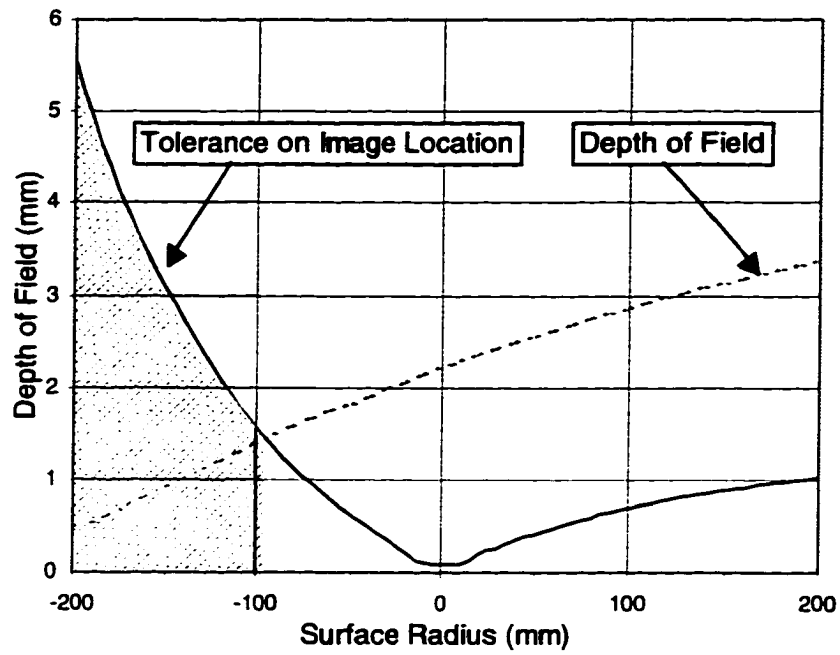


Figure 8.2. Depth of field vs. image position tolerance for $|\Delta R/R|=0.01$.
(Valid region is shaded)

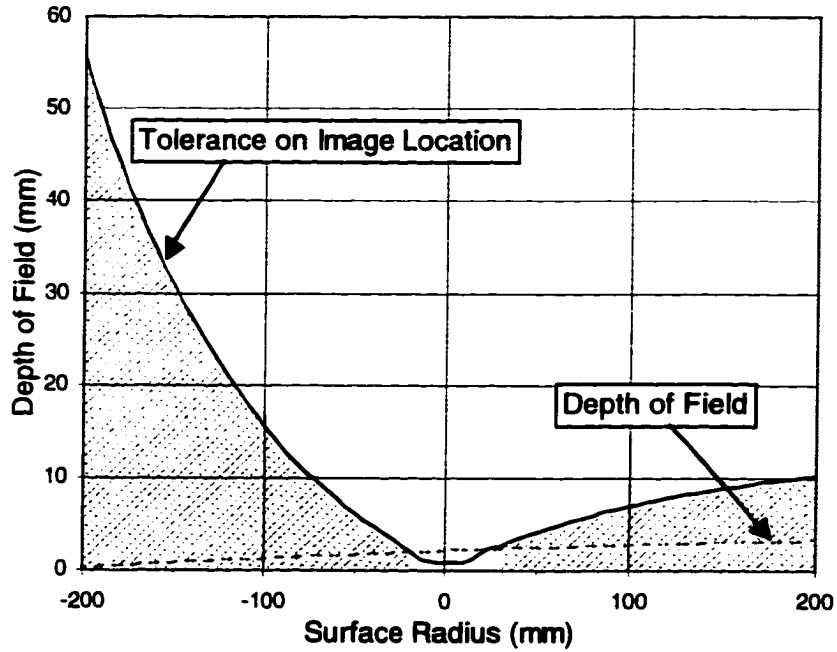


Figure 8.3. Depth of field vs. image position tolerance for $|\Delta R/R|=0.1$.
(Valid regions are shaded)

8.4 OTHER APPLICATIONS

Although the original motivation of this research work is the detection of tool misalignments in the Opticam generator, the idea of retrieving surface slope information from the reflected images may be extended to a wide range of applications. The fact that this technique uses a non-contact method and maybe applied to surfaces with a large range of radius of curvature without modification, makes it extremely attractive. Its simple and flexible structure allows it to be used in some of the hazardous environment considered by the conventional optical metrology systems. Improvements of the system that enable its ability in measuring radius of curvature and surface height map will further expand the horizon of its application.

In conclusion, this research work demonstrates one of the applications of the new technique for surface figure measurement. The basis for this development has been provided and proven both theoretically and experimentally. Modification of the prototype design has the potential in a better detection sensitivity, reliability and lower cost optical metrology system.

APPENDIX

PROGRAM LISTING

- **Main program routine for graphical-user-interface and message handling:
Programming language :**

**IDL (Interactive Data Language), v4.0.1
Research System, Inc. Boulder, CO**

```

:MAIN PROGRAM BODY FOR ON-LINE TOOL MISALIGNMENT DETECTION
:GRAPHICAL USER INTERFACE ROUTINES AND WINDOW HANDLES
:
PRO PDMENU_Event, Event
COMMON MAINBLK, FG_Win, FG_Img, Orig_Win, Dest_Win, FG_xy, OImg_xy, FIELD_FName, FILE.$
    SELECT, ROI, O_Data, BUTTON_Show, toggle.$
    S_Data, P_Data, FFT_Data, F_Data, Phase_Data, D_Data, H_Data, $
    R, Yerror, FIELD_Rd, FIELD_YError
CASE Event, Value OF
File.Open': BEGIN
    FILEIO, "OPEN", FILE, O_DATA
    IF N_ELEMENTS(O_DATA) NE 0 THEN O_DATA=ROTATE(O_DATA,1)
    IF (FILE NE ") THEN WIDGET_CONTROL, FIELD_FNAME, SET_VALUE=FILE
    SELECTR, ROI, FG_Win / CLEAN
    ROI(*)=0
    DISPLAY, O_DATA, 336, 448, FG_Win
END
File.Save': BEGIN
    FILEIO, "SAVE", FILE, O_DATA
END
File.Save As': BEGIN
    FILEIO, "SAVEAS", FILE, O_DATA
    IF (FILE NE ") THEN WIDGET_CONTROL, FIELD_FNAME, SET_VALUE=FILE
END
File.Exit': BEGIN
    WIDGET_CONTROL, event.top, /DESTROY
END
'Grab/Live': BEGIN
    if (not n_elements(toggle)) then toggle=1
    if (toggle eq 1) then begin
        FILE=""
        O_Data=bytarr(640,480)
        dummy = CALL_EXTERNAL('dll_com.dll', 'Mil_Grab', O_Data, long(640), long(480), VALUE =
[0b, 1b, 1b])
        O_Data=rotate(O_Data,7)
        DISPLAY, O_Data, 336, 448, FG_Win
        toggle=not toggle
    endif else begin

```

```

        dummy = CALL_EXTERNAL('dll_com.dll','Mil_Live',"Live Video")
        toggle=not toggle
    endwhile
END
'Process Image': BEGIN
    WIDGET_CONTROL, /HOURGLASS
    t0=systime(1)
    IF N_ELEMENTS(S_DATA) NE 0 THEN BEGIN
        CAL_PHAS/LoFreq/HiFreq/SMTH
        CAL_PHAS/TILT
        CAL_PHAS/CALERR
        print, 'Processing Time: ', systime(1)-t0, 'sec.'
        H_Data=Histo(Phase_Data, level=100)
        WIDGET_CONTROL, FIELD_Rd, GET_VALUE=R
        if N_ELEMENTS(R) NE 0 then begin
            if Yerror lt 0 then $
                WIDGET_CONTROL, FIELD_YError,
SET_VALUE=STRCOMPRESS(STRING(Yerror*20*R/80))+ ' um Dwell Error' $
            else $
                WIDGET_CONTROL, FIELD_YError,
SET_VALUE=STRCOMPRESS(STRING(Yerror*20*R/80))+ ' um'
            endif
            DISPLAY.Phase_Data, 512, 256, Dest_Win
            :automatic profiles of the calculated phase function
: WIDGET_CONTROL, Oimg_xy, $
: SET_VALUE='Left Button -> Toggle Row/Col; Right Button -> Exit'
: IF N_ELEMENTS(D_Data) NE 0 THEN TProf, CONGRID(Phase_Data, 512, 256), Orig_win, Dest_Win
        ENDIF
    END
'Hardware Setup.Initialization': BEGIN
    dummy = CALL_EXTERNAL('dll_com.dll','Mil_Init', BYTARR(640,480), long(640), long(480), $
        VALUE = {0b, 1b, 1b})
    END
'Hardware Setup.Close FrameGrabber': BEGIN
    dummy = CALL_EXTERNAL('dll_com.dll','Mil_Free',"Free Mil")
    END
'Help.About': BEGIN
    PRINT, 'Under Construction.'
    END
ENDCASE
END

PRO FG_Img_Event, Event
COMMON MAINBLK, FG_Win, FG_Img, Orig_Win, Dest_Win, FG_xy, Oimg_xy, FIELD_FName, FILE.$
    SELECT, ROI, O_Data, BUTTON_Show, toggle, $
        S_Data, P_Data, FFT_Data, F_Data, Phase_Data, D_Data, H_Data, $
        R, Yerror, FIELD_Rd, FIELD_YError
    WIDGET_CONTROL, FG_xy, $
        SET_VALUE=' Cursor: (' +
STRCOMPRESS(STRING(event.x))+',' +STRCOMPRESS(STRING(event.y))+')'
    IF SELECT NE 0 THEN BEGIN
        IF (event.type EQ 0) THEN BEGIN
            SELECTR, ROI, FG_Win / CLEAN
            FOR i=0, 2 DO BEGIN
                ROI(2*i)=event.x
                ROI(2*i+1)=event.y
            ENDFOR
        ENDIF
    ENDIF

```

```

SELECTR,ROI,FG_Win/CLEAN
WHILE event.type NE 1 DO BEGIN
  EVENT=WIDGET_EVENT(FG_Img)
  ROI(4)=ROI(2)
  ROI(5)=ROI(3)
  ROI(2)=event.x
  ROI(3)=event.y
  SELECTR,ROI,FG_Win
  WIDGET_CONTROL, FG_xy, $
  SET_VALUE= $
  ' W:' + STRCOMPRESS(STRING(ABS(event.x-roi(0))))+ $
  ' H:' + STRCOMPRESS(STRING(ABS(event.y-roi(1))))
ENDWHILE
ENDIF
ENDIF
END

PRO DList_Event, Event
COMMON MAINBLK, FG_Win,FG_Img, Orig_Win, Dest_Win, FG_xy, OImg_xy, FIELD_FName, FILE.$
  SELECT, ROI, O_Data, BUTTON_Show, toggle,$
  S_Data, P_Data, FFT_Data, F_Data, Phase_Data, D_Data, H_Data, $
  R,Yerror, FIELD_Rd, FIELD_YError
CASE Event.Index OF
  0: IF N_ELEMENTS(S_Data) NE 0 THEN D_Data=S_Data
  1: IF N_ELEMENTS(P_Data) NE 0 THEN D_Data=P_Data
  2: IF N_ELEMENTS(FFT_Data) NE 0 THEN D_Data=ABS(FFT_Data)
  3: IF N_ELEMENTS(F_Data) NE 0 THEN D_Data=ABS(F_Data)
  4: IF N_ELEMENTS(Phase_Data) NE 0 THEN D_Data=Phase_Data
  5: IF N_ELEMENTS(H_Data) NE 0 THEN D_Data=H_Data
ENDCASE
IF N_ELEMENTS(D_Data) NE 0 THEN DISPLAY, D_Data,512,256,Orig_Win
END

PRO YERR_Event, Event
COMMON MAINBLK, FG_Win,FG_Img, Orig_Win, Dest_Win, FG_xy, OImg_xy, FIELD_FName, FILE.$
  SELECT, ROI, O_Data, BUTTON_Show, toggle,$
  S_Data, P_Data, FFT_Data, F_Data, Phase_Data, D_Data, H_Data, $
  R,Yerror, FIELD_Rd, FIELD_YError
WIDGET_CONTROL, FIELD_Rd, GET_VALUE=R
IF Yerror lt 0 THEN $
  WIDGET_CONTROL, FIELD_YError, SET_VALUE=STRCOMPRESS(STRING(Yerror*20*R/80))+ ' um
Dwell Error' $
ELSE $
  WIDGET_CONTROL, FIELD_YError, SET_VALUE=STRCOMPRESS(STRING(Yerror*20*R/80))+ ' um'
END

PRO MAIN_Event, Event
COMMON MAINBLK, FG_Win,FG_Img, Orig_Win, Dest_Win, FG_xy, OImg_xy, FIELD_FName, FILE.$
  SELECT, ROI, O_Data, BUTTON_Show, toggle,$
  S_Data, P_Data, FFT_Data, F_Data, Phase_Data, D_Data, H_Data, $
  R,Yerror, FIELD_Rd, FIELD_YError
WIDGET_CONTROL,Event.Id,GET_UVALUE=Ev
CASE Ev OF
'Menu': PDMENU_Event, Event
'FG_Img': BEGIN
  FG_Img_Event, Event

```



```

END
'Edit_ROI': BEGIN
  SELECT=(NOT SELECT)
  IF SELECT THEN $
    WIDGET_CONTROL, BUTTON_Show, SET_VALUE='Default' $
  ELSE WIDGET_CONTROL, BUTTON_Show, SET_VALUE='Rotate'
  END
'Default': BEGIN
  IF SELECT THEN BEGIN
    SELECTR,ROI,FG_Win, /CLEAN           :ELSE SELECT=I
    DEF_ROI=[45.261,243.165,243.165]
    SELECTR,DEF_ROI,FG_Win, /CLEAN
    ROI=DEF_ROI
  ENDIF ELSE BEGIN
    O_Data=ROTATE(O_Data,1)
    DISPLAY,O_DATA, 336,448,FG_Win
    SELECTR,ROI,FG_Win,/CLEAN
  ENDELSE
  END
'Pick': BEGIN
  osize=size(O_Data)
  XFACT=osize(1)/336.
  YFACT=osize(2)/448.
  X0=ROI(0)*XFACT
  X1=ROI(2)*XFACT
  Y0=ROI(1)*YFACT
  Y1=ROI(3)*YFACT
  :print,roi
  :print,'x0,x1,y0,y1'.x0,x1,y0,y1
  S_Data=O_Data((X0 < X1)>0:(X0 > X1)<(osize(1)-1),(Y0 < Y1)>0:(Y0 > Y1)<(osize(2)-1))
  DISPLAY,S_Data,512,256,Orig_Win
  END
'Radius': BEGIN
  YERR_Event, Event
  END
'Display_List': BEGIN
  DList_Event,Event
  END
'Orig_Img': BEGIN
  WIDGET_CONTROL, OImg_xy, $
  SET_VALUE='Cursor: (' +
STRCOMPRESS(STRING(event.x))+','+STRCOMPRESS(STRING(event.y))+')'
  if (event.press ne 0) then if (N_ELEMENTS(Phase_Data) NE 0) then begin
:      CAL_PHAS, VPOS=event.y./TILT
:      CAL_PHAS, VPOS=event.y./CALERR
:      DISPLAY,Phase_Data,512,256,Orig_Win
  WIDGET_CONTROL, FIELD_Rd, GET_VALUE=R
  if N_ELEMENTS(R) NE 0 then begin
    if Yerror lt 0 then $
      WIDGET_CONTROL, FIELD_YError,
SET_VALUE=STRCOMPRESS(STRING(Yerror*20*R/80))+ ' um Dwell Error' $
    else $
      WIDGET_CONTROL, FIELD_YError,
SET_VALUE=STRCOMPRESS(STRING(Yerror*20*R/80))+ ' um'
  endif
  endif
  END

```

```

'Profiles': BEGIN
  WIDGET_CONTROL, Oimg_xy, $
  SET_VALUE=Left Button -> Toggle Row/Col; Right Button -> Exit'
  IF N_ELEMENTS(D_Data) NE 0 THEN TProf, CONGRID(D_Data,512,256), Orig_win, Dest_Win
  END
ENDCASE
END

```

```

=====MAIN RROGRAM=====
:OPEN MAIN PROGRAM WINDOW AND HANDLE PROGRAM EVENTS
PRO xwdet. GROUP=Group
cd,'d:\T_IDLV'
LOADCT,0
COMMON MAINBLK, FG_Win,FG_Img, Orig_Win, Dest_Win, FG_xy, Oimg_xy, FIELD_FName, FILE,$
  SELECT, ROI, O_Data, BUTTON_Show, toggle,$
  S_Data, P_Data, FFT_Data, F_Data, Phase_Data, D_Data, H_Data, $
  R,Yerror, FIELD_Rd, FIELD_YError
SELECT=0
ROI=INTARR(6)
YError=0

IF N_ELEMENTS(Group) EQ 0 THEN GROUP=0
junk = { CW_PDMENU_S, flags:0, name:" }
MAIN = WIDGET_BASE(GROUP_LEADER=Group, $
  COLUMN=1, $
  MAP=1, $
  TITLE='Center for Optics Manufacturing', $
  UVALUE='MAIN', $
  XOFFSET=70, $
  XSIZE=890, $
  YOFFSET=10, $
  YSIZE=640)

BASE_Menu = WIDGET_BASE(MAIN, $
  ROW=1, $
  MAP=1, $
  TITLE='MenuBase', $
  UVALUE='BASE_Menu')

MenuDesc = [ $
  { CW_PDMENU_S, 1, 'File' }, $; 0
  { CW_PDMENU_S, 0, 'Open' }, $; 1
  { CW_PDMENU_S, 0, 'Save' }, $; 2
  { CW_PDMENU_S, 0, 'Save As' }, $; 3
  { CW_PDMENU_S, 2, 'Exit' }, $; 4
  { CW_PDMENU_S, 0, 'Grab/Live' }, $; 5 //was called Acquire Image
  { CW_PDMENU_S, 0, 'Process Image' }, $; 6
  { CW_PDMENU_S, 1, 'Hardware Setup' }, $; 7
  { CW_PDMENU_S, 0, 'Initialization' }, $; 8
  { CW_PDMENU_S, 2, 'Close FrameGrabber' },$, 9
  { CW_PDMENU_S, 3, 'Help' }, $; 10
  { CW_PDMENU_S, 2, 'About' } $; 11
]

PDMENU = CW_PDMENU( BASE_Menu, MenuDesc, /RETURN_FULL_NAME, $
  UVALUE='Menu')

```

```

BASE_Win = WIDGET_BASE(MAIN, $
  COLUMN=3, $
  SPACE=5, $
  MAP=1, $
  TITLE='WinBase', $
  UVALUE='BASE_Win')

BASE_Left = WIDGET_BASE(BASE_Win, $
  COLUMN=1, $
  SPACE=5, $
  MAP=1, $
  TITLE='LeftBase', $
  UVALUE='BASE_Left', $
  XSIZE=350)

BASE_Frame = WIDGET_BASE(BASE_Left, $
  ROW=2, $
  SPACE=5, $
  XPAD=6, $
  YPAD=6, $
  FRAME=1, $
  MAP=1, $
  TITLE='Frame', $
  UVALUE='BASE_Frame')

FG_Img = WIDGET_DRAW( BASE_Frame, $
  MOTION_EVENTS=1, $
  BUTTON_EVENTS=1, $
  RETAIN=2, $
  UVALUE='FG_Img', $
  XSIZE=336, $
  YSIZE=448)

BUTTON_Edit = WIDGET_BUTTON( BASE_Frame, $
  UVALUE='Edit_ROI', $
  VALUE='Edit ROI')

BUTTON_Show = WIDGET_BUTTON( BASE_Frame, $
  UVALUE='Default', $
  VALUE='Rotate ')

BUTTON_Pick = WIDGET_BUTTON( BASE_Frame, $
  UVALUE='Pick', $
  VALUE='Select')

FG_xy = WIDGET_LABEL(BASE_Frame, $
  UVALUE='FG_xy', $
  VALUE='Cursor: ( . )')

BASE_Input = WIDGET_BASE(BASE_Left, $
  ROW=6, $
  SPACE=5, $
  XPAD=4, $
  YPAD=3, $
  FRAME=1, $
  MAP=1, $

```

```

    TITLE='Input', $
    UVALUE='BASE_Input')

FieldVal_FName = [ "" ]
FIELD_FName = CW_FIELD( BASE_Input,VALUE=FieldVal_FName, $
    ROW=1, $
    STRING=1, $
    TITLE='File Name :', $
    UVALUE='FileName', $
    XSIZE=37, $
    /NOEDIT)

FieldVal_TDist = [ '250' ]
FIELD_TDist = CW_FIELD( BASE_Input,VALUE=FieldVal_TDist, $
    ROW=1, $
    STRING=1, $
    TITLE='Target to Surface Distance (mm) :', $
    UVALUE='Dist', $
    XSIZE=17, $
    /NOEDIT)

FieldVal_Rd = [ 80 ]
FIELD_Rd = CW_FIELD( BASE_Input,VALUE=FieldVal_Rd, $
    ROW=1, $
    STRING=1, $
    TITLE='Surface Radius (mm) :', $
    UVALUE='Radius', $
    XSIZE=27, $
    /RETURN_EVENT)

FieldVal_YError = [ "" ]
FIELD_YError = CW_FIELD( BASE_Input,VALUE=FieldVal_YError, $
    ROW=1, $
    STRING=1, $
    TITLE='Detected Y-Error (um) :', $
    UVALUE='yError', $
    XSIZE=27, $
    /NOEDIT)

BASE_Right = WIDGET_BASE(BASE_Win, $
    ROW=4, $
    SPACE=5, $
    XPAD=6, $
    YPAD=6, $
    FRAME=1, $
    MAP=1, $
    TITLE='RightBase', $
    UVALUE='BASE_Right')

ListVal = [ $
    'Original Image', $
    'PreProcessed Image', $
    'Frequency Spectrum', $
    'Filtered Spectrum', $
    'Phase Image', $
    'Histogram(Phase)']
LIST = WIDGET_DROPLIST( BASE_Right,VALUE=ListVal, $

```

```

FRAME=0, $
UVALUE='Display_List', $
XOFFSET=0, $
XSIZE=180, $
YSIZE=20)

Orig_Img = WIDGET_DRAW( BASE_Right, $
  BUTTON_EVENTS=1, $
  MOTION_EVENTS=1, $
  RETAIN=2, $
  UVALUE='Orig_Img', $
  XSIZE=512, $
  YSIZE=256)

BLANK1=WIDGET_LABEL(BASE_Right, $
  VALUE=' ')

Orig_xy = WIDGET_LABEL(BASE_Right, $
  UVALUE='Orig_xy', $
  VALUE='Cursor: ( . )', $
  XSIZE=358, $
  XOFFSET=100)

BUTTON_Prof = WIDGET_BUTTON( BASE_Right, $
  UVALUE='Profiles', $
  VALUE='Show Profile')

Dest_Img = WIDGET_DRAW( BASE_Right, $
  RETAIN=2, $
  UVALUE='Dest_Img', $
  XSIZE=512, $
  YSIZE=256)

WIDGET_CONTROL, MAIN, /REALIZE

WIDGET_CONTROL, FG_Img, GET_VALUE=FG_Win
WIDGET_CONTROL, Orig_Img, GET_VALUE=Orig_Win
WIDGET_CONTROL, Dest_Img, GET_VALUE=Dest_Win

XMANAGER, 'MAIN', MAIN
END

```

- **Program routines for image processing and phase calculation using the Fourier transform method**

Programming language :

**IDL (Interactive Data Language), v4.0.1
Research System, Inc. Boulder, CO**

```

:NAME:
:      CAL_PHAS
:PURPOSE:
:      This procedure calculates phase discontinuities in the input 2D image.
PRO CAL_PHAS, BW=bw, LOFREQ=lofreq, HIFREQ=hifreq, DIMENSION=dimension, $
      TILT=tilt, LEFT=left, RIGHT=right, VPOS=vpos, CALERR=calerr.
SMTH=smth
COMMON MAINBLK, FG_Win, FG_Img, Orig_Win, Dest_Win, FG_xy, OImg_xy, FIELD_FName, $ FILE.
SELECT, ROI, O_Data, BUTTON_Show, toggle, $
      S_Data, P_Data, FFT_Data, F_Data, Phase_Data, D_Data, H_Data, $
      R, Yerror, FIELD_Rd, FIELD_YError

:=====2D convolution=====
IF N_ELEMENTS(S_DATA) EQ 0 THEN BEGIN
  PRINT, 'No Data to Process!'
  GOTO, QUIT
ENDIF
IF KEYWORD_SET(tilt) THEN GOTO, TILT
IF KEYWORD_SET(calerr) THEN GOTO, CALERR
P_DATA=S_DATA
iSIZE=SIZE(P_Data)
hSIZE=iSIZE(1)
vSIZE=iSIZE(2)

:Low Frequency Intensity Variation Correction (2D_Process)
IF KEYWORD_SET(lofreq) THEN BEGIN
  PRINT, 'Correcting Intensity Non-uniformity..'
  IF KEYWORD_SET(lofreq) LT 4 THEN lofreq=8
  SM_FLTR=FLTARR(lofreq, 1)
  SM_FLTR(*)=1.
  LOW_FREQ=FLOAT(P_Data)
  FOR COUNT=0, 2 DO $
    LOW_FREQ=CONVOL(LOW_FREQ, SM_FLTR)/TOTAL(SM_FLTR)
  P_Data=P_Data-LOW_FREQ
  P_Data=P_Data(2*lofreq:hSIZE-1-2*lofreq, *)
  for v=0, vSIZE-1 do $
    P_Data(*, v)=(P_Data(*, v)-MIN(P_Data(*, v)))/(MAX(P_Data(*, v))-MIN(P_Data(*, v)))*255.
  iSIZE=SIZE(P_Data)
  hSIZE=iSIZE(1)
  vSIZE=iSIZE(2)
ENDIF

:High Frequency Noise Reduction(2D_PROCESS)
IF KEYWORD_SET(hifreq) THEN BEGIN
  PRINT, 'Correcting High Frequency Noise...'
  IF KEYWORD_SET(hifreq) EQ 0 THEN hifreq=4
  SM_FLTR=FLTARR(hifreq, 1)

```

```

SM_FLTR(*)=1.
P_Data=CONVOL(P_Data,SM_FLTR)/TOTAL(SM_FLTR)
P_Data=P_Data(hifreq:hSIZE-1-lofreq,*)
ENDIF

:Display processed image
DISPLAY,P_Data,512,256,Dest_Win

:=====FOURIER ANALYSIS OF THE IMAGE=====
PRINT,'Calculating Phase...'
IF KEYWORD_SET(dimension) NE 2 THEN BEGIN
:----1D Routine----
iSIZE=SIZE(P_Data)
hSIZE=512
vSIZE=iSIZE(2)
P_Data=CONGRID(P_Data,hSIZE,vSIZE)
Filter=FLTARR(hSIZE,vSIZE)
FFT_Data=COMPLEXARR(hSIZE,vSIZE)
F_Data=COMPLEXARR(hSIZE,vSIZE)
HAM_FLTR=SIN(!PI*FINDGEN(hSIZE)/hSIZE) :1D Hamming Filter
T_ARRAY=FLTARR(vSIZE) :Array Remembers the Hamonics for each row
PP_Data=FLTARR(hSIZE,vSIZE)
FOR V=0,vSIZE-1 DO BEGIN
PP_Data(*,V)=P_Data(*,V)*HAM_FLTR
FFT_Data(*,V)=SHIFT(FFT(PP_Data(*,V),-1),hSIZE/2.)
: FFT_Data(*,V)=FFT_Data(*,V)/MAX(FFT_Data(*,V))*255.
M=MAX(ABS(FFT_Data(0:250,V)),TILT)
T_ARRAY(V)=TILT
ENDFOR

: Spatial filter the image for phase calculation
TILT=(MAX(T_ARRAY)+MIN(T_ARRAY))/2.
IF KEYWORD_SET(bw) EQ 0 THEN $
bw=(hSIZE/2.-TILT)/2 :Define Filter BandWidth
MASK=FLTARR(hSIZE)
MASK(hSIZE/2.-bw:hSIZE/2.+bw)=1.0
SIG=COMPLEXARR(hSIZE,vSIZE)
FOR V=0,vSIZE-1 DO BEGIN
F_Data(*,V)=SHIFT(FFT_Data(*,V),hSIZE/2.-TILT)*MASK
SIG(*,V)=FFT(F_Data(*,V),1)
ENDFOR
Phase_Data=ATAN(IMAGINARY(SIG)/FLOAT(SIG))

:=====PHASE UNWRAPPING BOTH X and Y DIRECTIONS=====
:(Required for 1D Phase Calculation Process)
PRINT,'Phase Unwrapping...'
FOR J=0,vSIZE-1 DO BEGIN
FOR I=1, hSIZE-1 DO BEGIN
BFR=Phase_Data(I-1,J)
PTS=Phase_Data(I,J)
WHILE ABS(BFR-PTS) GT !PI/2 DO PTS=PTS+(BFR-PTS)/ABS(BFR-PTS)*!PI
Phase_Data(I,J)=PTS
ENDFOR
ENDFOR
REF1=hSIZE/4.
REF2=hSIZE*3/4.

```

```

FOR J=1,VSIZE-1 DO BEGIN
  BFR=Phase_Data(REF1,J-1)
  PTS=Phase_Data(REF1,J)
  WHILE ABS(BFR-PTS) GT !PI/2 DO PTS=PTS+(BFR-PTS)/ABS(BFR-PTS)*!PI
  Phase_Data(*,J)=Phase_Data(*,J)+PTS-Phase_Data(REF1,J)
  BFR=Phase_Data(REF2,J-1)
  PTS1=Phase_Data(REF2,J)
  WHILE ABS(BFR-PTS1) GT !PI/2 DO PTS1=PTS1+(BFR-PTS1)/ABS(BFR-PTS1)*!PI
  Phase_Data(*,J)=Phase_Data(*,J)+(PTS1-Phase_Data(REF2,J))*(FINDGEN(HSIZE)-REF1)/(REF2-REF1)
ENDFOR
ENDIF ;----ID Process-----

```

```

:==SMOOTHING PHASE FUNCTION TO REDUCE HIGH FREQUENCY NOISE==

```

```

IF KEYWORD_SET(smth) THEN BEGIN
  PRINT,'Smoothing the Phase function...'
  SZ=10
  SM_FLTR=FLTARR(SZ,1)
  SM_FLTR(*,*)=1.
  Phase_Data=CONVOL(Phase_Data,SM_FLTR)/TOTAL(SM_FLTR)
  Phase_Data=CONGRID(Phase_Data(SZ:HSIZE-1-SZ,*),HSIZE,VSIZE)
ENDIF

```

```

:==REMOVE TILT IN THE CALCULATED PHASE FUNCTION==

```

```

TILT:
IF KEYWORD_SET(tilt) THEN BEGIN
  psize=size(phase_data)
  IF KEYWORD_SET(left) EQ 0 THEN left=float(psize(1))/4.5
  IF KEYWORD_SET(right) EQ 0 THEN right=float(psize(1))/2.2
  IF KEYWORD_SET(vpos) EQ 0 THEN $
    vpos=float(psize(2))/1.4 ELSE vpos=vpos/256.*float(psize(2))
  ; RG=100
  ; LLine=Phase_Data(left-rg:left+rg,vpos)
  ; RLine=Phase_Data(right-rg:right+rg,vpos)
  ; LFIT=POLY_FIT(FINDGEN(2*rg+1)+left-rg,LLine,1)
  ; RFIT=POLY_FIT(FINDGEN(2*rg+1)+right-rg,RLine,1)
  ; SUB=FINDGEN(pSize(1))*(LFIT(1)+RFIT(1))/2.)+(LFIT(0)+RFIT(0))/2.
  LINE=Phase_Data(left:right,vpos)
  ts=size(line)
  XX=FINDGEN(ts(1))+left
  FITLINE=POLY_FIT(XX,LINE,1)
  SUB=FINDGEN(pSize(1))*FITLINE(1)+FITLINE(0)
  FOR I=0,pSize(2)-1 DO Phase_Data(*,I)=Phase_Data(*,I)-SUB
ENDIF

```

```

:==CALCULATE PHASE DISCONTINUITIES IN THE PHASE FUNCTION==

```

```

CALERR:
IF KEYWORD_SET(calerr) THEN BEGIN
  psize=size(phase_data)
  IF KEYWORD_SET(left) EQ 0 THEN left=float(psize(1))/4.
  IF KEYWORD_SET(right) EQ 0 THEN right=float(psize(1))*(3./4.)
  IF KEYWORD_SET(vpos) EQ 0 THEN $
    vpos=float(psize(2))/1.7 ELSE vpos=vpos/256.*float(psize(2))
  Lphase=MOMENT(Phase_Data(left-80:left+80,vpos))
  Rphase=MOMENT(Phase_Data(right-80:right+80,vpos))
  Yerror=(Lphase(0)-Rphase(0))
  ; line1=fltarr(psize(1))

```



```

: line2=ftarr(psize(1))
: line1(*)=Lphase(0)
: line2(*)=Rphase(0)
: print,yerror
: plot.Phase_Data(left-80:left+80,vpos)/noerase, YRANGE=[-.5..5]
: plot.Phase_Data(right-80:right+80,vpos),YRANGE=[-.5..5]
ENDIF
QUIT:
END

```

- **Code for compiled Dynamical Link Library (DLL) functions for Matrox frame grabber control.**

Programming language : Microsoft Visual C++, v4.0

Note: Header files and included software libraries are not listed.

```

#include <windows.h>
#include <stdio.h>
#include <mil.h>

// Define a pointer to a float type.
#ifndef LPFLOAT
#define LPFLOAT    FLOAT FAR*
#endif
#ifndef LPBYTE
#define LPBYTE     BYTE FAR*
#endif

MIL_ID    MilApplication, /* Application identifier. */
          MilSystem,     /* System identifier. */
          MilDisplay,   /* Display identifier. */
          MilCamera,    /* Camera identifier. */
          MilImage:     /* Image buffer identifier. */

// Function prototypes.
BOOL WINAPI DllMain(HINSTANCE hInst, ULONG ulReason, LPVOID lpReserved);
BOOL WINAPI Mil_Init(LONG LArgc, LPVOID lpvArgv);
BOOL WINAPI Mil_Free(LONG LArgc, LPVOID lpvArgv);
BOOL WINAPI Mil_Grab(LONG LArgc, LPVOID lpvArgv);

// Windows DLL entry point.
BOOL WINAPI DllMain(HINSTANCE hInst, ULONG ulReason, LPVOID lpReserved)
{
    return(TRUE);
}

BOOL WINAPI Mil_Init(LONG lArgc, LPVOID lpvArgv)
{

```

```

LPLONG      lplArgv = NULL;
LPBYTE      lpfArray = NULL;
LONG        lArrayWidth = 0;
LONG        lArrayHeight = 0;
LONG        lArrayPts = 0;
CHAR        szMsg[256];

lplArgv = (LPLONG)lplArgv;
lpfArray = (LPBYTE)lplArgv[0];
lArrayWidth = (LONG)(lplArgv[1]);
lArrayHeight = (LONG)(lplArgv[2]);
lArrayPts = (LONG)(lArrayWidth * lArrayHeight);

//Allocate defaults.
MappAllocDefault(M_SETUP, &MilApplication, &MilSystem,
                 &MilDisplay, &MilCamera, &MilImage);

//Allocate buffer.
MbufAlloc2d(MilSystem,
            lArrayWidth, lArrayHeight,
            8L+M_UNSIGNED,
            M_IMAGE+M_GRAB+M_PROC,
            &MilImage);

sprintf(szMsg, "%s", "Frame Grabber Initialized!");
MessageBox (NULL, (LPSTR)szMsg, (LPSTR)"Reply from DLL_COM",
           MB_OK | MB_ICONINFORMATION);

return TRUE;
}

BOOL WINAPI Mil_Free(LONG lArgc, LPVOID lplArgv)
{
    CHAR        szMsg[256];

    sprintf(szMsg, "%s", "Frame Grabber Released!");
    MessageBox (NULL, (LPSTR)szMsg, (LPSTR)"Reply from DLL_COM",
               MB_OK | MB_ICONINFORMATION);

    //Release defaults.
    MappFreeDefault(MilApplication, MilSystem, MilDisplay, MilCamera, MilImage);

    return TRUE;
}

BOOL WINAPI Mil_Grab(LONG lArgc, LPVOID lplArgv)
{
    LPLONG      lplArgv = NULL;
    LPBYTE      lpfArray = NULL;
    LONG        lArrayWidth = 0;
    LONG        lArrayHeight = 0;
    LONG        lArrayPts = 0;
    LPBYTE      lpfReturn = NULL;

    lplArgv = (LPLONG)lplArgv;
    lpfArray = (LPBYTE)lplArgv[0];

```

```
IArrayWidth = (LONG)(lpArgv[1]);
IArrayHeight = (LONG)(lpArgv[2]);
lpfReturn = (LPBYTE)lpArgv[3];
IArrayPts = (LONG)(IArrayWidth * IArrayHeight);

//Grab an image.
MdigGrab(MilCamera. MilImage);
MbufGet2d(MilImage,0,0,
          IArrayWidth, IArrayHeight,
          lpfReturn);

return TRUE;
}
```

REFERENCES

- Auluck, S. K. H., "High-sensitivity diffraction-compensated Moiré deflectometry", *J. Modern Opt.*, **41**(4), 791-805 (1994).
- Bone, D. A., H. A. Bachor and R. J. Sandeman, "Fringe Pattern Analysis Using a 2-D Fourier Transform," *Appl. Opt.*, **25**, 1653-1660 (1986).
- Bone, D. J., "Fourier fringe analysis: the two-dimensional phase unwrapping problem." *Appl. Opt.*, **30**(25), 3627-3632 (1991).
- Bristow, T. C., G. Wagner, J. R. Biety, and R. A. Auriemma, "Surface profile measurements of curved parts," *Proc. SPIE* **1164**, 134-141 (1989).
- Brooks, R. E. and L. O. Heflinger, "Moiré Gauging Using Optical Interference Patterns", *Appl. Opt.* **8**, 935-939 (1969).
- Caber, P. J., "Interferometric profiler for rough surfaces," *Appl. Opt.*, **32**, 3438-3441 (1993).
- Chen, G. -H., "High-speed fabrication of aspherical surfaces," Ph.D. dissertation, The Institute of Optics, University of Rochester, 1977.
- Chiang, F. -P., "Moiré Methods for Contouring, Displacement, Deflection, Slope and Curvature," *Proc. SPIE*, **153**, 113-119 (1978).
- Chiang, F. -P., "Moiré Methods for Strain Analysis," in *Manual on Experimental Stress Analysis*, A. S. Kobayashi, Ed., Soc. For Exp. Stress Anal., Brookfield Center, CT, 1983.
- Cooley, J. W., "How the FFT gained acceptance," *IEEE Signal Processing Magazine*, **9**(1), 10-13 (1992).

REFERENCES - Continued

Creath, K., "Moiré and Fringe Projection Techniques," Course notes from Optical Testing, Optical Sciences 513, University of Arizona, 1991.

Creath, K. and A. Morales, "Contact and Noncontact Profilers," in *Optical Shop Testing 2nd Edition*, Malacara, D., Ed., John Wiley & Sons, Inc., N.Y. 1992, pp. 687-714.

D. Malacara and S. L. DeVore, "Interferogram Evaluation and Wavefront Fitting" in *Optical Shop Testing*, 2nd Ed., D. Malacara, Ed., John Wiley & Sons, Inc., N.Y. 1992, pp. 455-499.

DeCou, A. B., "Interferometric Star Tracking," *Appl. Opt.*, **13**, 414 -424 (1974).

Frankowski, G., "Optical Profilometry using Spatial Heterodyne Interferometric Methods," *Proc. SPIE* **1500**, 114-123 (1991).

Freischlad, K. and C. L. Koliopoulos, "Fourier description of digital phase-measuring interferometry," *J. Opt. Soc. Am.* **7**, 542-551 (1990).

Gaskill, J., *Linear System, Fourier Transforms, and Optics*, John Wiley & Son, Inc., N.Y. 1978.

Gasvik, K. J., *Optical Metrology*, Wiley, Chichester, N.Y., 1987.

Golini, D. and W. Czajkowski, "Microgrinding Makes UltrasMOOTH Optics Fast," *Laser Focus World*, **28**(7), 146-150, (1992).

Golini, D., "Deterministic Microgrinding and Magnetorheological Finishing: A Systems Approach for Optics Manufacture," internal report, Center for Optics Manufacturing, Rochester, N.Y. 1993.

REFERENCES - Continued

Golini, D., "Advances in Automated CNC Optics Manufacturing through Process Science," COM Summer School class notes, Center for Optics Manufacturing, Rochester, N.Y. June 1996.

Goodman, J. W., *Introduction to Fourier Optics*, 2nd Ed. McGraw-Hill, Inc., N.Y. 1996.

Greivenkamp, J. E., "Sub-Nyquist interferometry," *Appl. Opt.* **26**, 5245-5258 (1987).

Greivenkamp, J. E. and J. H. Bruning, "Phase Shifting Interferometry," in *Optical Shop Testing 2nd Edition*, Malacara, D., Ed., John Wiley & Sons, Inc., N.Y. 1992, pp.501-598.

Greivenkamp, J. E., "Optical Engineering (I)", course notes for Optical Sciences 502. University of Arizona, 1992.

Hayes, J., "Fast Fourier Transforms and Their Applications," in *Applied Optics and Optical Engineering, Vol. XI*, R. R. Shannon and J. C. Wyant, Eds., Academic Press, San Diego, 1992, pp. 55-123.

Hecht, E., *Optics 2nd Edition.*, Addison-Wesley Publishing Company, Inc., M.A. 1987.

Jones, R., "A review of optical techniques for the measurement of surface geometries," *Proc. SPIE*, **599**, 309-316 (1985).

Kafri, O. and A. Livnat, "Reflective Surface Analysis Using Moiré Deflectometry," *Appl. Opt.*, **20**, 3098-3100 (1981).

Kafri, O. and J. Glatt, "Moiré Deflectometry: A Ray Deflection Approach to Optical Testing," *Opt. Eng.*, **24**, 944-960 (1985).

REFERENCES - Continued

Kafri, O., "Noncoherent Method for Mapping Phase Objects," *Opt. Letter*, **5**, 555-557 (1988).

Kingslake, R., *Optical System Design*, Academic Press, Inc. Orlando, FL, 1983.

Kreis, T., "Digital Holographic Interference-Phase Measuring Using the Fourier-Transform Method," *J. Opt. Soc. Am. A*, **3**(6), 847-855 (1986).

Kujawinska, M., "Spatial Phase Measurement Methods," in *Interferogram Analysis: Digital Fringe Pattern Measurement Techniques*, Robinson, D. W. and Reid, G. T., Ed. Institute of Physics Publishing, Bristol and Philadelphia, 1993, pp. 141-193.

Lambropoulos, J., "A simple model for the relation between cutter marks, tool speed and work speed in deterministic microgrinding," Process Science monthly report, Center for Optics Manufacturing, Univ. of Rochester, Sept. 1993.

Lambropoulos, J. and D. Golini, "Cutter marks as vibration-induced errors in deterministic microgrinding," presented at Optical Fabrication and Testing Workshop, *Opt. Soc. Am.*, **13**, 10-17, June (1994).

Leonhardt, K., U. Droste, and H. Tiziani, "Microshape and rough-surface analysis by fringe projection," *Appl. Opt.* **33**, 7477-7488 (1994).

Liedes, J., "OPTICAM Machine Design," *SPIE*, **1531**, 216-222 (1991).

Lightenberg, F. K., "The Moiré Method," *Proc. Soc. Exp. Stress Anal.*, **12**, 83-98 (1955).

Lindquist, A., "A survey of commercial systems for advanced optics manufacturing," COM Summer School class notes, Center for Optics Manufacturing, Rochester, N.Y. June 1996.

REFERENCES - Continued

Lowman, A. E., "Calibration of a non-null interferometer for aspheric testing," Ph.D. Dissertation, University of Arizona, 1995.

Macy, W. W., "Two-dimensional fringe-pattern analysis" *App. Opt.*, **22**, 2898-901 (1983).

Malacara, D., *Optical Shop Testing 2nd Edition*, John Wiley & Sons, Inc., N.Y. 1992.

Matsumoto, T., Y. Kitagawa and T. Minemoto, "Sensitivity-variable moiré topography with a phase shift method", *Opt. Eng.* **35**, 1754-1760 (1996).

Meadows, D. M., W. O. Johnson and J. B. Allen, "Generation of Surface Contours by Moiré Patterns", *Appl. Opt.*, **9**, 942-947 (1970).

Mertz, L., "Complex Interferometry", *Appl. Opt.*, **22**, 1530-1534 (1983a).

Mertz, L., "Real-Time Fringe-Pattern Analysis", *Appl. Opt.*, **22**, 1535-1539 (1983b).

Mertz, L., "Optical Homodyne Phase Metrology", *Appl. Opt.*, **28**, 1011-1014 (1989).

Morimoto, Y. and M., Fujisawa, "Fringe pattern analysis by a phase-shifting method using Fourier transform", *Opt. Eng.*, **33**(11), 3709-14 (1994).

Moss, T., "Optics Manufacturing: It's Not the Same Old Grind," *Photonics Spectra*, 80-92, December, 1994.

Nugent, K. A., "Interferogram Analysis Using an Accurate Fully Automatic Algorithm", *Appl. Opt.*, **24**, 3101-3105 (1985).

O'Shea, D. C., *Elements of Modern Optical Design*, John Wiley & Sons, Inc., N.Y. 1985.

REFERENCES - Continued

Oster, G. and Y. Nishijima, "Moiré Pattern", *Sci. Amer.*, **208**(5), 54-63 (1963).

Pfeifer, T., B. Wang, J. Evertz, and R. Tutsch, "Phase-shifting Moiré deflectometry", *Optik*, **98**(4), 158-162 (1995).

Pollicove H. M. and D. T. Moore, "Automation for Optics Manufacturing," *Proc. SPIE*, **1333**, 2-6 (1990).

Pollicove H. M. and D. T. Moore, "The OPTICAM System: Optics Automation and Management," internal report, Center for Optics Manufacturing, The Institute of Optics, University of Rochester, Sept. 1990.

Pollicove, H. M. and D. T. Moore, "COM: Working to Move the Optics Industry into the 21st Century", *Photonics Spectra*, May 1992.

Pollicove, H. M., D. Golini, and J. Buckman, "Computer Aided Optics Manufacturing", *Optics & Photonics News*, **5**(6), 15-19 (1994).

Press, H., Ed., *Numerical recipes: the art of scientific computing*, Cambridge University Press, New York, 1986.

Quesnel, D., T. Rich and J. Lambropoulos, "Surface errors due to static tool misalignments in deterministic microgrinding", presented at Optical Fabrication and Testing Workshop, *Opt. Soc. Am.*, **13**, 22-25, June (1994).

Reid, G. T., "Moiré Fringes in Metrology," *Opt. Laser Eng.*, **5**, 63-93 (1984)

Reid, G. T., "Automatic Fringe Pattern Analysis: A Review", *Optics and Lasers in Engineering*, **7**, 37-68 (1986).

REFERENCES - *Continued*

Research System, Inc., *IDL reference Guide, IDL User's Guide*, Boulder, 1995.

Rich, T. and A. Lindquist, "Curve generating geometry and tool alignment error on the Opticam SX", Process Science monthly report, Center for Optics Manufacturing, Univ. of Rochester, Sept. 1993.

Robinson, D. W., "Phase Unwrapping Methods," in *Interferogram Analysis: Digital Fringe Pattern Measurement Techniques*, Robinson, D. W. and G. T. Reid Ed. Institute of Physical Publishing, Bristol and Philadelphia 1993.

Robinson, D. W. and G. T. Reid, *Interferogram Analysis: Digital Fringe Pattern Measurement Techniques*, Institute of Physical Publishing, Bristol and Philadelphia 1993.

Roddiar, C. and F. Roddiar, "Interferogram Analysis Using Fourier Transform Techniques", *Appl. Opt.*, **26**, 1668-1673 (1987).

Rowe, S. H. and W. T. Welford, "Surface topography of non-optical surfaces by projected interference fringes," *Nature*, **216**, 786-787 (1967).

Scott, R. M., "Optical Manufacturing", in *Applied Optics and Optical Engineering Volume III*, Shannon, R. R. and J. C. Wyant Ed., Academic Press, Inc., Orlando, FL 1980, pp. 43-95.

Servin, M., R. Rodriguez-Vera, M. Carpio and A. Morales, "Automatic Fringe Detection Algorithm used for Moiré Deflectometry", *Appl. Opt.*, **29**, 3266-3270 (1990).

Shack, R. V., "Aberration Theory," course notes for Optical Sciences 506, University of Arizona ,1992(a).

Shack, R. V., "Advanced Aberration Theory," course notes for Optical Sciences 514, University of Arizona ,1992(b).

REFERENCES - Continued

Sinclair D., "Simulation of optical surface errors resulting from manufacturing processes", Phase I Contract Summary Report, #DAAA21-94-C-0003, the U.S. Army Material Command, Sinclair Optics, Inc., 1994.

Smith, W. J., *Modern Optical Engineering: The Design of Optical Systems 2nd Ed.*, McGraw-Hill, Inc., N.Y. 1990.

Stevens, R., "Surface Distortions Caused by Vibratory Motion between Cutting Tool and Workpiece", Process Science monthly report, Center for Optics Manufacturing, Univ. of Rochester, Sept. 1993.

Takasaki, H., "Moiré Topography", *Appl. Opt.*, **9**, 1467-1472 (1970).

Takasaki, H., "Moiré Topography", *Appl. Opt.*, **12**, 845-850 (1973).

Takeda, M., H. Ina and S. Kobayashi, "Fourier-transform method of fringe-pattern analysis for computer-based topography and interferometry", *J. Opt. Soc. Am.*, **72**, 156-60 (1982).

Taylor, J. S., M. A. Piscotty, K. L. Blaedel, and F. A. Gray, "Working with the Superabrasives Industry to Optimize Tooling for Grinding Brittle Materials", presented at Spring Topical Meeting on Precision Grinding of Brittle Materials, Am. Soc. Prec. Eng., June (1996).

Uitterdijk, T., H. J. Frankena and C. Smorenburg, "Profiling of aspherical surfaces using Moiré deflectometry", *Proc. SPIE*, **2248**, 116-124 (1994).

Venkataraman, N. and Gan, R. F., "A dynamic model for microgrinding spherical optical surfaces," presented at International Conference on Optical Fabrication and Testing, Tokyo, Japan, June, 1995.

REFERENCES - Continued

Vinokur, S. I., *Geometrical method for generating a surface with a tubular tool, in generation of optical surfaces*, Ed. Kumanin, K. G., The Focal Library, N.Y. 1962.

Wasowski, J. J., "Moiré Topographic Map", *Opt. Comm.* **2**(7), 321-323 (1970).

Wasowski, J. J., "Moiré Surface Contouring by Addition Method", *Proc. 6th Int. Conf. On Experimental Stress Analysis* (VDI – Verlag, Dusseldorf), 127-134 (1978).

Welford, W. T., *Aberrations of Optical Systems*, Adam Hilger, Boston, 1986.